# Analytical scalings of the linear Richtmyer-Meshkov instability when a rarefaction is reflected

F. Cobos-Campos and J. G. Wouchuk*
*E. T. S. I. Industriales, Instituto de Investigaciones Energéticas and CYTEMA, Universidad de Castilla-La Mancha, 13071 Ciudad Real, Spain*

(Received 16 March 2017; published 5 July 2017)

The Richtmyer-Meshkov instability for the case of a reflected rarefaction is studied in detail following the growth of the contact surface in the linear regime and providing explicit analytical expressions for the asymptotic velocities in different physical limits. This work is a continuation of the similar problem when a shock is reflected [Phys. Rev. E **93**, 053111 (2016)]. Explicit analytical expressions for the asymptotic normal velocity of the rippled surface ($\delta v_i^\infty$) are shown. The known analytical solution of the perturbations growing inside the rarefaction fan is coupled to the pressure perturbations between the transmitted shock front and the rarefaction trailing edge. The surface ripple growth ($\psi_i$) is followed from $t = 0+$ up to the asymptotic stage inside the linear regime. As in the shock reflected case, an asymptotic behavior of the form $\psi_i(t) \cong \psi_\infty + \delta v_i^\infty t$ is observed, where $\psi_\infty$ is an asymptotic ordinate to the origin. Approximate expressions for the asymptotic velocities are given for arbitrary values of the shock Mach number. The asymptotic velocity field is calculated at both sides of the contact surface. The kinetic energy content of the velocity field is explicitly calculated. It is seen that a significant part of the motion occurs inside a fluid layer very near the material surface in good qualitative agreement with recent simulations. The important physical limits of weak and strong shocks and high and low preshock density ratio are also discussed and exact Taylor expansions are given. The results of the linear theory are compared to simulations and experimental work [R. L. Holmes *et al.*, J. Fluid Mech. **389**, 55 (1999); C. Mariani *et al.*, Phys. Rev. Lett. **100**, 254503 (2008)]. The theoretical predictions of $\delta v_i^\infty$ and $\psi_\infty$ show good agreement with the experimental and numerical reported values.

DOI: 10.1103/PhysRevE.96.013102

## I. INTRODUCTION

The Richtmyer-Mehskov instability develops after the refraction of a planar incident shock across a rippled contact surface [1,2] and has been continuously studied during the last 50 years, due to its importance in several fields like inertial confinement fusion (ICF), high energy density physics (HEDP), shock tube research, and astrophysics [3–32]. In Fig. 1, we indicate the flow quantities immediately after the incident shock refraction at the material interface, for the situation in which a rarefaction has been reflected back to the right. For $t < 0$, an incident shock comes from the right (fluid $b$) with velocity $-D_i\hat{x}$ and arrives to the contact surface (located at $x = 0$) at $t = 0$. It has compressed fluid $b$ from $\rho_{b0}$ to $\rho_{b1}$. Pressures behind and in front of the incident shock are $p_1$ and $p_0$, respectively. We assume inviscid fluids with an ideal gas equation of state (EOS). The specific heat ratio is $\gamma_b$ to the right of the material surface, and $\gamma_a$ to the left. The fluid velocity behind the incident shock is $U_1$. We define an incident shock strength parameter $z_i = (p_1 - p_0)/p_0$ as in [33]. The initial sound speed of fluid $b$ is $c_{b0} = \sqrt{\gamma_b p_0/\rho_{b0}}$. Therefore, the incident shock Mach number is [33]

$$M_i = \frac{D_i}{c_{b0}} = \sqrt{1 + \frac{(\gamma_b + 1)}{2\gamma_b} z_i}. \quad (1)$$

On the other side of the contact surface, the preshock density is $\rho_{a0}$ and the preshock sound speed is $c_{a0} = \sqrt{\gamma_a p_0/\rho_{a0}}$. The preshock density ratio at the material surface is defined as $R_0 = \rho_{a0}/\rho_{b0}$. We will only consider cases in which a rarefaction is reflected to the right at $t = 0+$. As discussed in [15], for given values of the isentropic exponents $\gamma_a$, $\gamma_b$, and the incident shock Mach number $M_i$, this will happen for small enough values of the preshock density ratio: $R_0 < R_0^{tt}$, where the expression for $R_0^{tt}$ is given by

$$R_0^{tt} = \frac{\gamma_b(\gamma_b + 1)M_i^2}{\gamma_a - \gamma_b + \gamma_b(\gamma_a + 1)M_i^2}. \quad (2)$$

For the case $R_0 = R_0^{tt}$ there is no reflected shock and only a transmitted shock is driven into the fluid to the left, a case called *total transmission*. For equal values of the isentropic exponent, $\gamma_a = \gamma_b$, it is $R_0^{tt} = 1$. For $\gamma_a \neq \gamma_b$, $R_0^{tt}$ could be above or below unity and a rarefaction is always reflected if $R_0 < R_0^{tt}$. We assume that the contact surface is initially rippled in the form $\Psi_i(y,t < 0) = \psi_0 \cos ky$, where $k = 2\pi/\lambda$ is the perturbation wave number, and $\lambda$ is the perturbation wavelength. In linear theory, we assume $\psi_0 \ll \lambda$. After the time $t = 2\psi_0/D_i$, which we assume vanishingly small, the incident shock disappears and a transmitted shock is driven inside fluid $a$ while a rarefaction fan is traveling back inside fluid $b$. We describe the different wavefronts in Fig. 1 where we have indicated the zero order background velocities. The contact surface moves to the left with speed $-U\hat{x}$ and the transmitted front travels to the left with velocity $-D_t\ \hat{x}$. The rarefaction region is composed of a heading front, traveling at the local sound of speed $c_{b1} - U_1$ in the laboratory frame, and a trailing edge, moving with velocity $c_{bf} - U$, also in the laboratory frame. The final density of fluid $b$, between the contact surface and the rarefaction tail, is $\rho_{bf}$ and that of fluid $a$ is $\rho_{af}$. The pressure between the transmitted shock and the rarefaction tail is $p_f$. The Richtmyer-Meshkov instability (RMI) for the case of a rarefaction reflected has been less studied theoretically than the shock reflected case, probably due to the mathematical

*gustavo.wouchuk@uclm.es

 ©2017 American Physical Society

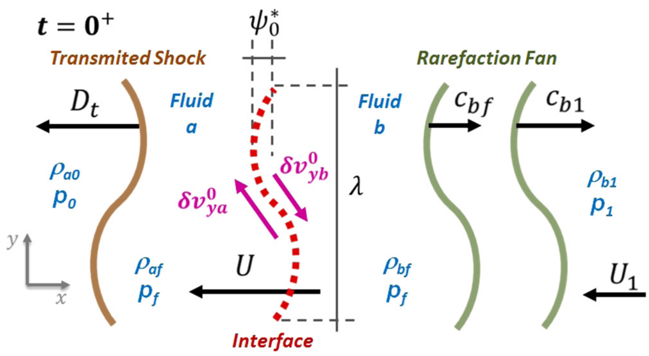


FIG. 1. Rippled wavefronts at $t = 0+$ when a rarefaction is reflected from the contact surface. The front and fluid velocities are indicated.

difficulties associated with perturbation growth inside the rarefaction fan. The original experiments of Meshkov [2] contemplated both scenarios which were discussed some years later by Meyer and Blewett [4] using numerical simulations. It was observed that the growth of the ripple surface changed phase in the rarefaction reflected situation and the asymptotic velocity had an opposite sign with respect to the shock reflected scenario. They observed that in order to obtain agreement between the numerical solution and the linear theory at low compression, an averaged initial post-shock ripple amplitude had to be used in the impulsive formula proposed by Richtmyer [1,4]. After that, the problem of a rarefaction wave traveling alone was analyzed theoretically by Kivity and Hanin in [17], who found an analytical expression for the tangential velocity perturbations inside the rarefaction wave. They used that solution to numerically solve the RMI for the reflected rarefaction case in [18]. Some time later, Yang *et al.* [5] have numerically solved the linear RMI in both cases and discovered that, in the rarefaction scenario, the rarefaction tail ripple also showed a linear asymptotic growth, similar to the contact surface ripple. This problem was considered later in [19] who studied the behavior of the rarefaction profiles and obtained analytical expressions for rarefaction tail ripple growth in different physical limits (weak and strong rarefactions). In [20], the perturbations growing inside a rippled rarefaction were also studied based on the solution obtained before by [17], and explicit analytical expressions for the trailing edge ripple growth were obtained, valid for any incident shock intensity, as well as explicit Taylor expansions of the asymptotic velocity in the regimes of strong and weak expansions. The results of [20] confirmed the expressions found in [19] in the different physical limits. Besides, it was shown that the growth of the rarefaction tail ripple is not of the same type as that occurring at the contact surface. In [6], the RMI for the rarefaction case was studied using Taylor series expansions in time, and the solutions compared very well with existing numerical results. Further analytical studies of the RMI in the rarefaction scenario were also done in [7,8,11] with different analytical techniques and focusing in different time intervals of the linear growth. In particular, in [11] the asymptotic linear velocity was calculated with an exact analytical expression. It is known that the normal asymptotic linear velocity can be written as the sum of two terms [10,11]

$$\delta v_i^\infty = \frac{\rho_{bf}\,\delta v_{yb}^0 - \rho_{af}\,\delta v_{ya}^0}{\rho_{bf} + \rho_{af}} + \frac{-\rho_{bf}\mathcal{F}_b + \rho_{af}\mathcal{F}_a}{\rho_{bf} + \rho_{af}}, \tag{3}$$

where $\delta v_{ya}^0$ and $\delta v_{yb}^0$ are the initial tangential velocities at both sides of the contact surface and $\mathcal{F}_{a,b}$ are spatial averages of the vorticity profiles generated by the rippled fronts in each fluid. For a rarefaction reflected inside fluid $b$, no vorticity is generated and, hence, $\mathcal{F}_b = 0$. For a rederivation of the above expression in this work, the reader is referred to the calculations shown later in Sec. II [Eqs. (107)–(115)]. The $\mathcal{F}_m$ averages become relevant for strong incident shocks, highly compressible fluids, and/or large density contrast at the material surface. In order to have bounded velocity perturbation fields far from the interface, we must require

$$\begin{aligned} \left|\delta v_i^\infty\right| - \left|\delta v_{ya}^\infty\right| &= \mathcal{F}_a, \\ \left|\delta v_i^\infty\right| - \left|\delta v_{yb}^\infty\right| &= 0 \end{aligned} \tag{4}$$

because $\mathcal{F}_b = 0$.

Unfortunately, the second term in the right hand side of Eq. (3) can not be expressed yet in a closed form, as it has to be obtained after solving a functional equation in the complex plane, that couples the dynamics of the rarefaction fan, the contact surface ripple, and the corrugated transmitted front. This technical complication makes it cumbersome to calculate the asymptotic velocity for arbitrary values of the preshock parameters. The validity of Eq. (3) has been previously shown in [11] inside limited regions of the space of the preshock parameters. On the other hand, its counterpart with $\mathcal{F}_b \neq 0$, in the shock reflected case, has been recently studied in a wide region of the space of the preshock parameters [10,15]. Nevertheless, for the rarefaction reflected situation, no further attempt has been made since the first results of [11] to obtain explicit analytical expressions of the linear asymptotic velocity, even approximate, in the range of moderate to strong shock compression, or to present Taylor expansions valid in the important physical limits of weak and strong shocks, weak and strong rarefactions, as recently done for the shock reflected case in [15] or in [21] for a single rippled shock traveling inside an ideal, homogeneous fluid.

One of the aims of this work is to present an explicit analytic formula that works reasonably well for weak to strong shocks and to give accurate Taylor expansions as powers of a small parameter in different physical limits: weak and strong shocks and low and high values of the density ratio at the contact surface. We stress the importance of the vorticity generation behind the transmitted front, showing the spatial structure of the asymptotic velocity fields at both sides of the contact surface, after the fronts have separated away from the material surface. An analysis of the contact surface ripple growth as a function of time is also shown and compared to experiments, where the asymptotic scaling $\psi_i(t) \cong \psi_\infty + \delta v_i^\infty t$ is obtained, in agreement with the findings of [4] or recently of [15]. Bessel series and Taylor series in powers of time are presented to describe the transient temporal evolution of perturbed velocities and ripple either at the transmitted shock and at the contact surface. Besides, the kinetic energy of the asymptotic velocity field is calculated at both sides of the contact surface and the importance of the bulk vorticity field is discussed.

These studies are done for a series of experiments reported in [12,13,22].

This work is structured as follows: the mathematical details are given in Sec. II. The background equations are carefully discussed showing the exact analytical solutions and several approximations corresponding to different physical limits. The perturbed fluid equations are described in the different regions: the fluid between the transmitted shock and the contact surface, the rarefaction wave, and the fluid between the contact surface and the rarefaction trailing edge. The differential equations are briefly reviewed and emphasis is put to obtain accurate descriptions of the temporal evolution of pressure and front corrugations. With this scope in mind, we have made use of analytical results published in earlier works, when necessary, in order to make a self-contained mathematical description. There are some features in the development of these calculations, not published before, i.e., the closed analytical expression for the pressure amplitude function at the rarefaction tail, the Taylor series in powers of time for the normal and tangential velocities, either at the shock front corrugation and at the contact surface ripple. As for the contact surface ripple growth, the asymptotic linear behavior $\psi_\infty + \delta v_i^\infty t$ is obtained, where the value of $\psi_\infty$ is not equal to the initial post-shock ripple amplitude, as first observed by Meyer and Blewett [4]. An analytical formula to calculate $\psi_\infty$ is provided in the general case. The asymptotic linear velocities (normal and tangential) at the rippled contact surface are shown and the iterative procedure for their calculation is briefly reviewed. The asymptotic velocity profiles in both fluids have been carefully calculated as a function of the space coordinates in conditions of strong compression. The kinetic energy stored inside each fluid has been also calculated, showing the error incurred in its calculation if we had neglected the vorticity field inside the fluid compressed by the transmitted shock. In Sec. III, we compare the exact value of the asymptotic normal velocity with an irrotational approximation in different regions of the space of the preshock parameters. Besides, we discuss the goodness of a lowest order approximate formula that consistently includes the effect of the bulk vorticity stored inside fluid $a$. In Sec. IV, we show Taylor expansions in powers of a small parameter in different physical limits. In Sec. V, our predictions are compared with previously reported experiments and simulations. We have found a very good agreement during the interval of time in which linear theory is acceptable. A brief summary is presented in Sec. V. Finally, in the Appendix section, we describe the mathematical procedure to calculate the asymptotic ordinate $\psi_\infty$, and the detailed numerical calculations for a particular experiment. The readers who do not want to delve at first into the mathematical details might skip Sec. II and go directly to Secs. III, IV, and V. Of course, some necessary notation might be required, which is explained at the beginning of the different subsections inside Sec. II.

## II. MATHEMATICAL MODEL

### A. Background profiles

As explained in the Introduction and taking into account Fig. 1, we consider an incident shock that comes from the left inside fluid $b$. The incident shock Mach number is given by Eq. (1). The ratios of the density and sound speed (downstream and upstream values) are given by

$$\frac{\rho_{b1}}{\rho_{b0}} = \frac{2\gamma_b + (\gamma_b+1)z_i}{2\gamma_b + (\gamma_b-1)z_i} = \frac{(\gamma_b+1)M_i^2}{(\gamma_b-1)M_i^2+2}, \tag{5a}$$

$$\frac{c_{b1}}{c_{b0}} = \sqrt{(1+z_i)\frac{\rho_{b0}}{\rho_{b1}}} = \frac{\sqrt{\left(2\gamma_b M_i^2 - \gamma_b + 1\right)\left[(\gamma_b-1)M_i^2+2\right]}}{(\gamma_b+1)M_i}. \tag{5b}$$

The velocity $U_1$ is given by

$$\frac{U_1}{c_{b0}} = \frac{z_i\sqrt{2}}{\sqrt{\gamma_b[2\gamma_b + (\gamma_b+1)z_i]}} = \frac{2}{\gamma_b+1}\left(M_i - \frac{1}{M_i}\right). \tag{6}$$

The downstream Mach number $\beta_i$, in terms of $M_i$, is

$$\beta_i = \frac{D_i - U_1}{c_{b1}} = \sqrt{\frac{(\gamma_b-1)M_i^2+2}{2\gamma_b M_i^2 - \gamma_b + 1}}. \tag{7}$$

After shock refraction, at $t = 0+$, a rarefaction fan is formed that expands fluid $b$ and a shock is transmitted inside fluid $a$. The density at the rarefaction head is $\rho_{b1}$ and it is $\rho_{bf}$ at its trailing edge. The sound speed at the rarefaction head is $c_{b1}$ and $c_{bf}$ at its tail. We define the parameter $M_1 = c_{bf}/c_{b1}$, as proposed in [19], in order to characterize the strength of the expansion. Due to the self-similar character of the centered rarefaction fan, all the thermodynamic quantities inside the expanding fluid are functions of the combination $x/t$. As in [20], we define the dimensionless variable $\zeta = x/(c_{b1}t)$ and the variable $A = c/c_{b1}$, which is the sound speed normalized with the sound speed at the rarefaction head, as defined in [19]. It can be seen that the following relationships hold:

$$c_{b1}\zeta = v_x + c, \tag{8a}$$

$$A = \frac{c}{c_{b1}} = \frac{2M_1}{\gamma_b+1} + \frac{\gamma_b-1}{\gamma_b+1}\zeta, \tag{8b}$$

where $v_x$ is the velocity at a given position inside the rarefaction. The origin of coordinates is located at the unperturbed contact surface after compression. The $\zeta$ coordinates of the rarefaction head and tail are

$$\zeta_{rh} = \frac{\gamma_b + 1 - 2M_1}{\gamma_b - 1}, \tag{9a}$$

$$\zeta_{rt} = M_1. \tag{9b}$$

Density and pressure can be written as functions of the variable $A$:

$$\frac{\rho}{\rho_{b1}} = A^{2/(\gamma_b-1)}, \tag{10a}$$

$$\frac{p}{p_{b1}} = A^{(2\gamma_b)/(\gamma_b-1)}. \tag{10b}$$

The transmitted shock strength is defined by $z_t = (p_f - p_0)/p_0$, where $p_f$ is the fluid pressure across the contact surface. The upstream transmitted shock Mach number is therefore

$$M_t = \frac{D_t}{c_{a0}} = \sqrt{1 + \frac{(\gamma_a+1)}{2\gamma_a}z_t}, \tag{11}$$

and its downstream Mach number $\beta_t$ is

$$\beta_t = \frac{D_t - U}{c_{af}} = \sqrt{\frac{(\gamma_a - 1)M_t^2 + 2}{2\gamma_a M_t^2 - \gamma_a + 1}}. \tag{12}$$

The ratios of the density and sound speed across the transmitted shock are given by

$$\frac{\rho_{af}}{\rho_{a0}} = \frac{2\gamma_a + (\gamma_a + 1)z_t}{2\gamma_a + (\gamma_a - 1)z_t} = \frac{(\gamma_a + 1)M_t^2}{(\gamma_a - 1)M_t^2 + 2}, \tag{13a}$$

$$\frac{c_{af}}{c_{a0}} = \sqrt{(1+z_t)\frac{\rho_{a0}}{\rho_{af}}} = \frac{\sqrt{\left(2\gamma_a M_t^2 - \gamma_a + 1\right)\left[(\gamma_a - 1)M_t^2 + 2\right]}}{(\gamma_a + 1)M_t}. \tag{13b}$$

The contact surface speed $U$ is

$$\frac{U}{c_{a0}} = \frac{z_t\sqrt{2}}{\sqrt{2\gamma_a + (\gamma_a + 1)z_t}} = \frac{2}{\gamma_a + 1}\left(M_t - \frac{1}{M_t}\right). \tag{14}$$

We define the post-shock density ratio

$$R = R_0 \frac{\rho_{af}}{\rho_{a0}}\frac{\rho_{b0}}{\rho_{b1}}\frac{\rho_{b1}}{\rho_{bf}}, \tag{15}$$

and the ratio of post-shock sound speeds

$$N = \frac{N_0}{M_1}\frac{c_{af}}{c_{a0}}\frac{c_{b0}}{c_{b1}}, \tag{16}$$

where

$$N_0 = \frac{c_{a0}}{c_{b0}} = \sqrt{\frac{\gamma_a}{\gamma_b R_0}}. \tag{17}$$

Given the four preshock parameters $z_i$ (or $M_i$), $\gamma_a$, $\gamma_b$, and $R_0 = \rho_{a0}/\rho_{b0}$, we have to calculate both the transmitted shock strength $z_t$ and the rarefaction strength $M_1$. Asking for continuity of the normal velocity and pressure at the contact surface, we get the following system of nonlinear equations:

$$\frac{z_t\sqrt{2}}{\sqrt{2\gamma_a + (\gamma_a + 1)z_t}} = \sqrt{\frac{\gamma_b R_0}{\gamma_a}}\left[\frac{z_i\sqrt{2}}{\sqrt{2\gamma_b + (\gamma_b + 1)z_i}} + \frac{2(1 - M_1)}{\gamma_b - 1}\sqrt{(1 + z_i)\frac{\rho_{b0}}{\rho_{b1}}}\right], \tag{18a}$$

$$M_1 = \left(\frac{1 + z_t}{1 + z_i}\right)^{(\gamma_b - 1)/(2\gamma_b)}. \tag{18b}$$

Unfortunately, there is no known analytical solution to the above system for arbitrary values of the preshock parameters and its solution must be obtained numerically. Nevertheless, we can try approximate solutions in the limits of very weak incident shocks ($z_i \ll 1$) and very strong rarefactions $M_1 \ll 1$.

For very weak shocks ($z_i \ll 1$), we obtain

$$z_t \cong \frac{2\sqrt{\gamma_a R_0}}{\sqrt{\gamma_b} + \sqrt{\gamma_a R_0}} z_i + O\left(z_i^2\right), \tag{19a}$$

$$M_1 \cong 1 - \left(\frac{\gamma_b - 1}{2\gamma_b}\right)\frac{\sqrt{\gamma_b} - \sqrt{\gamma_a R_0}}{\sqrt{\gamma_b} + \sqrt{\gamma_a R_0}} z_i + O\left(z_i^2\right). \tag{19b}$$

From the above results, we deduce that in order to have a rarefaction reflected in the weak incident shock limit, the inequality $\gamma_a \rho_{a0} < \gamma_b \rho_{b0}$ has to be fulfilled, which is the weak shock version of the condition $R_0 < R_0^{tt}$. Besides, we see that it is always $z_t < z_i$ because the final pressure $p_f$ driving the transmitted shock is lesser than the pressure $p_1 > p_0$.

If we consider an incident shock of infinite strength ($z_i \gg 1$), the ratio of sound velocities at the rarefaction trailing front and heading front ($M_1$) will reach its minimum value, which we call $M_1^{\min}$ [20]. The system of equations [Eq. (18)] also allows us to find $M_1^{\min}$ numerically for a given set of preshock parameters. We can obtain an analytic estimate of the minimum rarefaction strength in the limit of vanishingly small preshock density ratio ($R_0 \ll 1$) and very strong incident shocks. After some algebra, we obtain the following results, at the lowest order in $R_0$, under the assumption $M_1^{\min} \ll 1$:

$$M_1^{\min} \cong (\zeta_0 R_0)^{(\gamma_b - 1)/(2\gamma_b)}, \tag{20a}$$

$$\left.\frac{z_t}{z_i}\right)_{z_i \gg 1, R_0 \ll 1} \cong \zeta_0 R_0, \tag{20b}$$

where

$$\zeta_0 = \frac{\gamma_a + 1}{\gamma_b(\gamma_b + 1)}\left(1 + \gamma_b\sqrt{\frac{2}{\gamma_b - 1}}\right)^2. \tag{21}$$

For small preshock density ratio but finite strength incident shocks, we obtain the following expansions in powers of $R_0$:

$$M_1 \cong (1 + z_i)^{\left(\frac{\gamma_b - 1}{2\gamma_b}\right)}\left[1 + \frac{(\gamma_b - 1)\zeta_1}{2\gamma_b}\sqrt{R_0} + O(R_0)\right], \tag{22a}$$

$$z_t \cong \zeta_1\sqrt{R_0} + O(R_0), \tag{22b}$$

where

$$\zeta_1 = \sqrt{\gamma_a\gamma_b}\left\{\frac{2\left[1 - (1 + z_i)^{\frac{1-\gamma_b}{2\gamma_b}}\right]}{\gamma_b - 1}\frac{c_{b1}}{c_{b0}} + \frac{U_1}{c_{b0}}\right\}. \tag{23}$$

The expansions given by Eqs. (20) and (22) are valid in different ranges. Equation (20) is valid in the interval $0 < R_0 \ll R_0^{\min}(z_i)$ and Eq. (22) is only valid in the complementary interval $R_0^{\min}(z_i) \ll R_0 < R_0^{tt}$, where $R_0^{\min}$ is obtained by imposing equality of both expansions at $R_0^{\min}$. The value of $R_0^{\min}$ can be written as

$$R_0^{\min} = \frac{\zeta_1^2 + 2\zeta_0(1 + z_i) + \zeta_1\sqrt{\zeta_1^2 + 4\zeta_0(1 + z_i)}}{2[\zeta_0(1 + z_i)]^2}, \tag{24}$$

which depends on the incident shock strength $z_i$. It is easy to see that $R_0^{\min} \to 0$ for $z_i \to \infty$.

At intermediate values of $R_0$, inside the interval $R_0^{\min} < R_0 < R_0^{tt}$, we can make the rarefaction tail stationary in the laboratory frame. Let us call $R_0^{\text{crit}}$ the value of $R_0$ for which $U = c_{bf}$. For greater values of the preshock density, the rarefaction tail moves following the contact surface and the rarefaction head in the laboratory frame. For $R_0 < R_0^{\rm crit}$, the rarefaction trailing edge moves to the left, following the transmitted shock, in the laboratory frame. The case $R_0 = R_0^{\rm crit}$ is analogous to the case in which the reflected shock wave remains steady in the laboratory frame, as studied in [16]. The analytical expression of $R_0^{\rm crit}$ is

$$R_0^{\rm crit} = \frac{[2\gamma_b + (\gamma_b+1)z_i]\,[1+\gamma_b-(\gamma_b-1)(1+z_i)\zeta_2]^2}{\{(\gamma_b-1)z_i + \sqrt{2\gamma_b(1+z_i)[2\gamma_b+(\gamma_b-1)z_i]}\}^2[1-\gamma_b+(\gamma_a+1)(1+z_i)\zeta_2]}, \tag{25}$$

where

$$\zeta_2 = \left\{\frac{2}{\gamma_b+1} + \frac{\sqrt{2}\left(\gamma_b^2-1\right)z_i}{\sqrt{\gamma_b(1+z_i)[2\gamma_b+(\gamma_b-1)z_i]}}\right\}^{\frac{2\gamma_b}{\gamma_b-1}}. \tag{26}$$

### B. Fluid perturbations behind the transmitted shock

Between the contact surface and the transmitted shock, fluid $a$ has been compressed and set in motion. To simplify the algebra, we work in a system of reference comoving with the compressed fluid $a$. The coordinate origin is located at the contact surface. Because of the front corrugation, pressure and vorticity (entropy) perturbations are generated. Inside fluid $a$ we normalize the perturbations of pressure, density, and velocity according to

$$\delta p_a(x,y,t) = \tilde{p}_a(x,t)\cos(ky)\quad \rho_{af}c_{af}D_i k\psi_0, \tag{27a}$$

$$\delta\rho_a(x,y,t) = \tilde{\rho}_a(x,t)\cos(ky)\ \rho_{af}\ k\psi_0, \tag{27b}$$

$$\delta v_{xa}(x,y,t) = \tilde{u}_a(x,t)\cos(ky)D_i\ k\psi_0, \tag{27c}$$

$$\delta v_{ya}(x,y,t) = \tilde{v}_a(x,t)\sin(ky)D_i\ k\psi_0. \tag{27d}$$

The dimensional transmitted front ripple is assumed to be of the form

$$\Psi_t(y,t) = \tilde{\psi}_t(t)\cos(ky)\ \psi_0. \tag{28}$$

The dimensionless initial shock ripple amplitude is given by $\tilde{\psi}_{t0}$:

$$\tilde{\psi}_{t0} = \frac{\psi_t(t=0+)}{\psi_0} = 1 - \frac{D_t}{D_i}, \tag{29}$$

and, because tangential velocity must be conserved across the corrugated front, an initial tangential velocity perturbation is generated behind it, which is given by

$$\delta v_{ya}^0 = -Uk\psi_{t0}. \tag{30}$$

We define the dimensionless velocity

$$\tilde{v}_{ya}^0 = \frac{\delta v_{ya}^0}{k\psi_0 D_i}. \tag{31}$$

After $t = 0+$, pressure perturbations are created inside the compressed fluid. In linear theory, the usual approach is to solve the wave equation for the pressure perturbations. The dimensionless linearized fluid equations ($x$ and $y$ momentum equations, mass conservation, and entropy conservation) are, respectively,

$$\frac{\partial \tilde{u}_a}{\partial \tau_a} = -\frac{\partial \tilde{p}_a}{\partial kx}, \tag{32a}$$

$$\frac{\partial \tilde{v}_a}{\partial \tau_a} = \tilde{p}_a, \tag{32b}$$

$$\frac{\partial \tilde{\rho}_a}{\partial \tau_a} = -\frac{D_i}{c_{af}}\left(\frac{\partial \tilde{u}_a}{\partial kx} + \tilde{v}_a\right), \tag{32c}$$

$$\frac{\partial \tilde{p}_a}{\partial \tau_a} = \frac{c_{af}}{D_i}\frac{\partial \tilde{\rho}_a}{\partial \tau_a}. \tag{32d}$$

Note that the conservation of entropy for the compressed fluid particles does not strictly imply $\tilde{\rho}_a \propto \tilde{p}_a$. Actually, Eq. (32d) only states that their partial time derivatives are proportional. A first integral of this equation gives a relationship of the form

$$\tilde{\rho}_a(x,t) = \frac{D_i}{c_{af}}\tilde{p}_a(x,t) + f(x), \tag{33}$$

where the function $f(x)$ stands for the generation of entropic perturbations of density, which only depend on space, in the reference frame used [7,25,31]. The above result tells us that density perturbations are composed of an acoustic part (related to the fluctuations in pressure) and an entropic part (due to the conservation of the entropy generated at the shock front) as discussed in [7,25,26]. The strict proportionality between $\tilde{p}$ and $\rho$ is only true for the particles that travel inside the rarefaction fan, inside fluid $b$, because no entropy is generated in this other situation [20].

From now on, we use the coordinate transformation [34]

$$kx = r_a\sinh\chi_a, \quad kc_{af}t = r_a\cosh\chi_a. \tag{34}$$

Combining Eqs. (32), we get the linear wave equation for the pressure perturbations can be written as [7]

$$r_a\frac{\partial^2\tilde{p}_a}{\partial r_a^2} + \frac{\partial\tilde{p}_a}{\partial r_a} + r_a\tilde{p}_a = \frac{\partial\tilde{h}_a}{\partial\chi_a}, \tag{35a}$$

$$\tilde{h}_a = \frac{1}{r_a}\frac{\partial\tilde{p}_a}{\partial\chi_a}. \tag{35b}$$

The solution to the above equations can be found in the form of an infinite series of Bessel functions [7] or in terms of the Laplace transform of the pressure perturbations [11]. As for the first method, it can be seen that

$$\tilde{p}_a(\chi_a,r_a) = \sum_{n=0}^{\infty}\{\pi_{2n+1}^a\cosh[(2n+1)\chi_a] + \omega_{2n+1}^a\sinh[(2n+1)\chi_a]\}J_{2n+1}(r_a), \tag{36}$$

where $J_{2n+1}$ is the ordinary Bessel function of order $2n+1$ [35], and the coefficients $\pi_{2n+1}^a$ and $\omega_{2n+1}^a$ have to be obtained through the boundary conditions at the shock and at the contact surface when matching with the perturbation field inside fluid $b$ [7,8]. We later show an efficient method to calculate $\pi_{2n+1}^m$ and $\omega_{2n+1}^m$ in order to follow the initial transient evolution of the different perturbed quantities.

Before attacking the problem of the temporal evolution, it is very convenient to work with the Laplace transform of the pressure perturbations. Laplace transforms in this work have two goals: on one hand, they will enable us to obtain the coefficients $\pi^a_{2n+1}$, $\omega^a_{2n+1}$, and, besides, to obtain exact analytical formulas for the asymptotic normal and tangential velocities at the rippled contact surface. To this scope, we define the Laplace transforms

$$\tilde{P}_a(\chi_a,s_a) = \int_0^\infty \hat{p}_a(\chi_a,r_a)e^{-r_a s_a}\,dr_a, \tag{37a}$$

$$\tilde{H}_a(\chi_a,s_a) = \int_0^\infty \tilde{h}_a(\chi_a,r_a)e^{-r_a s_a}\,dr_a. \tag{37b}$$

We take the Laplace transform of both Eqs. (35) and make $s_a = \sinh q_a$. After some algebra, the solution to the wave equation can be written, in terms of Laplace transforms, as [11]

$$\tilde{P}_a(\chi_a,q_a) = \frac{F_{a1}(q_a-\chi_a) + F_{a2}(q_a+\chi_a)}{\cosh q_a}, \tag{38a}$$

$$\tilde{H}_a(\chi_a,q_a) = F_{a1}(q_a-\chi_a) - F_{a2}(q_a+\chi_a), \tag{38b}$$

for some functions $F_{a1,2}$. For the sake of simplicity, we use the same notation for the Laplace transform of $\tilde{P}_a$, written indistinctly as a function of $s_a$ in Eq. (37a), or of $q_a$ in Eq. (38a). The same applies to the function $\tilde{H}_a$.

The pressure amplitudes $F_{a1,2}$ are functions to be determined from the boundary and initial conditions. It can be seen that $F_{a1}$ represents pressure perturbations that escape from the contact surface towards the shock, and $F_{a2}$ represent the waves that reach the transmitted shock from downstream [23]. If we take the Laplace transform of Eq. (36) in the domain of the variable $r_a$, we find

$$F_{a1}(q_a) = \frac{1}{2}\sum_{n=0}^{\infty}\left(\pi^a_{2n+1} + \omega^a_{2n+1}\right)e^{-(2n+1)q_a}, \tag{39a}$$

$$F_{a2}(q_a) = \frac{1}{2}\sum_{n=0}^{\infty}\left(\pi^a_{2n+1} - \omega^a_{2n+1}\right)e^{-(2n+1)q_a}. \tag{39b}$$

The functions $F_{a1,2}$ have to be related through the linearized boundary conditions at the shock front, that is, the linearized Rankine-Hugoniot equations [11]. They are written, at first, in the domain of the time variable $r_t = kc_{af}t\sqrt{1-\beta_t^2}$. The relationship between the transmitted shock ripple and the shock pressure perturbations is [see Eq. (18) of [7] or Eq. (13) of [31]]

$$\frac{d\tilde{\psi}_t}{d\tau_a} = \frac{\gamma_a+1}{4\beta_t}\frac{D_i}{c_{af}}\tilde{p}_t. \tag{40}$$

The factor $D_i/c_{af}$ appearing in the right hand side of the former equation is due to the different scaling factor used to define the dimensionless pressure, which is $\rho_{af}c_{af}D_i k\psi_0$ here, in contrast to $\rho_{af}c_{af}^2 k\psi_0$ in [24,31]. The equation that relates the pressure and pressure gradient with the shock ripple just behind the transmitted shock is

$$h_t(r_t) = -\frac{M_t^2+1}{2M_t^2\beta_t}\frac{d\tilde{p}_t}{dr_t} - \frac{\beta_t^2}{\sqrt{1-\beta_t^2}}\left(\frac{\rho_{af}}{\rho_{a0}}-1\right)\tilde{\psi}_t. \tag{41}$$

If we make a Laplace transformation in the domain of the variable $r_t$, we obtain (after making $s_a = \sinh q_a$)

$$\tilde{H}_t(q_a) = \alpha_{a1}(q_a)\tilde{P}_t(q_a) + \alpha_{a2}(q_a), \tag{42}$$

where

$$\alpha_{a1}(q_a) = \alpha_{a10}\sinh q_a + \frac{\alpha_{a11}}{\sinh q_a}, \tag{43a}$$

$$\alpha_{a2}(q_a) = \frac{\alpha_{a20}}{\sinh q_a}, \tag{43b}$$

and

$$\alpha_{a10} = \frac{\kappa_t+\beta_t^2}{2\kappa_t\beta_t}, \tag{44a}$$

$$\alpha_{a11} = \frac{1}{2}\frac{\beta_t}{\kappa_t}\frac{\kappa_t-\beta_t^2}{1-\beta_t^2}\frac{\rho_{af}}{\rho_{a0}}, \tag{44b}$$

$$\alpha_{a20} = -\tilde{v}^0_{ya}\sinh\chi_t. \tag{44c}$$

The parameter $\kappa_t$ is the dimensionless slope of the R-H curve of fluid $a$, evaluated in its final state, and normalized with respect to the adiabatic sound speed of the shocked fluid

$$\kappa_t = \frac{1}{c_{af}^2}\left(\frac{dp}{d\rho}\right)_{\rho_{af}}. \tag{45}$$

Its analytical expression for an ideal gas with isentropic exponent $\gamma_a$ is

$$\frac{1}{\kappa_t} = \frac{1}{4}(\gamma_a-1)^2(1+z_i)\left[1-\frac{\rho_{a0}}{\rho_{af}}\left(\frac{\gamma_a+1}{\gamma_a-1}\right)\right]^2. \tag{46}$$

Finally, after some algebra, we find a relationship between both pressure amplitudes:

$$F_{a2}(q_a) = \frac{\tilde{v}^0_{ya}}{\sinh(q_a-\chi_t)\eta^+(q_a-\chi_t)} - \frac{\eta_t^-(q_a-\chi_t)}{\eta_t^+(q_a-\chi_t)}F_{a1}(q_a-2\chi_t), \tag{47}$$

where $\tanh\chi_t = -\beta_t$ and the functions $\eta_t^\pm$ are defined below:

$$\eta_t^\pm(q_a) = \frac{\alpha_{a1}(q_a)}{\cosh q_a} \pm 1. \tag{48}$$

We see that Eq. (47) is a functional equation. The argument of the unknown function $F_{a1}$ is shifted by $-2\chi_t$. The shift turns out to be an important quantity that can not be neglected for moderate to strong shocks. Physically, it is related to the sound wave reverberation between the contact surface and the ripped transmitted shock front. For very weak shocks ($z_i \ll 1$), it is $\chi_t \propto \ln z_i$. Hence, the shifted argument of $F_{a1}$ in the previous equation becomes infinitely large. As the pressure functions $F_{a1,2}$ behave like decaying exponentials for large absolute values of their arguments, the functional equation becomes a simpler algebraic equation relating $F_{a2}$ and $F_{a1}$. In the very weak shock limit, the sonic perturbations radiated by the contact surface ripple barely catch the transmitted shock, which behaves almost as an isolated shock wave. In the opposite limit ($z_i \gg 1$), it is $\chi_t \sim O(1)$ and, hence, $\chi_t$ can not be neglected inside the argument of $F_{a1}$. In this limit, the velocity of the shock relative to the contact surface decreases, thus enhancing the sonic interaction. We have not enough information inside fluid $a$ in order to solve for the two unknown functions $F_{a1}$ and $F_{a2}$ in the general case because Eq. (47) is a single equation for two unknowns. In order to solve the problem inside fluid $a$, we must also solve the perturbation problem inside fluid $b$ and connect both perturbation fields across the contact surface, by requiring the continuity of pressure and normal velocity perturbations. To perform this task, we must formally solve for the perturbed pressure function inside fluid $b$, and we use the same formalism as in fluid $a$. However, the perturbations growing to the right of the contact surface are also influenced by the perturbations that are generated inside the rarefaction fan, as shown in [6,19,20]. In the next subsection, we review at first the perturbation fields inside the rippled rarefaction wave. After that, the pressure perturbations inside fluid $b$ are solved and the matching of the solutions across the rippled material surface can then be done.

### C. Rarefaction region

For the analysis of the perturbations growing inside the rarefaction fan, we refer to [20]. The results derived there will be later useful in order to describe the perturbations at the rarefaction tail as a function of time and, hence, to later calculate the temporal evolution of the contact surface ripple. We will only briefly review here the main results and refer to [20] for the derivations of the formulas. We work in the Eulerian system of reference that moves with the unperturbed contact surface. We use the definitions

$$\delta v_x(x,y,t) = c_{b1}\tilde{u}_{\mathrm{raref}}(x,t)k\psi_0 \cos ky, \tag{49a}$$

$$\delta v_y(x,y,t) = c_{b1}\tilde{v}_{\mathrm{raref}}(x,t)k\psi_0 \sin ky \tag{49b}$$

for the longitudinal and tangential velocities. Notice that the velocity scale used to measure velocities inside the rarefaction wave is $c_{b1}$ and not $D_i$. The pressure and density perturbations are written as

$$\delta p(x,y,t) = \tilde{p}_{\mathrm{raref}}(x,t)\cos ky \rho_{b1} c_{b1}^2 k\psi_0, \tag{50a}$$

$$\delta \rho(x,y,t) = \tilde{\rho}_{\mathrm{raref}}(x,t)\cos ky \rho_{b1} k\psi_0, \tag{50b}$$

We assume adiabatic flow inside the rarefaction and, hence, $\tilde{p}_{\mathrm{raref}} = \tilde{\rho}_{\mathrm{raref}}$ [see the discussion concerning Eq. (33)] and/or [19,20]. Note that the proportionality factor between the dimensionless pressure and density is unity here because of the different normalization used compared to the relationship between the same quantities in fluid $a$ [see Eq. (32d)]. At $t = 0+$, after the incident shock has been refracted, the rarefaction leading and trailing edges become rippled. The initial dimensionless amplitudes of their ripples are, respectively [6,11],

$$\tilde{\psi}_{rh}^0 = \frac{\psi_{rh}^0}{\psi_0} = 1 - \frac{c_{b1} - U_1}{D_i}, \tag{51a}$$

$$\tilde{\psi}_{rt}^0 = \frac{\psi_{rt}^0}{\psi_0} = 1 + \frac{c_{bf} - U}{D_i}. \tag{51b}$$

As explained in [19], or in [5], immediately after shock refraction, an initial profile of the tangential velocity perturbation is formed inside the centered expansion fan. In terms of the self-similar variable $\zeta$, the distribution of tangential velocity inside the expansion fan at $t = 0+$ is given by

$$\tilde{v}_{\mathrm{raref}}(\zeta, t = 0+) = \frac{1}{\gamma_b + 1}\frac{\tilde{\psi}_{rt}^0 - \tilde{\psi}_{rh}^0}{\zeta_{rh} - \zeta_{rt}}\left(\zeta_{rh}^2 - \zeta^2\right) - \frac{2}{\gamma_b + 1}\left(\frac{\tilde{\psi}_{rt}^0 - \tilde{\psi}_{rh}^0}{\zeta_{rh} - \zeta_{rt}} + \tilde{\psi}_{rt}^0\right)(\zeta_{rh} - \zeta). \tag{52}$$

The perturbations growing inside the expansion fan evolve in time, and for $t > 0$, the tangential velocity fluctuations inside the rarefaction region can be written in the form [17,18,20]

$$\tilde{v}_{\mathrm{raref}}(\xi,\eta) = \sqrt{\xi}\int_1^{\xi} J_0[\sqrt{n_{KH}\eta(\xi - z)}]\frac{dw_0}{dz}, \tag{53}$$

where the new variables $\xi$ and $\eta$ are defined by

$$\xi = A^{\beta}, \quad \eta = (kc_{b1}t)^2 A^{\alpha}, \tag{54}$$

with

$$\alpha = \frac{\gamma_b + 1}{\gamma_b - 1}, \tag{55a}$$

$$\beta = \frac{\gamma_b - 3}{\gamma_b - 1}, \tag{55b}$$

$$n_{KH} = \frac{\gamma_b + 1}{3 - \gamma_b}. \tag{55c}$$

The function $J_0$ is the ordinary Bessel function of order 0 [35,36]. The function $w_0$ is related to the initial tangential velocity profile, in the new variables [17,18,20]. It can be written as

$$w_0(z) = \sum_{j=0}^{2} \alpha_j z^{\epsilon_j}, \tag{56}$$

where the coefficients $\alpha_j$ and the exponents $\epsilon_j$ are given by

$$\alpha_0 = \left[\frac{\zeta_{rh}^2}{\gamma_b + 1} - \frac{4M_1^2}{(\gamma_b^2 - 1)(\gamma_b - 1)}\right]\left[\frac{\tilde{\psi}_{rt}^0 - \tilde{\psi}_{rh}^0}{\zeta_{rh} - M_1}\right] - \left(\frac{2\zeta_{rh}}{\gamma_b + 1} + \frac{4M_1}{\gamma_b^2 - 1}\right)\left[\frac{(\tilde{\psi}_{rt}^0 - \tilde{\psi}_{rh}^0)M_1}{\zeta_{rh} - M_1} + \tilde{\psi}_{rt}^0\right], \tag{57}$$

$$\alpha_1 = \left(\frac{1}{\gamma_b - 1}\right)\left[\frac{(\tilde{\psi}_{rt}^0 - \tilde{\psi}_{rh}^0)M_1}{\zeta_{rh} - M_1} + 2\tilde{\psi}_{rt}^0\right] + \frac{4M_1}{(\gamma_b - 1)^2}\left[\frac{\tilde{\psi}_{rt}^0 - \tilde{\psi}_{rh}^0}{\zeta_{rh} - M_1}\right], \tag{58}$$

$$\alpha_2 = -\frac{\gamma_b + 1}{(\gamma_b - 1)^2}\left[\frac{\tilde{\psi}_{rt}^0 - \tilde{\psi}_{rh}^0}{\zeta_{rh} - M_1}\right], \tag{59}$$

$$\epsilon_0 = -\frac{1}{2}, \quad \epsilon_1 = \frac{\gamma_b + 1}{2\gamma_b - 6}, \quad \epsilon_2 = \frac{3\gamma_b - 1}{2\gamma_b - 6}. \tag{60}$$

### D. Fluid perturbations inside the expanded fluid b

In the space between the contact surface and the rarefaction trailing edge the background mass density is constant and equal to the fluid density at the rarefaction trailing edge: $\rho_{bf}$.

We scale here pressure, density, and velocity perturbations in the form

$$\delta p_b(x,y,t) = \tilde{p}_b(x,t)\cos ky\ \rho_{bf} c_{bf} D_i\ k\psi_0, \quad (61a)$$

$$\delta \rho_b(x,y,t) = \tilde{\rho}_b(x,t)\cos ky\ \rho_{bf}\ k\psi_0, \quad (61b)$$

$$\delta v_{xb}(x,y,t) = \tilde{u}_b(x,t)\cos ky\ D_i\ k\psi_0, \quad (61c)$$

$$\delta v_{yb}(x,y,t) = \tilde{v}_b(x,t)\cos ky\ D_i\ k\psi_0. \quad (61d)$$

We define the variables $\chi_b$ and $r_b$:

$$kx = r_b \sinh \chi_b, \quad kc_{bf} t = r_b \cosh \chi_b. \quad (62)$$

The wave equation can be treated in the same way as in fluid $a$ and its solutions written in a similar form [11]. We show the solution as a function of time and space, in the form

$$\tilde{p}_b(\chi_b,r_b) = \sum_{n=0}^{\infty} \{\pi^b_{2n+1} \cosh[(2n+1)\chi_b] + \omega^b_{2n+1} \sinh[(2n+1)\chi_b]\} J_{2n+1}(r_b). \quad (63)$$

Working with the Laplace transform of the wave equation for the pressure fluctuations inside fluid $b$, we arrive to a similar decomposition, as in fluid $a$:

$$\tilde{P}_b(\chi_b,q_b) = \frac{F_{b1}(q_b-\chi_b) + F_{b2}(q_b+\chi_b)}{\cosh q_b}, \quad (64a)$$

$$\tilde{H}_b(\chi_b,q_b) = F_{b1}(q_b-\chi_b) - F_{b2}(q_b+\chi_b). \quad (64b)$$

Analogously as with fluid $a$, the pressure amplitudes $F_{b1,2}$ can be expressed in terms of the coefficients $\pi^b_{2n+1}$, $\omega^b_{2n+1}$:

$$F_{b1}(q_b) = \frac{1}{2}\sum_{n=0}^{\infty}\left(\pi^b_{2n+1} + \omega^b_{2n+1}\right)e^{-(2n+1)q_b}, \quad (65a)$$

$$F_{b2}(q_b) = \frac{1}{2}\sum_{n=0}^{\infty}\left(\pi^b_{2n+1} - \omega^b_{2n+1}\right)e^{-(2n+1)q_b}. \quad (65b)$$

As discussed in [11], the function $F_{b1}$ is explicitly given by the perturbations growing at the rarefaction trailing edge, inside the rarefaction wave. The explicit formula for the function $F_{b1}(q_b)$ is

$$F_{b1}(q_b) = -\frac{1}{2}\frac{\delta v^0_{yb}}{D_i}e^{q_b} + e^{q_b}\sinh q_b \times \int_0^{\infty} \tilde{v}_{rt}(\tau_b)\exp(-\tau_b e^{q_b})\, d\tau_b, \quad (66)$$

where $\delta v^0_{yb}$ is the (dimensional) initial rarefaction tail tangential velocity, and can be calculated using Eq. (52):

$$\delta v^0_{yb} = \frac{1}{\gamma_b+1}\left[\left(\tilde{\psi}^0_{rt} - \tilde{\psi}^0_{rh}\right)(\zeta_{rh}+\zeta_{rt}) - \frac{2}{\gamma_b+1}\left(\frac{\tilde{\psi}^0_{rt} - \tilde{\psi}^0_{rh}}{\zeta_{rh}-\zeta_{rt}} + \tilde{\psi}^0_{rt}\right)(\zeta_{rh}-\zeta_{rt})\right] c_{b1}. \quad (67)$$

It is convenient to define here a normalized velocity with respect to the incident shock speed ($D_i$), as this is necessary when matching with the velocity perturbations at the contact surface. We define, for later use,

$$\tilde{v}^0_{yb} = \frac{\delta v^0_{yb}}{k\psi_0 D_i} = \frac{c_{b1}}{D_i}\left(a + b\ \zeta_{rt} + c\ \zeta^2_{rt}\right), \quad (68)$$

where

$$a = \frac{\zeta^2_{rh}}{\gamma_b+1}\frac{\tilde{\psi}^0_{rt} - \tilde{\psi}^0_{rh}}{\zeta_{rh}-\zeta_{rt}} - \frac{2\zeta_{rh}}{\gamma_b+1}\left[\frac{\left(\tilde{\psi}^0_{rt} - \tilde{\psi}^0_{rh}\right)\zeta_{rt}}{\zeta_{rh}-\zeta_{rt}} + \tilde{\psi}^0_{rt}\right], \quad (69a)$$

$$b = \frac{2}{\gamma_b+1}\left[\frac{\left(\tilde{\psi}^0_{rt} - \tilde{\psi}^0_{rh}\right)\zeta_{rt}}{\zeta_{rh}-\zeta_{rt}} + \tilde{\psi}^0_{rt}\right], \quad (69b)$$

$$c = -\frac{1}{\gamma_b+1}\frac{\tilde{\psi}^0_{rt} - \tilde{\psi}^0_{rh}}{\zeta_{rh}-\zeta_{rt}}, \quad (69c)$$

as defined in [11].

The function $\tilde{v}_{rt}$ inside the integral in Eq. (66) is the dimensionless rarefaction tail tangential velocity as a function of dimensionless time $\tau_b = kc_{bf}t$. We use Eq. (53) to write the function $\tilde{v}_{rt}$, after noting that the time inside the rarefaction is scaled with $c_{b1}$:

$$\tilde{v}_{rt}(\tau_b) = \tilde{v}_{raref}\left(\xi = M_1^{\beta}, \eta = \tau_b M_1^{\alpha-2}\right), \quad (70)$$

where $\beta = (\gamma_b-3)/(\gamma_b-1)$ and $\alpha = (\gamma_b+1)/(\gamma_b-1)$. After some algebra, we obtain

$$F_{b1}(q_b) = -\frac{\tilde{v}^0_{yb}}{2}\ e^{q_b} + \xi^{1/2}_{rt}\frac{c_{b1}}{D_i}e^{q_b}\sinh q_b \times \int_1^{\xi_{rt}} \frac{dw_0}{dz}\left[e^{2q_b} + nM_1^{-\beta}(\xi_{rt}-z)\right]dz. \quad (71)$$

The integral in the above equation can be obtained analytically in terms of known transcendent functions. An exact analytical expression for $F_{b1}$, not reported before, is given by the following lengthy expression:

$$F_{b1}(q_b) = -\frac{\tilde{v}^0_{yb}}{2}\ e^{q_b} + \frac{c_{bf}}{D_i}\xi^{1/2}_{rt}e^{q_b}\sinh(q_b)\Lambda(q_b), \quad (72)$$

where

$$\Lambda(q_b) = \frac{b_1\xi^{\Psi_1+1}_{rt}}{\sqrt{n_{KH}}}\left\{2\left(\frac{e^{2q}}{n_{KH}}+1\right)^{\Psi_1}\sqrt{\frac{e^{2q}}{n_{KH}} - \frac{1}{\xi_{rt}} + 1}\ {}_2F_1\left[\frac{1}{2}, -\Psi_1; \frac{3}{2}; 1 - \frac{1}{\left(1+\frac{e^{2q}}{n_{KH}}\right)\xi_{rt}}\right] - 2\sqrt{\frac{e^{2q}}{n_{KH}}}\left(\frac{e^{2q}}{n_{KH}}+1\right)^{\Psi_1} {}_2F_1\left(\frac{1}{2}, -\Psi_1; \frac{3}{2}; 1 - \frac{1}{1+\frac{e^{2q}}{n_{KH}}}\right)\right\}$$

$$
\begin{aligned}
&+\frac{b_2\xi_{rt}^{\Psi_2+1}}{\sqrt{n_{KH}}}\left\{2\left(\frac{e^{2q}}{n_{KH}}+1\right)^{\Psi_2}\sqrt{\frac{e^{2q}}{n_{KH}}-\frac{1}{\xi_{rt}}+1}\,{}_2F_1\left[\frac{1}{2},-\Psi_2;\frac{3}{2};1-\frac{1}{\left(1+\frac{e^{2q}}{n_{KH}}\right)\xi_{rt}}\right]\right.\\
&\left.-2\sqrt{\frac{e^{2q}}{n_{KH}}}\left(\frac{e^{2q}}{n_{KH}}+1\right)^{\Psi_2}{}_2F_1\left(\frac{1}{2},-\Psi_2;\frac{3}{2};1-\frac{1}{1+\frac{e^{2q}}{n_{KH}}}\right)\right\}\\
&+\frac{b_3\xi_{rt}^{\Psi_3+1}}{\sqrt{n_{KH}}}\left\{2\left(\frac{e^{2q}}{n_{KH}}+1\right)^{\Psi_3}\sqrt{\frac{e^{2q}}{n_{KH}}-\frac{1}{\xi_{rt}}+1}\,{}_2F_1\left[\frac{1}{2},-\Psi_3;\frac{3}{2};1-\frac{1}{\left(1+\frac{e^{2q}}{n_{KH}}\right)\xi_{rt}}\right]\right.\\
&\left.-2\sqrt{\frac{e^{2q}}{n_{KH}}}\left(\frac{e^{2q}}{n_{KH}}+1\right)^{\Psi_3}{}_2F_1\left(\frac{1}{2},-\Psi_3;\frac{3}{2};1-\frac{1}{1+\frac{e^{2q}}{n_{KH}}}\right)\right\},
\end{aligned}
\tag{73}
$$

in which ${}_2F_1(z_1,z_2;z_3;z_4)$ is the Gauss hypergeometric series [35,36], and

$$
\begin{aligned}
&\mu_1=\frac{\gamma_b+1}{\gamma_b-1},\quad \mu_2=-\frac{2M_1}{\gamma_b-1},\quad n_{KH}=\frac{\gamma_b+1}{3-\gamma_b},\quad b_1=\epsilon_0\left(a+b\mu_2+c\mu_2^2\right),\\
&b_2=\epsilon_1(b\mu_1+2c\mu_1\mu_2),\quad b_3=\epsilon_2c\mu_1^2,\quad \Psi_1=-\frac{3}{2},\quad \Psi_2=\frac{7-\gamma_b}{2\gamma_b-6},\quad \Psi_3=\frac{\gamma_b+5}{2\gamma_b-6},
\end{aligned}
\tag{74}
$$

where $\epsilon$ and $\alpha$ were defined in Eqs. (57)–(60).

In order to later calculate $\pi_{2n+1}^m$ and $\omega_{2n+1}^m$, it is convenient to have an expansion of $F_{b1}$ in powers of $e^{-q_b}$. This can be done by using Eq. (72) written above. However, a much simpler way is to make an expansion in powers of $e^{-q_b}$ directly inside the integrand in Eq. (71). We obtain

$$
F_{b1}(q_b)=\sum_{n=0}^{\infty}f_{b1}^{2n+1}e^{-(2n+1)q_b}\equiv\sum_{n=0}^{\infty}\Theta[\Xi(n+1)-\Xi(n)]e^{-(2n+1)q_b},
\tag{75}
$$

where

$$
\begin{aligned}
\Theta&=\frac{\sqrt{\xi_{rt}}}{2}\frac{c_{bf}}{D_i},\quad \delta=\frac{\gamma_b-1}{\gamma_b-3},\\
\Xi(n)&=\frac{(-1)^n(n_{KH})^n}{2\sqrt{\pi}\Gamma(n+1)\Gamma\left(n+\delta+\frac{1}{2}\right)\Gamma\left(n+2\delta+\frac{1}{2}\right)\xi_{rt}}\\
&\quad\times\left\{c(4\delta-1)\mu_1^2\Gamma\left(2\delta-\frac{1}{2}\right)\Gamma\left(n+\frac{1}{2}\right)\Gamma(n+1)\Gamma\left(n+\delta+\frac{1}{2}\right)\xi_{rt}^{2\delta+\frac{1}{2}}\right.\\
&\quad+\Gamma\left(n+2\delta+\frac{1}{2}\right)\left[(2c\mu_2+b)(2\delta-1)\mu_1\Gamma\left(\delta-\frac{1}{2}\right)\Gamma\left(n+\frac{1}{2}\right)\Gamma(n+1)\xi_{rt}^{\delta+\frac{1}{2}}\right.\\
&\quad-2\Gamma\left(n+\delta+\frac{1}{2}\right)\sqrt{\xi_{rt}}(-\sqrt{\pi}[(c\mu_2+b)\mu_2+a])\Gamma(n+1)\\
&\quad+\Gamma\left(n+\frac{1}{2}\right)\sqrt{\xi_{rt}}\left([(c\mu_2+b)\mu_2+a]{}_2F_1\left(-\frac{1}{2},-n;\frac{1}{2};\frac{1}{\xi_{rt}}\right)\right.\\
&\quad\left.\left.\left.+\ \mu_1\left(c\mu_1\,{}_2F_1\left(-n,2\delta-\frac{1}{2};2\delta+\frac{1}{2};\frac{1}{\xi_{rt}}\right)+(2c\mu_2+b)\right){}_2F_1\left(-n,\delta-\frac{1}{2};\delta+\frac{1}{2};\frac{1}{\xi_{rt}}\right)\right)\right]\right\}.
\end{aligned}
\tag{76}
$$

### E. Functional equation for $F_{a1}$

We can match the perturbation fields at both sides of the contact surface requiring the continuity of pressure and normal velocity at both sides of $x=0$. We write this set of conditions in terms of the Laplace transforms in the way

$$R\tilde{P}_a(\chi_a=0,q_a)=\tilde{P}_b(\chi_b=0,q_b), \tag{77a}$$
$$\tilde{H}_a(\chi_a=0,q_a)=\tilde{H}_b(\chi_b=0,q_b), \tag{77b}$$

which can be rewritten in terms of the functions $F_{m1,2}$ using Eq. (38) as

$$R\frac{\cosh q_b}{\cosh q_a}[F_{a1}(q_a)+F_{a2}(q_a)]=F_{b1}(q_b)+F_{b2}(q_b), \tag{78a}$$
$$F_{a1}(q_a)-F_{a2}(q_a)=F_{b1}(q_b)-F_{b2}(q_b). \tag{78b}$$

When matching the perturbation fields at the contact surface, the following relationship between $s_a$ and $s_b$ has been used: $N\sinh q_a=\sinh q_b$. In the above system of equations

[Eq. (78)], we remind that $F_{b1}(q_b)$ is already given by Eq. (72), which is information given at the rarefaction tail. Besides, the linearized Rankine-Hugoniot conditions give us a relationship between $F_{a1}$ and $F_{a2}$ in Eq. (47). Therefore, we have a linear system of four equations to solve for the four pressure amplitudes $F_{m1,2}$ $(m = a, b)$. After some algebra, we arrive to a single functional equation for $F_{a1}$:

$$F_{a1}(q_a) = \phi_{a1}(q_a) + \phi_{a2}(q_a)F_{a1}(q_a - 2\chi_t), \qquad (79)$$

where [11]

$$\phi_{a1}(q_a) = \frac{2}{\Delta+1}F_{b1}(q_b) - \frac{\Delta-1}{\Delta+1}\frac{\delta v_{ya}^0 \sinh\chi_t}{\eta_t^+(q_a-\chi_t)\sinh q_a - \chi_t}, \qquad (80a)$$

$$\phi_{a2}(q_a) = \frac{\Delta-1}{\Delta+1}\frac{\eta_t^-(q_a-\chi_t)}{\eta_t^+(q_a-\chi_t)}, \qquad (80b)$$

and

$$\Delta = R\frac{\cosh q_b}{\cosh q_a}. \qquad (81)$$

We can solve it by iterations, as shown in [11]. We need a starting function to initiate the iteration sequence. It can be easily obtained by solving Eq. (79) for $q_a \gg -2\chi_t$. We get

$$F_{a1}^{[0]}(q_a) = \frac{\phi_{a1}(q_a)}{1-\phi_{a2}(q_a)}. \qquad (82)$$

The $n$th step in the iteration sequence is then

$$F_{a1}^{[n]}(q_a) = \sum_{l=0}^{n}\left[\phi_{a1}(q_a - 2l\chi_t)\prod_{j=0}^{l-1}\phi_{a2}(q_a - 2j\chi_t)\right] + \left[\prod_{l=0}^{n}\phi_{a2}(q_a - 2l\chi_t)\right]F_{a1}^{[0]}(q_a - 2n\chi_t),$$
$$n \geqslant 1. \qquad (83)$$

The above functional equation has been discussed for the first time in [11] and in [14] to calculate the asymptotic velocity at the contact surface ripple. We use it here with the same purpose, but also to calculate the Bessel series coefficients $\pi_{2n+1}^a$ and $\omega_{2n+1}^a$ in Eq. (36) in order to follow the initial transient of the pressure perturbations. It is noted that $F_{b1}(q_b)$ inside the expression for $\phi_{a1}(q_a)$ [Eq. (80a)] is understood as a function of $q_a$ through the relationship $N\sinh q_a = \sinh q_b$.

### F. Time evolution of the pressure perturbations

#### *1. Bessel series for arbitrary values of position and time*

According to Eq. (36), we can follow the transient growth of the perturbations at any position if we have the coefficients $\pi_{2n+1}^a$ and $\omega_{2n+1}^a$. This denumerable set of numbers can be obtained with the aid of the Laplace transforms developed in the previous subsections. Our task in this section is to build the equations that enable us to calculate $\pi_{2n+1}^a$ and $\omega_{2n+1}$. If we write the pressure perturbations $\tilde{P}_a$ and $\tilde{H}_a$ at the contact surface (at $x = 0$ or, equivalently, $\chi_a = 0$), we have

$$\tilde{P}_{ai}(q_a) = \frac{F_{a1}(q_a)+F_{a2}(q_a)}{\cosh q_a} = \sum_{n=0}^{\infty}\pi_{2n+1}^a\frac{\left(\sqrt{s_a^2+1}-s_a\right)^{2n+1}}{\sqrt{s_a^2+1}}, \qquad (84a)$$

$$\tilde{H}_{ai}(q_a) = F_{a1}(q_a) - F_{a2}(q_a) = \sum_{n=0}^{\infty}\omega_{2n+1}^a\left(\sqrt{s_a^2+1}-s_a\right)^{2n+1}, \qquad (84b)$$

where the subindex $i$ indicates the location of the contact surface. Besides, the Laplace transforms of the Bessel functions have also been used [35,36]. From the linearized Rankine-Hugoniot relationship at the transmitted shock front [Eq. (47)] we know that $F_{a2}$ is related to $F_{a1}$. Therefore, the left hand sides of Eq. (84) are known in terms of $F_{a1}$ which is the solution to the functional equation (79). Therefore, the desired coefficients $\pi_{2n+1}^a$ and $\omega_{2n+1}^a$ could be obtained through a convenient series expansion of $F_{a1}$ and $F_{a2}$ in powers of $1/s_a$. We make

$$F_{a1}(q_a) = \sum_{n=0}^{\infty}\frac{f_{2n+1}^{a1}}{s_a^{2n+1}}, \qquad (85a)$$

$$F_{a2}(q_a) = \sum_{n=0}^{\infty}\frac{f_{2n+1}^{a2}}{s_a^{2n+1}}. \qquad (85b)$$

The idea is to substitute Eq. (85a) inside Eq. (79), expand both members in powers of $1/s_a$, and obtain an infinite system of equations, from which the coefficients $f_{2n+1}^{a1}$ can be retrieved. Then, substituting both expansions given by Eqs. (85) inside Eq. (47), another system of equations can be constructed to obtain the coefficients $f_{2n+1}^{a2}$, as functions of $f_{2n+1}^{a1}$. A recurrence equation to calculate $f_{2n+1}^{a1}$ can be easily implemented inside a *Mathematica* notebook or a similar mathematical software. All we need is to expand the functions $\phi_{a1}$, $\phi_{a2}$ and the shifted function $F_{a1}(q_a - 2\chi_t)$ and equate equal powers in $1/s_a$. The general term would be too large to be written here and be of practical use. We only show the first two coefficients. We have

$$f_1^{a1} = \frac{1}{2N}\frac{\beta_t N(NR-1) + (\beta_t+1)(\alpha_{a10}+1)\Theta[\Xi(1)-\Xi(0)]}{\beta_t + NR + (\beta_t NR+1)\alpha_{a10}} \qquad (86)$$

and

$$f_3^{a1} = \frac{1}{8N^3\left(\nu_1^{f_3^a} + \nu_2^{f_3^a}\alpha_{a10} + \nu_3^{f_3^a}\alpha_{a10}^2\right)}\Big[-2\beta_t N^2\left(\sigma_1^{f_3^a} + \sigma_2^{f_3^a}\alpha_{a10} + \sigma_3^{f_3^a}\alpha_{a11}\right) + (\beta_t+1)\Theta[\Xi(1)-\Xi(0)]\left(\sigma_4^{f_3^a} + \sigma_5^{f_3^a}\alpha_{a10} + \sigma_6^{f_3^a}\alpha_{a10}^2 + \sigma_7^{f_3^a}\alpha_{a11}\right) + (\beta_t+1)^3\Theta[\Xi(2)-\Xi(1)]\left(\sigma_8^{f_3^a} + \sigma_9^{f_3^a}\alpha_{a10} + \sigma_{10}^{f_3^a}\alpha_{a10}^2\right)\Big], \qquad (87)$$

where

$$
\begin{aligned}
\sigma_1^{f_{a1}^3} &= 2R^2N^3\beta_t^2 + R\big[N^2\big(2\beta_t^3+\beta_t^2+4\beta_t+1\big)-(\beta_t+1)^3\big] - N\beta_t\big(\beta_t^2+1\big),\\
\sigma_2^{f_{a1}^3} &= 2R^2N^3\beta_t^3 - R\big[N^2\beta_t\big(\beta_t^2-6\beta_t-3\big)+(\beta_t+1)^3\big] - N\big(3\beta_t^2-1\big),\\
\sigma_3^{f_{a1}^3} &= 2\big[R^2N^3\beta_t\big(\beta_t^2-1\big)+RN^2\big(-\beta_t^3+\beta_t^2+\beta_t-1\big)-N\big(\beta_t^2-1\big)\big],\\
\sigma_4^{f_{a1}^3} &= R[2N^3(3\beta_t+1)-3N(\beta_t+1)^2]+2N^2\beta_t(\beta_t-1)-\beta_t(\beta_t+1)^2,\\
\sigma_5^{f_{a1}^3} &= R[8N^3\beta_t(\beta_t+1)-3N(\beta_t+1)^3]+2N^2\big(\beta_t^3-\beta_t^2-\beta_t+1\big)-(\beta_t+1)^3,\\
\sigma_6^{f_{a1}^3} &= RN\beta_t[2N^2\beta_t(\beta_t+3)-3(\beta_t+1)^2]-2N^2\beta_t(\beta_t-1)-(\beta_t+1)^2,\\
\sigma_7^{f_{a1}^3} &= 4N^2\big(\beta_t^3-\beta_t^2-\beta_t+1\big)[RN-1],\\
\sigma_8^{f_{a1}^3} &= RN+\beta_t,\\
\sigma_9^{f_{a1}^3} &= (\beta_t+1)[RN+1],\\
\sigma_{10}^{f_{a1}^3} &= RN\beta_t+1,\\
\nu_1^{f_{a1}^3} &= R^2N^2\big(3\beta_t^2+1\big)+4RN\beta_t\big(\beta_t^2+1\big)+\beta_t^2\big(\beta_t^2+3\big),\\
\nu_2^{f_{a1}^3} &= 4R^2N^2\beta_t\big(\beta_t^2+1\big)+2RN\big(\beta_t^4+6\beta_t^2+1\big)+4\beta_t\big(\beta_t^2+1\big),\\
\nu_3^{f_{a1}^3} &= R^2N^2\beta_t^2\big(\beta_t^2+3\big)+4RN\beta_t\big(\beta_t^2+1\big)+3\beta_t^2+1.
\end{aligned} \tag{88}
$$

Once we have the coefficients $f_{2n+1}^{a1}$, we substitute the series for $F_{a1}$ inside Eq. (84). Expanding both members in powers of $1/s_a$ we obtain the quantities $\pi_{2n+1}^a$ and $\omega_{2n+1}^a$. The equations can be easily implemented inside a *Mathematica* notebook or any similar software, and solve them for arbitrary values of $n$. Writing the general term would be of little practical value, as the analytical expressions soon become cumbersome [32]. We only show here the first two coefficients in each fluid, $\pi_1^a$, $\pi_3^a$ and $\omega_1^a$, $\omega_3^a$:

$$
\pi_1^a = \frac{2}{N}\,\frac{-\beta_tN+(\beta_t\alpha_{\mathrm{a}10}+1)\Theta[\Xi(1)-\Xi(0)]}{\beta_t+NR+(\beta_tNR+1)\alpha_{\mathrm{a}10}} \tag{89}
$$

and

$$
\begin{aligned}
\pi_3^a = {}& \frac{2}{N^3\big(\nu_1^{\pi_3^a}+\nu_2^{\pi_3^a}\alpha_{\mathrm{a}10}+\nu_3^{\pi_3^a}\alpha_{\mathrm{a}10}^2\big)}\big[N^2\beta_t\delta v_{ya}^0\big(\sigma_1^{\pi_3^a}+\sigma_2^{\pi_3^a}\alpha_{\mathrm{a}10}+\sigma_3^{\pi_3^a}\alpha_{\mathrm{a}11}\big)\\
&+\Theta[\Xi(1)-\Xi(0)]\big(\sigma_4^{\pi_3^a}+\sigma_5^{\pi_3^a}\alpha_{\mathrm{a}10}+\sigma_6^{\pi_3^a}\alpha_{\mathrm{a}10}^2+\sigma_7^{\pi_3^a}\alpha_{\mathrm{a}11}\big)+\Theta[\Xi(2)-\Xi(1)]\big(\sigma_8^{\pi_3^a}+\sigma_9^{\pi_3^a}\alpha_{\mathrm{a}10}+\sigma_{10}^{\pi_3^a}\alpha_{\mathrm{a}10}^2\big)\big],
\end{aligned} \tag{90}
$$

where

$$
\begin{aligned}
\sigma_1^{\pi_3^a} &= R\big[N^2\big(-5\beta_t^2-3\big)+6\beta_t^2+2\big]+N\beta_t\big(\beta_t^2-1\big),\\
\sigma_2^{\pi_3^a} &= R\beta_t\big[N^2\big(\beta_t^2-9\big)+2\beta_t^2+6\big]+3N\big(\beta_t^2-1\big),\\
\sigma_3^{\pi_3^a} &= -4N\big(\beta_t^2-1\big)[RN\beta_t+1],\\
\sigma_4^{\pi_3^a} &= \big(3\beta_t^2+1\big)(N^2-1)[3RN+\beta_t],\\
\sigma_5^{\pi_3^a} &= 12RN\beta_t\big(\beta_t^2+1\big)(N^2-1)+N^2\big(3\beta_t^4+2\beta_t^2+3\big)-\beta_t^4-6\beta_t^2-1,\\
\sigma_6^{\pi_3^a} &= \beta_t\big(\beta_t^2+3\big)(N^2-1)[3RN\beta_t+1],\\
\sigma_7^{\pi_3^a} &= -4N^2\big(\beta_t^2-1\big)^2,\\
\sigma_8^{\pi_3^a} &= \big(3\beta_t^2+1\big)[RN+\beta_t],\\
\sigma_9^{\pi_3^a} &= 4RN\beta_t\big(\beta_t^2+1\big)+\beta_t^4+6\beta_t^2+1,\\
\sigma_{10}^{\pi_3^a} &= \beta_t\big(\beta_t^2+3\big)[RN\beta_t+1],\\
\nu_1^{\pi_3^a} &= \nu_1^{f_3^{a1}},\quad \nu_2^{\pi_3^a} = \nu_2^{f_3^{a1}},\quad \nu_3^{\pi_3^a} = \nu_3^{f_3^{a1}},
\end{aligned} \tag{91}
$$

$$
\omega_1^a = \frac{2}{N}\,\frac{\beta_tN^2R+(\alpha_{\mathrm{a}10}+\beta_t)\Theta[\Xi(1)-\Xi(0)]}{\beta_t+NR+(\beta_tNR+1)\alpha_{\mathrm{a}10}}, \tag{92}
$$

and

$$\omega_3^a = \frac{2}{N^3\left(\nu_1^{\omega_3^a} + \nu_2^{\omega_3^a}\alpha_{a10} + \nu_3^{\omega_3^a}\alpha_{a10}^2\right)}\left[RN^2\beta_t\delta v_{ya}^0\left(\sigma_1^{\omega_3^a} + \sigma_2^{\omega_3^a}\alpha_{a10} + \sigma_3^{\omega_3^a}\alpha_{a11}\right)\right.$$
$$+\Theta[\Xi(1)-\Xi(0)]\left(\sigma_4^{\omega_3^a} + \sigma_5^{\omega_3^a}\alpha_{a10} + \sigma_6^{\omega_3^a}\alpha_{a10}^2 + \sigma_7^{\omega_3^a}\alpha_{a11}\right)$$
$$\left.+\Theta[\Xi(2)-\Xi(1)]\left(\sigma_8^{\omega_3^a} + \sigma_9^{\omega_3^a}\alpha_{a10} + \sigma_{10}^{\omega_3^a}\alpha_{a10}^2\right)\right], \tag{93}$$

where

$$\begin{aligned}
\sigma_1^{\omega_3^a} &= -RN^3\left(\beta_t^2-1\right) - N^2\beta_t\left(3\beta_t^2+5\right) + 2\beta_t\left(\beta_t^2+3\right),\\
\sigma_2^{\omega_3^a} &= -3RN^3\beta_t\left(\beta_t^2-1\right) - N^2\left(9\beta_t^2-1\right) + 6\beta_t^2+2,\\
\sigma_3^{\omega_3^a} &= 4N^2\left(\beta_t^2-1\right)[RN\beta_t+1],\\
\sigma_4^{\omega_3^a} &= \beta_t\left(\beta_t^2+3\right)(N^2-1)[3RN+\beta_t],\\
\sigma_5^{\omega_3^a} &= RN\left[N^2\left(\beta_t^4+22\beta_t^2+1\right) - 3\left(\beta_t^4+6\beta_t^2+1\right)\right] + 4\beta_t\left(\beta_t^2+1\right)(N^2-1),\\
\sigma_6^{\omega_3^a} &= \left(3\beta_t^2+1\right)(N^2-1)[3RN\beta_t+1],\\
\sigma_7^{\omega_3^a} &= 4RN^3\left(\beta_t^2-1\right)^2,\\
\sigma_8^{\omega_3^a} &= \beta_t\left(\beta_t^2+3\right)[RN+\beta_t],\\
\sigma_9^{\omega_3^a} &= RN\left(\beta_t^4+6\beta_t^2+1\right) + 4\beta_t\left(\beta_t^2+1\right),\\
\sigma_{10}^{\omega_3^a} &= \left(3\beta_t^2+1\right)[RN\beta_t+1],\\
\nu_1^{\omega_3^a} &= \nu_1^{f_3^{a1}}, \quad \nu_2^{\omega_3^a} = \nu_2^{f_3^{a1}}, \quad \nu_3^{\omega_3^a} = \nu_3^{f_3^{a1}}.
\end{aligned} \tag{94}$$

#### 2. *Taylor series in time for the shock pressure perturbations*

An alternative way of studying the temporal evolution of the shock pressure perturbations consists in using an expansion in powers of time, as done in [6,19]. We write the Taylor series for the pressure perturbation at the transmitted shock:

$$\tilde{p}_t(r_t) = \sum_{n=0}^{\infty} \frac{p_{t0}^{(2n+1)}}{(2n+1)!}\, r_t^{2n+1}, \tag{95}$$

where $r_t = \tau_a/\cosh\chi_t = \tau_a\sqrt{1-\beta_t^2}$ and $p_{t0}^{(2n+1)}$ is the $2n+1$ derivative of the shock pressure perturbation (with respect to the variable $r_t$) at $t = 0+$. Our task in this subsection is to build the equations that allow us to find the quantities $p_{t0}^{(2n+1)}$. If we make a Laplace transform of the above equation, we get

$$\tilde{P}_t(s_a) = \sum_{n=0}^{\infty} \frac{p_{t0}^{(2n+1)}}{s_a^{2n+2}}. \tag{96}$$

According to Eqs. (38), (39), (47), and (85), the derivatives $p_{t0}^{(2n+1)}$ are combinations of the quantities $f_{2n+1}^{a1}$. However, it is simpler to relate the derivatives $p_{t0}^{(2n+1)}$ with the Bessel series coefficients $\pi_{2n+1}^a$ and $\omega_{2n+1}^a$. According to Eq. (36), we write the pressure perturbation at the shock in the form

$$\tilde{p}_t(r_t) = \sum_{n=0}^{\infty} D_{2n+1}^t J_{2n+1}(r_t), \tag{97}$$

where $D_{2n+1}^t = \pi_{2n+1}^a \cosh[(2n+1)\chi_t] + \omega_{2n+1}^a \sinh[(2n+1)\chi_t]$. The Laplace transform of Eq. (97) is

$$\tilde{P}_t(s_a) = \sum_{n=0}^{\infty} D_{2n+1}^t \frac{\left(\sqrt{s_a^2+1}-s_a\right)^{2n+1}}{\sqrt{s_a^2+1}}. \tag{98}$$

After expanding the right hand side of Eq. (98) in powers of $1/s_a$ and equating with Eq. (96) we can retrieve the general term $p_{t0}^{(2n+1)}$. The two first initial derivatives are

$$p_{t0}^{(1)} = \frac{D_1^t}{2}, \quad p_{t0}^{(3)} = \frac{D_3^t - 3D_1^t}{8}, \tag{99}$$

and the general term $p_{t0}^{(2n+1)}$ can be easily calculated, for example, inside a *Mathematica* notebook.

### G. Time evolution of the transmitted shock ripple

The shock ripple evolution is directly calculated by integrating Eq. (40) [7]. If we use the Bessel functions series for the transmitted shock pressure perturbation, we get

$$\tilde{\psi}_t(r_t) = \tilde{\psi}_{t0} J_0(r_t) - \frac{(\gamma_a+1)}{2\beta_t\sqrt{1-\beta_t^2}}\frac{D_i}{c_{af}}\sum_{n=0}^{\infty} D_{2n+1}^t \times\left[\sum_{k=1}^{n} J_{2k}(r_t)\right], \tag{100}$$

where we remind that $r_t = kc_{af}t\sqrt{1-\beta_t^2}$. On the other hand, with the Taylor series, we get

$$\tilde{\psi}_t(r_t) = \tilde{\psi}_{t0} + \frac{(\gamma_a+1)}{4\beta_t\sqrt{1-\beta_t^2}}\frac{D_i}{c_{af}}\sum_{n=0}^{\infty} p_{t0}^{2n+1}\frac{r_t^{2n+2}}{(2n+2)!}. \tag{101}$$

### H. Time evolution of the rarefaction tail ripple

To calculate the time evolution of the rarefaction tail corrugation, we follow [20], specifically its Eq. (58). We take care that in the results presented in [20], the dimensionless time is scaled with $kc_{b1}$. That is, the nondimensional time in [20] is $\tau_{\rm raref}$. Therefore, we have

$$\tilde{\psi}_{rt}(\tau_{\rm raref}) = \tilde{\psi}_{rt}^0 + \frac{3-\gamma_b}{4M_1}\left\{\frac{D_i}{c_{b1}}\tilde{v}_{yb}^0 - \tilde{v}_{rt}(\tau_{\rm raref}) - \tau_{\rm raref}M_1^{\frac{-2}{\gamma_b-1}}\sqrt{n_{KH}}\int_1^{\xi_{rt}}\frac{dw_0(z)}{dz}\frac{j_1\left[\tau_{\rm raref}\sqrt{M_1^{(\gamma_b+1)/(\gamma_b-1)}n_{KN}(\xi_{rt}-z)}\right]}{\sqrt{\xi_{rt}-z}}dz\right\}, \tag{102}$$

where the function $\tilde{v}_{rt}(\tau_{\rm raref})$ is given by

$$\tilde{v}_{rt}(\tau_b) = \tilde{v}_{\rm raref}(\xi_{rt},\eta_{rt}), \tag{103a}$$

$$\xi_{rt} = M_1^{(\gamma_b-3)/(\gamma_b-1)}, \tag{103b}$$

$$\eta_{rt} = \tau_{\rm raref}^2 M_1^{(\gamma_b+1)/(\gamma_b-1)}. \tag{103c}$$

Besides, the function $j_1$ is given by

$$j_1(x) = xJ_0(x) - J_1(x) + \frac{\pi x}{2}[J_1(x)\boldsymbol{H}_0(x) - J_0(x)\boldsymbol{H}_1(x)]. \tag{104}$$

$\boldsymbol{H}_\nu$ are ordinary Struve functions. The initial tangential velocity $\tilde{v}_{yb}^0$ is writen in Eq. (152), $w_0(z)$ in Eq. (56), and $n_{KH}$ in Eq. (74). In [20], it was demonstrated that the normal velocity at the trailing edge reaches an asymptotic value in time. Thanks to this, we write a formula valid in the linear asymptotic regime in the form

$$\tilde{\psi}_{rt}(t\to\infty) \cong u_{rt}^{\infty}\,\tau_{\rm raref}. \tag{105}$$

There is no asymptotic ordinate to the origin for the trailing edge ripple growth. The normal velocity $u_{rt}^{\infty}$ is taken from Eq. (61) of [20]:

$$u_{rt}^{\infty} = \frac{c_{b1}}{D_i}\frac{\gamma_b-3}{4}\xi_{rt}\sqrt{n_{KH}}\int_1^{\xi_{rt}}\frac{dw_0(z)}{dz}\frac{1}{\sqrt{\xi_{rt}-z}}dz. \tag{106}$$

### I. Vorticity generated by the transmitted shock and asymptotic velocities at the contact surface ripple

#### 1. Differential equations

After $t = 0+$, the rippled wavefronts escape from the contact surface. The transmitted shock front generates vorticity inside fluid $a$. On the contrary, no vorticity is created inside fluid $b$. At each side of the contact surface, we have a steady velocity field of the form ($m = a$ or $b$)

$$\vec{v}_m(x,y) = (u_m(x)\cos ky, v_m(x)\sin ky). \tag{107}$$

The vorticity inside fluid $a$ can be expressed in dimensionless form, as [7,15,25]

$$\tilde{\omega}_a(x,y) = \frac{\delta\omega_a(x,y)}{kD_i} = g_a(\tilde{x})\sin ky, \tag{108}$$

where $\tilde{x} = kx$, and the function $g_a$ is given by

$$g_a(\tilde{x}) = \Omega_a\tilde{p}_t[t = -x/(D_t-U)] \equiv \Omega_a\tilde{p}_t[r_t = -\tilde{x}/\sinh\chi_t)]. \tag{109}$$

In the above equation, $\tilde{p}_t$ refers to the pressure perturbation at the transmitted shock. As the shock moves away, the pressure perturbations show a damped oscillatory behavior in time. In consequence, according to Eq. (109), this temporal behavior of the pressure fluctuations translates into a spatial damped oscillatory pattern for the vorticity spread inside fluid $a$. The important information expressed by Eq. (109) is that the vorticity at position $x$ is proportional to the value of the pressure perturbation at the transmitted shock at the time the shock front arrived to that position. In other words, vorticity stored in the bulk is the memory of the compressible history of the shock ripple oscillations. The quantity $\Omega_a$ is given by [8]

$$\Omega_a = -\frac{(M_t^2-1)\sqrt{2\gamma_a M_t^2-\gamma_a+1}}{M_t^2\left[(\gamma_a-1)M_t^2+2\right]^{3/2}}. \tag{110}$$

For large times, when the rippled wavefronts have separated off the contact surface, at least a perturbation wavelength, we can assume that the pressure perturbation field becomes negligible near the material surface and the velocity perturbations become incompressible [8,10,11]. It can be seen, that for large times, the dimensionless velocity components satisfy the ordinary differential equations

$$\frac{d^2u_a}{d\tilde{x}^2} - u_a = -g_a(\tilde{x}), \tag{111a}$$

$$\frac{d^2u_b}{d\tilde{x}^2} - u_b = 0, \tag{111b}$$

where $g_a$ is given above by Eq. (109) and is necessary in order to calculate the vorticity generated by the transmitted shock inside fluid $a$. Inside fluid $b$ there is no vorticity and the velocity field simply decays exponentially. The tangential component of the velocity ($v$) is easily obtained from the previous equations because of the asymptotic incompressibility of the perturbation field, which in our units is simply written as

$$v = -\frac{du}{d\tilde{x}}. \tag{112}$$

The fact that $g_a \neq 0$ implies that the normal and tangential velocities at the contact surface ripple inside fluid $a$ are different. Their difference becomes more important in regimes where shock compression is important. Let $u_i$ indicate the dimensionless normal velocity at the interface and $v_{ia}$ the dimensionless tangential velocity. It can be seen that

$$u_i + v_{ia} = -\Omega_a \sinh\chi_t \tilde{P}_t(q_a = -\chi_t) = F_a, \tag{113a}$$

$$u_i = v_{ib}, \tag{113b}$$

where $F_a$ is the dimensionless form of $\mathcal{F}_a$ [see Eq. (4)]. We see that $F_a \propto \int_0^\infty \tilde{p}_t(r)\exp(-r\sinh\chi_t)\,dr$ is essentially a weighted average of the vorticity spread inside fluid $a$.

To close the equations system above, we need another relationship between the asymptotic velocities. It comes from integrating the $y$ component of the linearized momentum equation at $x = 0$, and we obtain [8,11]

$$\rho_{af}\left(v_{ia} - \tilde{v}_{ya}^0\right) = \rho_{bf}\left(u_i - \tilde{v}_{yb}^0\right). \tag{114}$$

Using $R = \rho_{af}/\rho_{bf}$ [see Eq. (15)], we obtain

$$u_i = \frac{\tilde{v}_{yb}^0 - R\tilde{v}_{ya}^0}{R+1} + \frac{RF_a}{R+1}, \tag{115a}$$

$$v_{ia} = -\frac{\tilde{v}_{yb}^0 - R\tilde{v}_{ya}^0}{R+1} + \frac{F_a}{R+1}, \tag{115b}$$

$$v_{ib} = u_i. \tag{115c}$$

The first term in the above equations is only dependent on the initial tangential velocities generated by the rippled wavefronts at both sides of the material interface and is enough to estimate the asymptotic velocities for weak shocks. The second term is proportional to the vorticity integrated inside fluid $a$, which is represented by the parameter $F_a$, and is necessary when one reaches shock compression becomes important. This is typically the case when the incident shock Mach number increases beyond 1.5 and/or any of the fluids' isentropic exponent approaches unity.

#### 2. Calculation of $F_a$

The quantity $F_a$ can be obtained after some careful algebra [10,11]:

$$F_a = \left[1 + \frac{M_t^2}{M_t^2 - 1}\frac{4(D_t - U)}{U}\right]^{-1}\left[\tilde{v}_{ya}^0 - 2F_{a1}(-2\chi_t)\right]. \tag{116}$$

The main difficulty in obtaining $F_a$ is that we must get $F_{a1}(-2\chi_t)$ from Eq. (79). It must be solved by iterations as shown in Eqs. (82) and (83). The number of iteration steps will be dependent on the values of the four preshock parameters and $n$ might increase if $M_i$ increases and/or $\gamma_m \to 1$. For most of the cases, and especially those found in the experiments discussed later, it is enough considering $n = 0$, that is, without iteration. We call $F_a^{[0]}$ the corresponding value and thus we can write

$$F_a^{[0]} = \left[1 + \frac{M_t^2}{M_t^2 - 1}\frac{4(D_t - U)}{U}\right]^{-1}\left[\tilde{v}_{ya}^0 - 2F_{a1}^{[0]}(-2\chi_t)\right]. \tag{117}$$

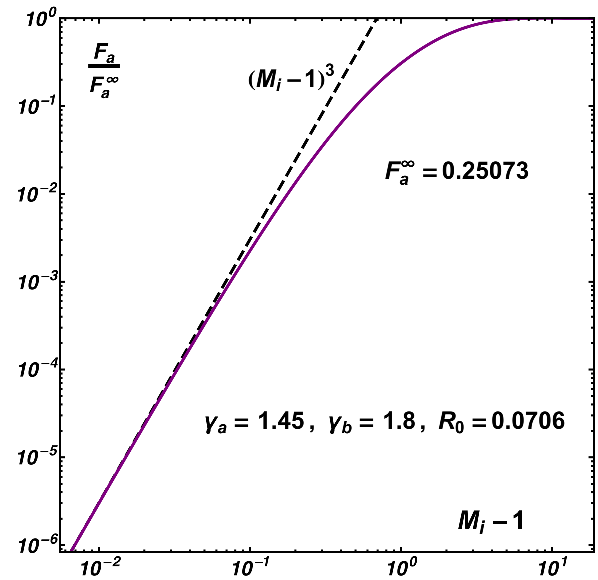


FIG. 2. Bulk vorticity parameter $F_a$ in units of $F_a^\infty$ as a function of $M_i - 1$ for the preshock conditions indicated in the legend.

The function $F_{a1}^{[0]}(-2\chi_t)$ has been shown in Eq. (82). The quantity $F_a^{[0]}$ is the simplest analytical expression that contains information of the vorticity field created by the transmitted shock inside fluid $a$, which is a necessary ingredient to estimate the asymptotic linear velocities in regimes where compressibility is important.

In Fig. 2 we show $F_a$, normalized with its value at high compression. For large Mach numbers, the parameter $F_a$ saturates at $F_a^\infty \cong 0.250\,73$ for the preshock parameters chosen in Fig. 2. At low compression, it is seen that $F_a \propto (M_i - 1)^3$.

### J. Velocity perturbations at the contact surface ripple as a function of time

Having obtained the variation of the pressure perturbation field in space and time between the fronts, it is possible to obtain the velocity fields in space and time too. In this section, we will concentrate at the contact surface ripple and follow the growth in time of the normal and tangential velocities. We can calculate the time evolution either via a Bessel series representation or with a Taylor series of powers in time. Both approaches are detailed below.

#### 1. Time evolution with Bessel series

As has been already shown in [15] for the shock reflected case, the Bessel series representation of the normal velocity of the ripple is a good mathematical choice, as it depends on the value of the asymptotic normal velocity $\delta v_i^\infty = u_i D_i\, k\, \psi_0$, thus becoming a convenient tool to evaluate the goodness of the approximation done in calculating $u_i$. The same feature is observed here for the rarefaction reflected case. We must integrate Eq. (32a) at $x = 0$ in time. We define $\tilde{u}_{ai}(\tau_a) = \tilde{u}_a(x = 0, \tau_a)$, the subindex $i$ indicates the contact surface location:

$$\frac{\partial \tilde{u}_{ai}}{\partial \tau_a} = -\tilde{h}_a(\chi_a = 0,\tau_a) \equiv -\tilde{h}_{ai}(\tau_a). \tag{118}$$

The dimensionless function $\tilde{h}_a$ is defined in Eq. (35b). After using known properties of the Bessel functions [35,36], we obtain, after time integration,

$$\frac{1}{\psi_0}\frac{d\psi_i}{d\tau_a} = \frac{D_i}{c_{af}}u_i\left\{\tau_a J_0(\tau_a) + \frac{\pi\tau_a}{2}[J_1(\tau_a)\boldsymbol{H}_0(\tau_a) - J_0(\tau_a)\boldsymbol{H}_1(\tau_a)] - J_1(\tau_a)\right\} + \frac{4}{\tau_a}\frac{D_i}{c_{af}}\sum_{n=0}^{\infty}\omega_{2n+1}^{a}\left[\sum_{l=1}^{n} l J_{2l}(\tau_a)\right], \tag{119}$$

where $J_\nu(x)$ are ordinary Bessel functions of order $\nu$ and $\boldsymbol{H}_\nu(x)$ are Struve functions of order $\nu$ [35,36].

As for the tangential velocity at the contact surface on side $a$, we must integrate Eq. (32b) in time at $x = 0$. We define $\tilde{v}_{ai}(\tau_a) = \tilde{v}_a(x = 0,\tau_a)$:

$$\frac{\partial \tilde{v}_{ai}}{\partial \tau_a} = \tilde{p}(\chi_a = 0,\tau_a) \equiv \tilde{p}_{ai}(\tau_a). \tag{120}$$

After integrating in time, we have [35,36]

$$\tilde{v}_{ai}(\tau_a) = \tilde{v}_{ya}^0 + \left(v_{ia} - \tilde{v}_{ya}^0\right)[1 - J_0(\tau_a)] - 2\sum_{n=0}^{\infty}\omega_{2n+1}^{a}\sum_{k=1}^{n} J_{2k}(\tau_a). \tag{121}$$

### 2. Time evolution with a Taylor series in powers of time

The Taylor series representation is equivalent to the Bessel series solution discussed above. To obtain it, we work with the Laplace transforms of the quantities at $x = 0$. We multiply both sides of Eqs. (118) and (120) by $e^{-s_a\tau_a}$ and integrate between 0 and $\infty$ to obtain

$$s_a\tilde{U}_{ai}(s_a) = -\tilde{H}_{ai}(s_a), \tag{122a}$$

$$s_a\tilde{V}_{ai}(s_a) = \tilde{v}_{ya}^0 + \tilde{P}_{ai}(s_a), \tag{122b}$$

where the initial condition of zero normal velocity at $x = 0$ has been used. Besides, the initial value of the tangential velocity behind the transmitted shock front $\tilde{v}_{ya}^0$ has also been used. The symbol $\tilde{U}_{ia}$ stands for the Laplace transform of $\tilde{u}_{ia}$ and $\tilde{V}_{ia}$ for $\tilde{v}_{ia}$.

Thanks to Eqs. (84) and (85) we know that

$$\tilde{P}_{ai} = \frac{1}{\sqrt{s_a^2+1}}\sum_{n=0}^{\infty}\frac{f_{a1}^{2n+1} + f_{a2}^{2n+1}}{s_a^{2n+1}}, \tag{123a}$$

$$\tilde{H}_{ai} = \sum_{n=0}^{\infty}(2n+1)\frac{\left(f_{a1}^{2n+1} - f_{a2}^{2n+1}\right)}{s_a^{2n+1}}, \tag{123b}$$

where the procedure to calculate $f_{2n+1}^{a1}$ and $f_{2n+1}^{a2}$ has been discussed before. Besides, we propose

$$\tilde{P}_{ai} = \sum_{n=0}^{\infty}\frac{p_{i0}^{(2n+1)}}{s_a^{2n+2}}, \tag{124a}$$

$$\tilde{H}_{ai} = \sum_{n=0}^{\infty}\frac{h_{i0}^{(2n+2)}}{s_a^{2n+1}}. \tag{124b}$$

If we expand Eqs. (123) and equate equal power terms in $1/s_a$ with the corresponding expansions defined in Eqs. (124), we get the coefficients $p_{i0}^{(2n+1)}$ and $h_{j0}^{(2n+1)}$, which are essential to determine the functions $\tilde{U}_{ia}$ and $\tilde{V}_{ia}$. In fact, substituting inside Eqs. (122) we have

$$\tilde{U}_{ai} = -\sum_{n=0}^{\infty}\frac{h_{i0}^{(2n+2)}}{s_a^{2n+2}}, \tag{125a}$$

$$\tilde{V}_{ai} = \frac{\tilde{v}_{ya}^0}{s_a} + \sum_{n=0}^{\infty}\frac{p_{i0}^{(2n+1)}}{s_a^{2n+3}}. \tag{125b}$$

If we make an inverse Laplace transform of the above equations, we obtain

$$\tilde{u}_{ai}(\tau_a) = -\sum_{n=0}^{\infty}\frac{h_{i0}^{2n+1}}{(2n+1)!}\tau_a^{2n+1}, \tag{126a}$$

$$\tilde{v}_{ai}(\tau_a) = \tilde{v}_{ya}^0 + \sum_{n=0}^{\infty}\frac{p_{i0}^{2n+1}}{(2n+2)!}\tau_a^{2n+2}. \tag{126b}$$

## K. Contact surface ripple growth as a function of time

The results of experiments are usually shown as plots of the contact surface ripple as a function of time. Our model equations provide us with the time evolution of the contact surface normal velocity, which after time integration give the evolution of $\psi_i(t)$. The mathematical procedure is essentially the same as followed in [15].

The ripple amplitude $\psi_i(t)$ is obtained by direct integration in time of the normal velocity $\delta v_i(t)$ at the material interface:

$$\psi_i(t) = \psi_0^* + \int_{0+}^{t}\delta v_i(t')\,dt', \tag{127}$$

where

$$\psi_0^* = \left(1 - \frac{U}{D_i}\right)\psi_0 \tag{128}$$

is the post-shock value of the ripple amplitude at $t = 0+$. After using known properties of the Bessel functions and the recurrence relationships (11.2.6) together with Eq. (11.3.22) of [36], we arrive to the following analytical result:

$$\psi_i(t) = \psi_0^* + \psi_0 \frac{D_i}{c_{af}} u_i \left( \tau_a \left\{ \tau_a J_0(\tau_a) + \frac{\pi \tau_a}{2} [J_1(\tau_a) \boldsymbol{H}_0(\tau_a) - J_0(\tau_a) \boldsymbol{H}_1(\tau_a)] - J_1(\tau_a) \right\} - 1 + J_0(\tau_a) \right)$$
$$+ \psi_0 \frac{D_i}{c_{af}} \sum_{n=0}^{\infty} 2\omega_{2n+1}^a \sum_{l=1}^{n} \left[ 1 - \frac{2}{\tau_a} \sum_{k=1}^{l} (2k-1) J_{2k-1}(\tau_a) \right]. \tag{129}$$

We can also obtain the asymptotic behavior of $\psi_i(t)$. We define the Laplace transform of $\psi_i(t)/\psi_0$ as

$$\tilde{\xi}_i(s_a) = \frac{1}{\psi_0} \int_{0+}^{\infty} \psi_i(\tau_a) e^{-s_a \tau_a} d\tau_a. \tag{130}$$

Taking the Laplace transform of Eq. (127), using the above definition, and substituting inside Eq. (122a), we get

$$s_a \left[ s_a \tilde{\xi}_i(s_a) - \frac{\psi_0^*}{\psi_0} \right] = -\frac{D_i}{c_{af}} \frac{H_{ai}(s_a)}{s_a}. \tag{131}$$

We make a Taylor expansion of $H_{ai}(s_a)$ in powers of $s_a$, and after some algebraic work, we arrive to

$$\tilde{\xi}_i(s_a) \cong \left[ \frac{\psi_0^*}{\psi_0} - \frac{D_i}{c_{af}} H'_{ai}(0) \right] \frac{1}{s_a} + \frac{D_i}{c_{af}} \frac{u_i}{s_a^2} + O(1). \tag{132}$$

If we make an inverse Laplace transform, and reminding that $\delta v_i^{\infty} = u_i k \psi_0 D_i$, we arrive to the result, written in dimensional form

$$\psi_i(t \gg t_1) \cong \psi_{\infty} + \delta v_i^{\infty} t, \tag{133}$$

where $\psi_{\infty}$ is an asymptotic ordinate, given by

$$\psi_{\infty} = \psi_0^* - \frac{D_i}{c_{af}} [F'_{a1}(0) - F'_{a2}(0)] \psi_0, \tag{134}$$

and the prime to the right of the functions $F_{a1,2}$ indicates the derivative with respect to their argument. An accurate method to calculate $\psi_{\infty}$ is detailed in the Appendix.

The characteristic time $t_1$, inside the argument of $\psi$ in the left hand side of Eq. (133), defines the duration of the transient phase, within linear theory, before the asymptotic is reached. As observed in [15], a qualitative interpretation of $\psi_{\infty}$ can be obtained, considering very large times inside Eq. (127). After rearranging terms, we find

$$\psi_{\infty} - \psi_0^* = \int_{0+}^{\infty} [\delta v_i(t) - \delta v_i^{\infty}] dt, \tag{135}$$

which tells us that $\psi_{\infty} - \psi_0^*$ is a measure of the area difference between $\delta v_i(t)$ and $\delta v_i^{\infty}$ in a time plot of the normal velocity evolution. We can see this in Fig. 3(a) for a specific choice of the preshock parameters. The shaded area represents the difference $[\psi_{\infty} - \psi_0^*]/\psi_0$.

If we define the dimensionless time $\tau_d = k\delta v_i^{\infty} t$ and plot the difference $[\psi_i(t) - \psi_{\infty}]/\psi_0$, all the curves would asymptotically collapse into a single straight line of slope 45°. The universal scaling can be recognized in Fig. 3(b), where the complete and asymptotic formulas are shown together for several choices of the preshock parameters. Each curve joins the asymptotic straight line at a different dimensionless time $\tau_{d1}$, which would be a function of the four preshock quantities.

We clearly notice the subtle sound wave reverberations for the more compressible cases.

Meyer and Blewett had also observed a behavior like the one predicted by Eq. (133) in [4]. They concluded that the asymptotic ordinate measured from their simulations was quite different from $\psi_0^*$. Our Eqs. (133) and (134) answer the question posed by them as early as 1974.

The contact surface ripple amplitude can also be obtained by time integration of Eq. (126a), and get an expansion in powers of time:

$$\psi_i(\tau_a) = \psi_0^* - \psi_0 \frac{D_i}{c_{af}} \sum_{n=0}^{\infty} \frac{h_{i0}^{2n+1}}{(2n+2)!} \tau_a^{2n+2}. \tag{136}$$

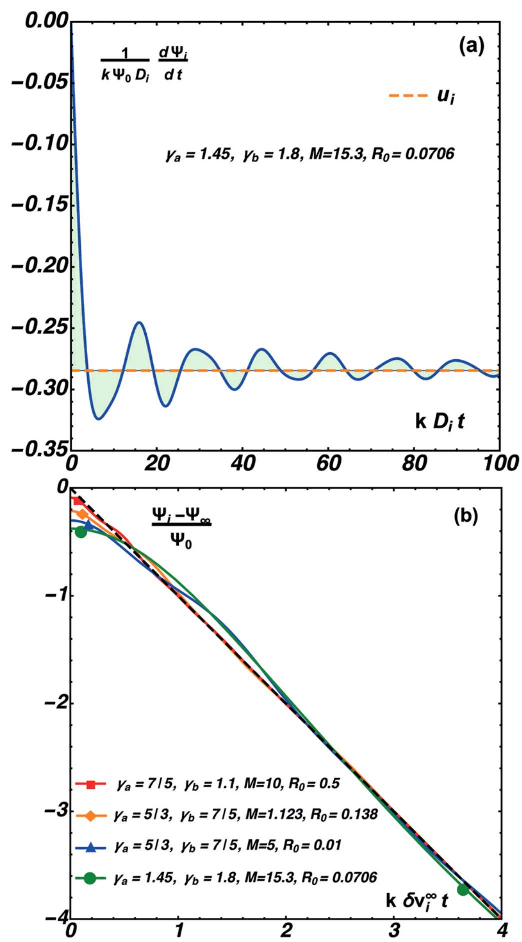


FIG. 3. (a) Time evolution of the contact surface normal velocity in units of $kD_i t$ for the preshock parameters shown in the legend. The physical meaning of the shaded area is explained in the text. (b) Contact surface ripple amplitude, inferred from Eq. (133), in units of $k\delta v_i^{\infty} t$. Different initial conditions are considered and the corresponding preshock parameters are indicated in the legend.

### L. Calculation of the asymptotic velocity field in both fluids

We deal now with the velocity fields that remain in the compressed and expanded fluids at both sides of the contact surface when the corrugated fronts are far. Once the pressure perturbations emitted by the rippled rarefaction and shock fronts become negligible, the density perturbations tend to a constant function of space inside fluid $a$, essentially given by the amount of entropy generated at the transmitted shock front. The density perturbations inside fluid $b$ vanish for large times, as no entropy has been generated by the rarefaction fan. As a consequence, the velocity fields become incompressible, but not irrotational, and Eqs. (111) hold. The most general solution of Eq. (111) is

$$u_a(\tilde{x}) = u_i\, e^{\tilde{x}} + u_{ap}(\tilde{x}), \quad x \leqslant 0 \tag{137a}$$

$$u_b(\tilde{x}) = u_i\, e^{-\tilde{x}}, \quad x \geqslant 0 \tag{137b}$$

where $u_{ap}$ is a particular solution of Eq. (111) in fluid $a$. Since in fluid $b$ there is no vorticity, the complete solution is equal to the homogeneous part and $u_{bp}(\tilde{x}) = 0$. In the shocked fluid, we propose a particular solution in the form of a Taylor series:

$$u_{ap}(\tilde{x}) = \sum_n \frac{\theta_n}{n!}\tilde{x}^n. \tag{138}$$

If we substitute Eq. (138) into Eq. (111), we obtain the following recurrence equation for the coefficients $\theta_n$:

$$\theta_{2n+1} = \theta_{2n-1} - \Omega_a \frac{p_{t0}^{(2n-1)}}{\sinh^{2n-1}\chi_t}, \quad n \geqslant 1 \tag{139}$$

where use has been made of Eqs. (109) and (95) for the pressure perturbation evaluated at the shock front. To calculate the first coefficient $\theta_1$, it is necessary to introduce Eq. (137) in Eq. (112) evaluated at $x = 0$, and we obtain

$$u_i + u'_{ap}(0) = -v_{ai}, \tag{140}$$

from which we finally get

$$\theta_1 = -F_a. \tag{141}$$

The asymptotic tangential velocity $v(x)\sin ky$ is easily obtained from the above results, noting that, because of incompressibility, it is $v(x) = -u'(x)$.

We show next the solution of the above differential equations. This is done in Fig. 4, where the asymptotic velocity profiles inside both fluids are plotted as a function of the spatial coordinates. The incident shock has $M_i = 15.3$. The gases have $\gamma_a = 1.45$ and $\gamma_b = 1.8$. The preshock density ratio is $R_0 = 0.0706$. The solution to the asymptotic equations for both components of the velocity field gives rise to the continuous curves shown in Fig. 4. The values of the dimensionless normal and tangential velocities at the contact surface are, for this case,

$$u_i = u_a(x = 0) = u_b(x = 0) = -0.284\,575, \tag{142a}$$

$$v_{ia} = v_a(x = 0) = 0.536\,345, \tag{142b}$$

$$v_{ib} = v_b(x = 0) = u_i = -0.284\,575. \tag{142c}$$

If we assume that the velocity field is irrotational on both sides of the contact surface, we would obtain the dotted lines shown. On the side of fluid $b$, this is correct because the rarefaction does not generate any vorticity inside the expanded fluid. However, inside fluid $a$, the situation is the opposite. The high Mach number of the incident shock makes such an approximation an unrealistic assumption. In fact, as we can see from Fig. 4(a), the normal velocity changes phase at the position $x \sim -\lambda/10$, to change phase again at $x \sim -\lambda/3$, etc., due to the vorticity field inside that fluid. Besides, it is noted that an irrotational assumption inside fluid $a$ would predict a tangential velocity as indicated with the dotted line in Fig. 4(b) which is quite different from the correct solution shown as the continuous green curve. In Fig. 4(c), we show the density map of the vorticity profile. It is interesting to see that the first vortex to the left of the material surface has been generated inside a distance $\sim\lambda/3$. The proportionality factor between the longitudinal size of the vortex and $\lambda$ is a function of the four preshock parameters. This factor decreases below unity in the high compression limit and increases in the limit of very weak shocks. In [24] the size of the first vortices near the interface has been analytically studied for the shock reflected case and analytical estimates have been given in the weak shock limit for different boundary conditions downstream the shock. For the rarefaction reflected situation, this will be done in a future work. The size observed for the vortices generated by the transmitted front sets another characteristic length, aside from $\lambda$, that could be important for more exact nonlinear models of the RMI.

### M. Kinetic energy

Once we have the asymptotic velocity profiles, we are able to calculate the perturbed kinetic energy stored in the bulk. The kinetic energy, per unit length in the $\hat{z}$ direction, is

$$\delta e^m_{\rm kin}(x,y) = \rho_{mf}\frac{1}{2}\int_0^y \int_0^x \left[\delta v^2_{xm}(x')\cos^2 ky' + \delta v^2_{ym}(x')\sin^2 ky'\right]dx'\,dy', \tag{143}$$

where $x$ and $y$ are lengths of the integration domain. Due to the symmetry in the $\hat{y}$ axis, it is reasonable to consider the energy stored inside a vorticity strip inside fluid $a$ of Fig. 3 of dimensions $(0,x) \times (0,y)$. If we take $y = \lambda/2$, we obtain

$$\delta e^m_{\rm kin}\left(x,\frac{\lambda}{2}\right) = \rho_{mf} D_i^2 \psi_0^2 \frac{\pi}{4} I_{\rm kin}(\tilde{x}). \tag{144}$$

For a rotational field like $(u_a, v_a)$, $I_{\rm kin}(\tilde{x})$ must be carefully evaluated using Eqs. (137) and (112):

$$I_{\rm kin}(\tilde{x}) = \int_0^{\tilde{x}} \left[u_m^2(\tilde{x}') + v_m^2(\tilde{x}')\right]d\tilde{x}'. \tag{145}$$

However, for an irrotational velocity field, it is simply given by

$$I^{irr}_{\rm kin}(\tilde{x}) = u_i^2(1 - e^{-2|\tilde{x}|}). \tag{146}$$

It is noted that Mikaelian had also calculated the kinetic energy content in a RM environment like the one considered here [29] using the impulsive prescription for the ripple's normal velocity, which amounts to using the irrotational estimation. We plot $I_{\rm kin}(\tilde{x})$ as a function of $x/\lambda$ in Fig. 5. We remind here

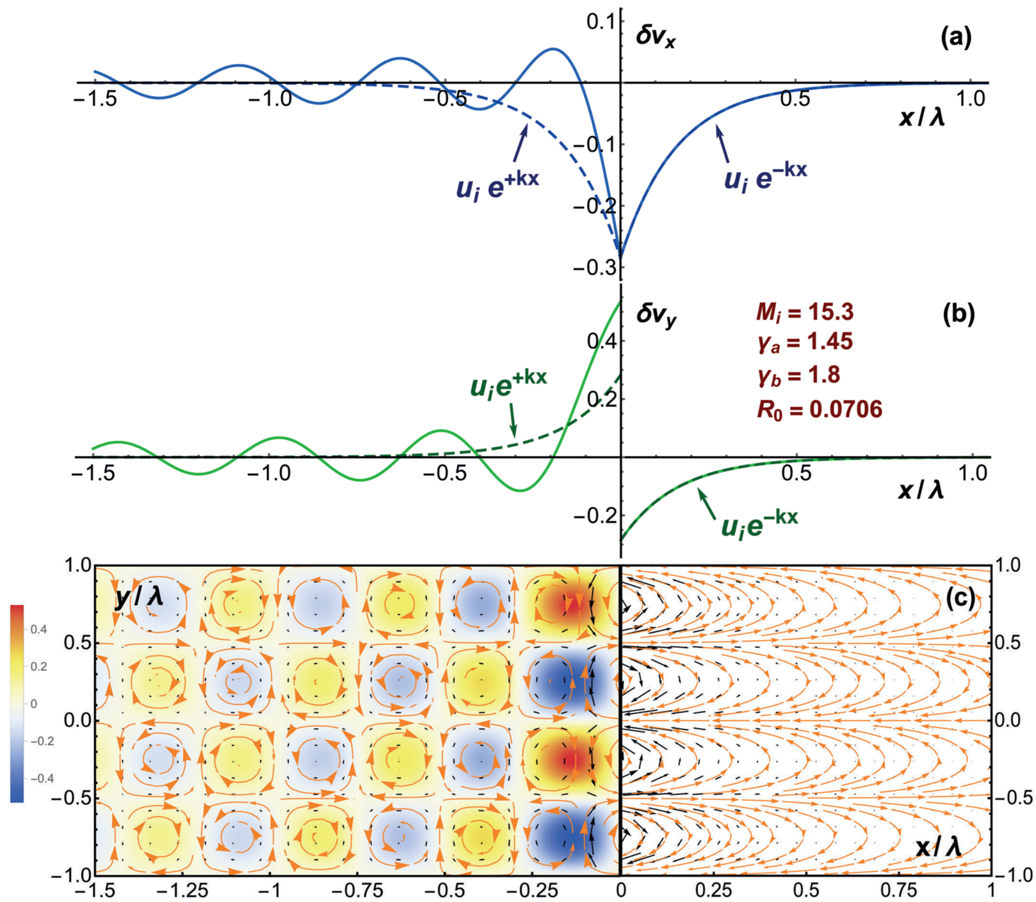


FIG. 4. Asymptotic velocity fields at both sides of the contact surface together with the vorticity generated in the bulk of fluid $a$ by the transmitted shock. The preshock parameters are shown inside the figure and correspond to one of the experiments described in [13]. (a) Normal velocity perturbations in both fluids. The solid curves are the exact solution to Eqs. (111) and (112). Dotted lines show, instead, a hypothetical irrotational approximation for the same velocity fields. The differences between the continuous and the dotted curves are discussed in the text. (b) Tangential velocity perturbations in both fluids. (c) Vorticity density maps and streamlines in both fluids.

that $\tilde{x} = kx$. This graph shows how the kinetic energy is stored inside fluid $a$. At first, we realize that the energy predicted by Eq. (145) is greater than the irrotational approximation given

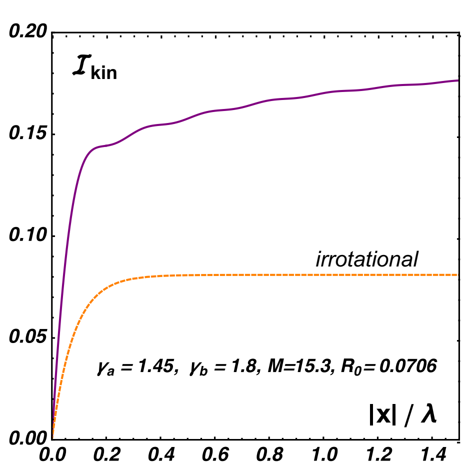


FIG. 5. $I_{\text{kin}}$ as a function of $x/\lambda$ for the preshock parameters indicated inside the figure. The purple solid line is given by Eq. (145) and the irrotational approximation represented by the orange dashed line is the result of Eq. (146).

by Eq. (146). Besides, most of the energy is concentrated very near the contact surface. Indeed, we see that almost 80% of the total energy is concentrated within a layer of width $\sim 0.3\lambda$. Most of the bulk kinetic energy falls inside the first vortex strip for this set of preshock parameters. This fact is in qualitative agreement whit recent simulations [30]. In Fig. 6(a), we show the kinetic energy stored in fluid $a$ up to a distance $x/\lambda = -1.5$ as a function of the incident Mach number. The energy scale has been chosen independent of $M_i$. We realize that a rotational field stores more energy than a completely irrotational flow, due to the non-negligible motion trapped inside the vortices. In the plot we see that the irrotational prescription is only valid for weak shocks, usually for incident Mach numbers less than 1.4. This is consistent with the results shown in the next section. Despite the fact that irrotational estimations of the normal velocity are reasonable in some cases, even for strong shocks, the same is not true for the tangential velocity in the compressed fluid. Because of vorticity, both velocities will increase their difference with shock Mach number and, hence, rotational kinetic energy will be larger. To conclude, it is interesting to compare $\delta e^{m}_{\text{kin}}$ with the background value. After simple algebra, we get the zero order kinetic energy per unit length inside a rectangular strip of

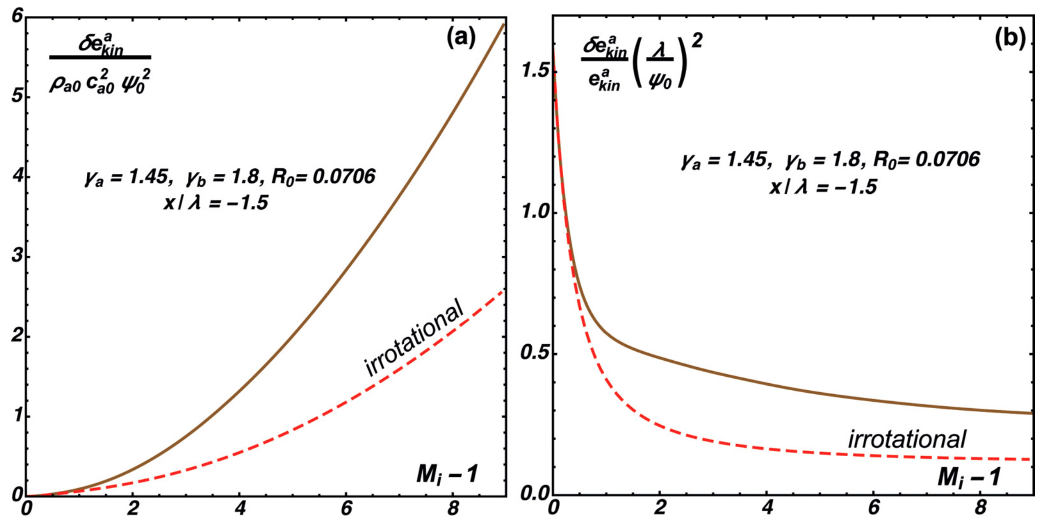


FIG. 6. (a) The kinetic energy per unit $\hat{z}$-length storage in any vorticity strip inside fluid $a$ up to $x/\lambda = -1.5$ as a function of the incident shock Mach number. The red dashed line is the irrotational approximation. (b) The ratio between perturbed and background kinetic energy inside a strip of dimension $(\tilde{x} \times \lambda/2)$ of the fluid $a$ up to $x/\lambda = -1.5$. The red dashed line is the irrotational approximation. The preshock parameters are the same in both plots and they are written inside each figure.

dimensions $x \times \lambda/2$:

$$e^m_{\mathrm{kin}}\left(x,\frac{\lambda}{2}\right) = \rho_{mf} U^2 \lambda^2 \frac{|\tilde{x}|}{8\pi}. \tag{147}$$

The ratio between both quantities can be written as

$$\frac{\delta e^m_{\mathrm{kin}}}{e^m_{\mathrm{kin}}} = \frac{2\pi^2}{|\tilde{x}|}\left(\frac{\psi_0}{\lambda}\right)^2\left(\frac{D_i}{U}\right)^2 I_{\mathrm{kin}}(\tilde{x}). \tag{148}$$

In Fig. 6(b), we plot the above energy ratio inside fluid $a$ up to $x/\lambda = -1.5$ as a function of $M_i$. We observe that the ratio starts at a value equal to $\frac{2\pi^2}{|\tilde{x}|} A_T^2 (1 - e^{-2|\tilde{x}|})$ and decreases as the shock becomes stronger, reaching an asymptotic value for very strong shocks. As before, the irrotational approximation is only valid in the weak shock limit. The distribution of kinetic energy might be important for the problem of re-shock at the material surface as well as an important theoretical tool useful in the elaboration of more exact nonlinear models. A careful and detailed study of the dependence of $\delta e^m_{\mathrm{kin}}(x,y)$ as a function of the preshock parameters and the corresponding scalings laws will be the subject of a future work.

### N. Contact surface asymptotic normal velocity in the form of a Taylor series in powers of a small parameter $\varepsilon$: $\varepsilon = M_i - 1$, $\varepsilon = 1/M_i$, $\varepsilon = R_0^{tt} - R_0$, $\varepsilon = R_0 - R_0^{\mathrm{crit}}$, and $\varepsilon = R_0 - R_0^{\mathrm{min}}$

In the previous subsections, we have learned how to solve the perturbed fluid equations in both fluids when a rarefaction is reflected. The velocity fields have been studied as a function of time, and explicit analytical formulas for the asymptotic velocities have been obtained valid in the whole parameter space. It is very tempting to study the limiting expressions of the asymptotic normal velocity in different physical limits. This can be done by expanding in a Taylor series of the corresponding small parameter in the limit considered. We explain below the method we have used to calculate $u_i$ as a Taylor series in powers of $\varepsilon = M_i - 1$. The calculations described in this section are intended to help with the calculations followed in the corresponding *Mathematica* file attached in the Supplemental Material [37], as they are very lengthy. Similar reasonings are straightforward if we want Taylor expansions in any of the other physical limits. The only difference is that for the other small parameters, the quantity $F_a$ is taken from the corresponding expansion of the quantity $F^{[0]}_{a1}(-2\chi_t)$. The files are ready to use, after we provide the necessary preshock parameters at the beginning.

All the perturbed quantities explicitly depend on $z_i$ and $z_t$. Therefore, obtaining an expansion of $z_t$ in powers of $z_i$, in the weak shock limit, is essential to get the Taylor polynomial for $u_i$. In Eq. (18), we propose an expansion of the form

$$z_t = \sum_{n=1}^{\infty} c_{tn} z_i^n, \tag{149}$$

valid for sufficiently small values of $z_i$. The series for $M_1$ is obtained after substituting Eq. (149) inside Eq. (18). Every perturbation quantity $\delta\phi$ is a given function of $\gamma_a$, $\gamma_b$, $R_0$, $z_i$, and $z_t$: $\delta\phi(\gamma_a,\gamma_b,R_0,z_i,z_t)$. Therefore, we substitute Eq. (149) inside $z_t$ in any quantity composing the analytic expression for $u_i$ and expand in powers of $z_i$. Let us give some insights about the sequence we have followed. We rewrite Eq. (115) for the case of a reflected rarefaction:

$$u_i = \frac{\delta v_i^{\infty}}{k\psi_0 D_i} = \frac{\tilde{v}^0_{yb} - R\tilde{v}^0_{ya}}{R+1} + \frac{RF_a}{R+1}. \tag{150}$$

We expand each quantity inside the first term of Eq. (150) in powers of $z_i$. We write the definitions for the lateral velocity at both sides of the contact surface at $t = 0+$, in fluid $a$,

$$\tilde{v}^0_{ya} = \frac{\delta v^0_{ya}}{k\psi_0 D_i} = \frac{U}{D_i}\left(1 - \frac{D_t}{D_i}\right), \tag{151}$$

and in fluid $b$,

$$\tilde{v}^0_{yb} = \frac{\delta v^0_{yb}}{k\psi_0 D_i} = \frac{c_{b1}}{D_i}\left(a + b\,\zeta_{rt} + c\,\zeta_{rt}^2\right), \tag{152}$$

where the quantities $a$, $b$, and $c$ are defined in Eqs. (153):

$$a = \frac{\zeta_{rh}^2}{\gamma_b + 1}\frac{\tilde{\psi}_{rt}^0 - \tilde{\psi}_{rh}^0}{\zeta_{rh} - \zeta_{rt}} - \frac{2\zeta_{rh}}{\gamma_b + 1}\left[\frac{(\tilde{\psi}_{rt}^0 - \tilde{\psi}_{rh}^0)\zeta_{rt}}{\zeta_{rh} - \zeta_{rt}} + \tilde{\psi}_{rt}^0\right], \tag{153a}$$

$$b = \frac{2}{\gamma_b + 1}\left[\frac{(\tilde{\psi}_{rt}^0 - \tilde{\psi}_{rh}^0)\zeta_{rt}}{\zeta_{rh} - \zeta_{rt}} + \tilde{\psi}_{rt}^0\right], \tag{153b}$$

$$c = -\frac{1}{\gamma_b + 1}\frac{\tilde{\psi}_{rt}^0 - \tilde{\psi}_{rh}^0}{\zeta_{rh} - \zeta_{rt}}. \tag{153c}$$

The velocities $D_i$, $D_t$, $U$, and $c_{b1}$ can be found, respectively, in Eqs. (1), (11), (14), and (5) of Secs. I and II. $\tilde{\psi}_{rh}^0$, $\tilde{\psi}_{rt}^0$, $\zeta_{rh}$, and $\zeta_{rt}$ can be found in Eqs. (51) and (9) of Sec. III A. To expand $R$, we realize that

$$R = R_0\frac{\rho_{af}}{\rho_{a0}}\frac{\rho_{b0}}{\rho_{b1}}\frac{\rho_{b1}}{\rho_{bf}}, \tag{154}$$

therefore we expand each factor $\rho_{b0}/\rho_{b1}$, etc., following the exact formulas shown in Eqs. (5), (10), and (13) of Sec. II.

When expanding the vorticity parameter $F_a$ in powers of $M_i - 1$, it is convenient to use Eq. (113):

$$F_a = -\Omega_a \sinh\chi_t \tilde{P}_t(s_a = -\sinh\chi_t). \tag{155}$$

According to Eq. (96), we have

$$\tilde{P}_t(s_a = -\sinh\chi_t) = \sum_{n=0}^{\infty}\frac{p_{t0}^{(2n+1)}}{(\sinh\chi_t)^{2n+2}}, \tag{156}$$

where $p_{t0}^{(2n+1)}$ is the $(2n+1)$th derivative of the pressure perturbation at the transmitted shock front at $t = 0+$. If we substitute Eq. (156) in Eq. (155), we obtain

$$F_a = -\Omega_a\sum_{n=0}^{\infty}\frac{p_{t0}^{(2n+1)}}{(\sinh\chi_t)^{2n+1}}. \tag{157}$$

There is a remarkable property for the initial derivatives: $p_{t0}^{(1)} \propto z_i + O(z_i^2)$, $p_{t0}^{(3)} \propto z_i^2 + O(z_i^3)$, etc. Besides, $\Omega_a \propto z_i^2 + O(z_i^3)$. It follows that $F_a \propto z_i^3 + O(z_i^4)$. This makes that the Taylor coefficients in the weak shock limit are exact as they are written. The expansions of the terms that compose the truncated expression for $F_a$ can be expanded in powers of $z_i$. The final result for $u_i$ can then be expanded in powers of $M_i - 1$ after using the relationship given by Eq. (1). The explicit and lengthly details of the intermediate calculations are inside the corresponding *Mathematica* file attached to the Supplemental Material [37].

If we want to develop the expansions in powers of the other small parameters ($\varepsilon = 1/M_i$, $\varepsilon = R_0^{tt} - R_0$, $\varepsilon = R_0 - R_0^{\text{crit}}$, and $\varepsilon = R_0 - R_0^{\text{min}}$), the only difference with the weak shock limit is that the bulk parameter $F_a$ is now taken from the expansion of the function $F_{a1}^{[0]}(-2\chi_t)$. More exact expansions of $F_a$ could be obtained by expanding higher iteration orders of the quantity $F_{a1}(-2\chi_t)$. We have preferred to work with the starting value $F_{a1}^{[0]}(-2\chi_t)$ because it is clearly simpler and it gives enough accuracy for the ranges explored. The comparison between the different expansions and the exact asymptotic velocity is presented in the next section.

## III. APPROXIMATE FORMULAS FOR THE ASYMPTOTIC VELOCITIES

### A. Irrotational approximation

The asymptotic normal velocity is given by the first of Eqs. (115) which we repeat here for convenience (the normalization with $D_i$ is reminded):

$$u_i = \frac{\delta v_i^\infty}{k\psi_0 D_i} = \frac{\tilde{v}_{yb}^0 - R\tilde{v}_{ya}^0}{R+1} + \frac{RF_a}{R+1}. \tag{158}$$

The main difficulty associated with the calculation of $u_i$ lies in the bulk vorticity parameter $F_a$. If we neglected the second term of the above equation, it would be equivalent to say that the vorticity generated by the transmitted shock is negligible. We call "*weak shock approximation*" to such an assumption, and indicate it by

$$u_i^{ws} = \frac{\tilde{v}_{yb}^0 - R\tilde{v}_{ya}^0}{R+1}. \tag{159}$$

We compare here the differences between Eqs. (158) and (159) in different domains of the space of the four preshock parameters. At the end of this section, we show another approximate formula for $u_i$ that considers the lowest possible approximation to $F_a$. The accuracy with which $u_i$ is calculated will be dictated by the number of iterations used in the calculation of $F_a$. In general, we ensure at least three significant digits for $u_i$, increasing when necessary the number of the iteration steps. In Fig. 7(a), we compare $u_i^{ws}$ with $u_i$ as a function of $M_i$ for the other parameters shown in the figure. In Fig. 7(a), two sets of $\gamma$ values are chosen: $\gamma_a = 1.45, \gamma_b = 1.1$ and $\gamma_a = 1.45, \gamma_b = 1.8$. In each case, three different values of the preshock density ratio are considered, as indicated in the figure. The relative difference $|(u_i^{ws} - u_i)/u_i|$ is plotted against the incident shock Mach number. The solid blue curve with the blue circle as a marker corresponds to the parameters used in the experiments of [12,13]. For low values of the shock strength ($M_i \lesssim 2$), the difference between the irrotational approximation and the complete formula stays below 20% for the cases shown, except for specific choices of $R_0$. In general, the difference between the weak shock approximation and the exact result increases when the incident shock becomes stronger. In Fig. 7(b), we explicitly compare the exact and approximate curves for two particular cases. In the orange curves, the weak shock approximation always overestimates the exact result in an amount given by the value of the vorticity parameter $F_a < 0$ in the whole range studied. However, the blue curve shows that $F_a$ changes sign at $M_i \cong 6.5$, contrary to our intuition. At larger Mach numbers, the weak shock formula underestimates the asymptotic velocity. The intersection of the solid and dashed blue curves in Fig. 7(b) corresponds with the zero of the solid green curve in Fig. 7(a).

In Fig. 8(a), we show the relative difference $|(u_i^{ws} - u_i)/u_i|$, as a function of the preshock density ratio $R_0$ for the same set of gases as before, for different choices of $M_i$. For very weak shocks ($M_i = 1.1$), the blue curves indicate that the relative difference stays in general below 1% in the whole range. Every curve starts at the right, at the value $R_0^{tt}$, because a shock will be reflected for $R_0 > R_0^{tt}$. The solid blue curve shows two interesting points: one at which $F_a = 0$ for $R_0 \lesssim 0.8$ and a

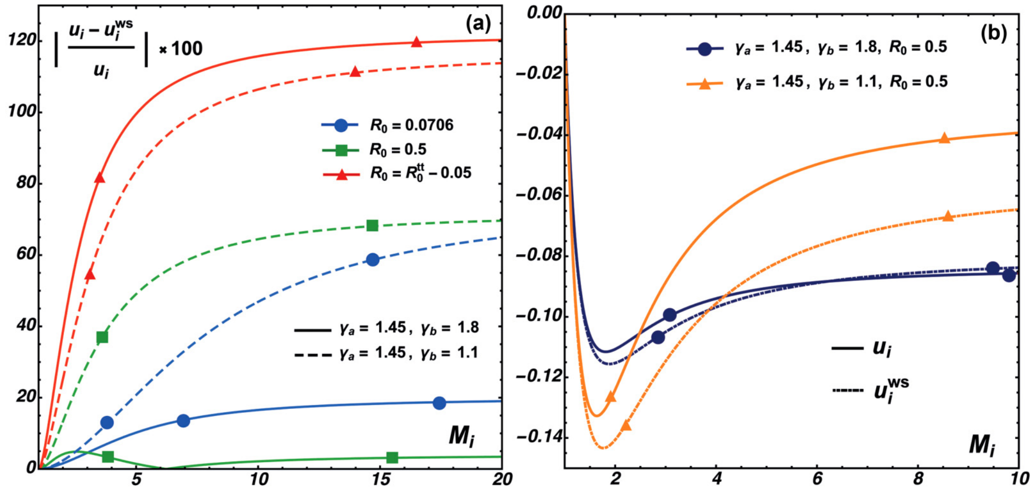


FIG. 7. (a) Relative difference between $u_i$ and $u_i^{ws}$ as a function of $M_1$ for different choices of the other parameters. (b) The quantities $u_i$ and $u_i^{ws}$ as a function of $M_i$ for different pairs of gases.

freeze-out point at $R_0 \lesssim 1$. For a stronger shock ($M_i = 5$), a similar behavior is observed with the difference that the characteristic values of $R_0$ at which $F_a = 0$ and $u_i = 0$ are shifted to the left. For even stronger shock ($M_i = 15$), the freeze-out point is observed at very low values of $R_0$ [14,27]. It is worth to note that compressibility of fluid $b$ is important for moderate to strong incident shocks, as can be seen in Fig. 8(a), where a relative difference between the weak shock formula and the exact result of around 50% is observed. In Fig. 8(b), we explicitly compare, as in Fig. 7(b), $u_i$ with $u_i^{ws}$ for the two sets of gases with $M_i = 5$. The point at which $F_a = 0$ is evidenced by the intersection of the solid and dashed blue curves. The freeze-out point is located at the point where the solid blue curve crosses the zero value.

In Fig. 9(a), a similar analysis is shown as a function of $\gamma_a$, the compressibility parameter of the gas compressed by the transmitted shock. For very weak shocks, the relative difference is negligible. For stronger shocks and values of $\gamma_a \to 1$, the relative difference increases significantly. Situations for which $F_a = 0$ are observed for low values of $\gamma_a$. In Fig. 9(b), the explicit comparison between $u_i$ and $u_i^{ws}$ is shown for the parameters shown. For the case indicated with the blue line we observe that for low values of $\gamma_a$, $F_a$ changes sign and $u_i^{ws}$ underestimates the normal velocity. Besides, it can become positive for highly compressible fluids.

In Fig. 10(a), the analysis is done as function of the compressibility parameter of the expanding fluid $b$. A similar behavior is observed as a function of $\gamma_a$. However, we notice that for relatively low values of $\gamma_b$, it is $F_a < 0$. For some ranges it is $u_i^{ws} > 0$, contrary to the correct value $u_i < 0$.

For very weak shocks, the difference is negligible, except for shocks of moderate to high strength. It is easy to see a characteristic value of $\gamma_b$ for which it is $F_a = 0$. In Fig. 10(b), we show $u_i$ and $u_i^{ws}$ as a function of $\gamma_b$. It is clear that $u_i^{ws}$ is not a good approximation for any value of $\gamma_b$ in the interval $1 \leqslant \gamma_b \leqslant 3$. This difference is also seen in the logarithmic plot of Fig. 10(a). At most, $u_i$ and $u_i^{ws}$ coincide at a single value of $\gamma_b$ for which it is $F_a = 0$.

The difference between $|u_i|$ and $|v_{ia}|$ tells us about the relative importance of the vorticity spread inside fluid $a$. Hence,

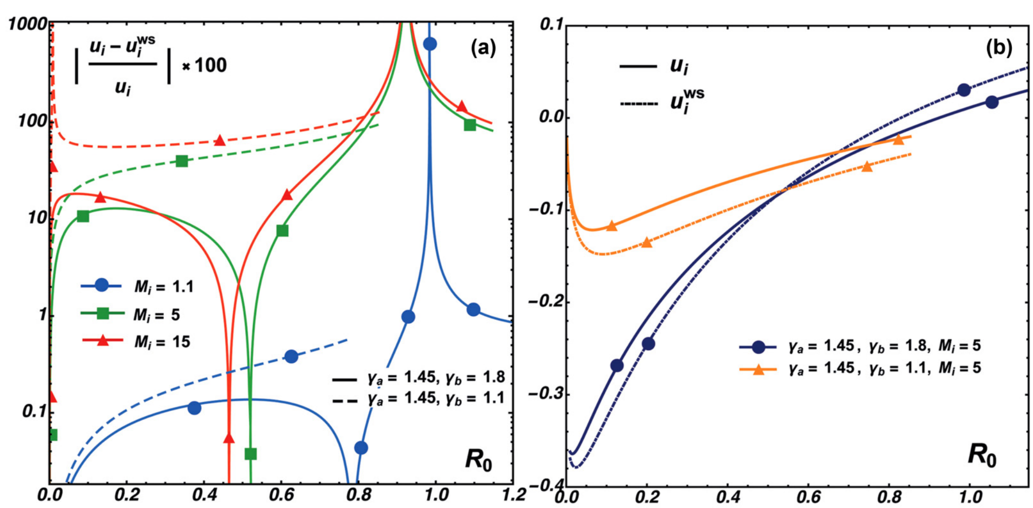


FIG. 8. (a) Relative difference between $u_i$ and $u_i^{ws}$ as a function of $R_0$ for different choices of the other parameters. (b) The quantities $u_i$ and $u_i^{ws}$ as a function of $R_0$ for different pairs of gases.

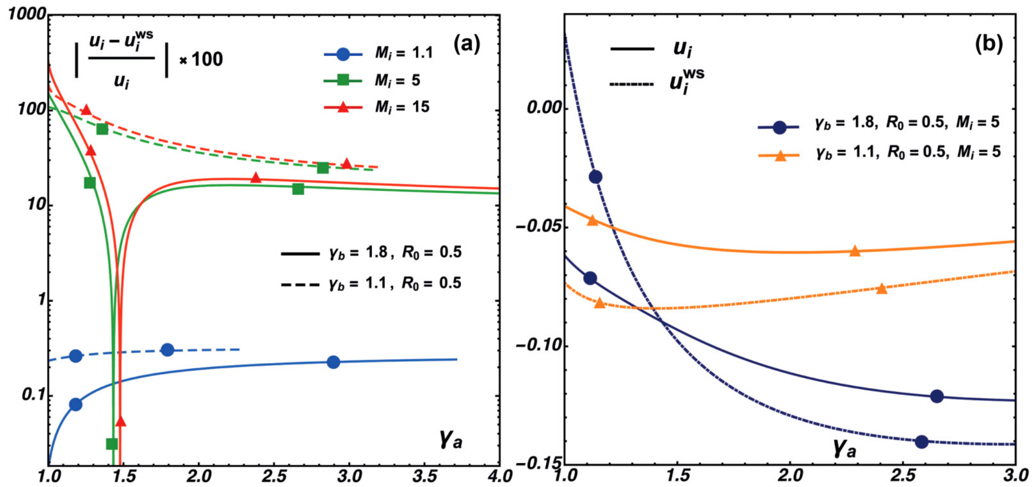


FIG. 9. (a) Relative difference between $u_i$ and $u_i^{ws}$ as a function of $\gamma_a$ for different choices of the other parameters. (b) The quantities $u_i$ and $u_i^{ws}$ as a function of $\gamma_a$ for different pairs of gases.

how much does the ratio $|u_i/v_{ia}|$ depart from unity, is informing us about the goodness of an irrotational approximation for that specific choice of preshock parameters. As discussed in the previous section, values of $|u_i/v_{ia}|$ very different from unity might warn us of a possible underestimation of the perturbation kinetic energy stored inside the bulk of the compressed fluid $a$. In Fig. 11, we show the ratio $|u_i/v_{ia}|$ as a function of the four preshock parameters. In Fig. 11(a), we show the velocities ratio as a function of the incident shock Mach number for the same pair of gases with different preshock density ratio. As expected, both velocities have the same absolute value for very weak shocks, as bulk vorticity is negligible. As the shock becomes stronger, the tangential velocity on the side of the compressed fluid increases and we can obtain values of $|u_i/v_{ia}|$ as low as 0.2 or lower, for $R_0 = 0.01$, or other combinations of the preshock quantities. In Fig. 11(b), we plot the same ratio as a function of the preshock density ratio. Now again, for very strong shocks we can get a vary large difference for very low values of $R_0$. There is a maximum value of the preshock density ratio ($R_0^{tt}$), above which a shock is reflected and the curve can not be continued with the results of this work. For $R_0 > R_0^{tt}$, the model of [15] has to be used. For curve (i) it is $R_0^{tt} \cong 0.884$, and for curve (ii) it is $R_0^{tt} \cong 0.899$. It is clear that the curves terminate to the right at the corresponding value of $R_0^{tt}$. To the left, the curves start at the minimum value $R_0^{\min}$ defined in Eq. (24). It is $R_0^{\min} \cong 0.0267$ for curve (i) and $R_0^{\min} \cong 0.00131$ for (ii). In Fig. 11(c), the velocity ratio is shown as a function of the isentropic exponent of fluid $a$. As $\gamma_a \to 1$, we see markedly different behaviors, depending on the values of $R_0$. In any case, $|u_i/v_{ia}|$ is always quite different from unity, except at singular points. For both cases, there is a maximum possible value of $\gamma_a$: $\gamma_a^{tt} = 3.624$ for curve (i) and $\gamma_a^{tt} \cong 221.53$ above which a shock will be reflected. In Fig. 11(d), we plot the velocity ratio as a function of $\gamma_b$. As happened in the shock reflected case [15], we recognize here two characteristic regimes. For the cases shown in Fig. 11(d), at lower values of $\gamma_b$ we see that $v_{ia}$ reaches a zero value, which is the reason of the peak to the left in curve (i), centered at

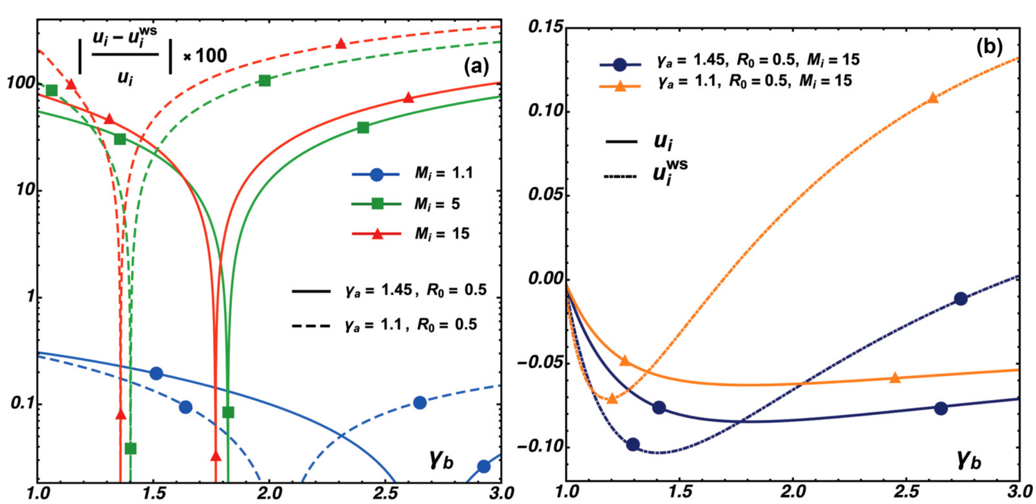


FIG. 10. (a) Relative difference between $u_i$ and $u_i^{ws}$ as a function of $\gamma_b$ for different choices of the other parameters. (b) The quantities $u_i$ and $u_i^{ws}$ as a function of $\gamma_b$ for different pairs of gases.

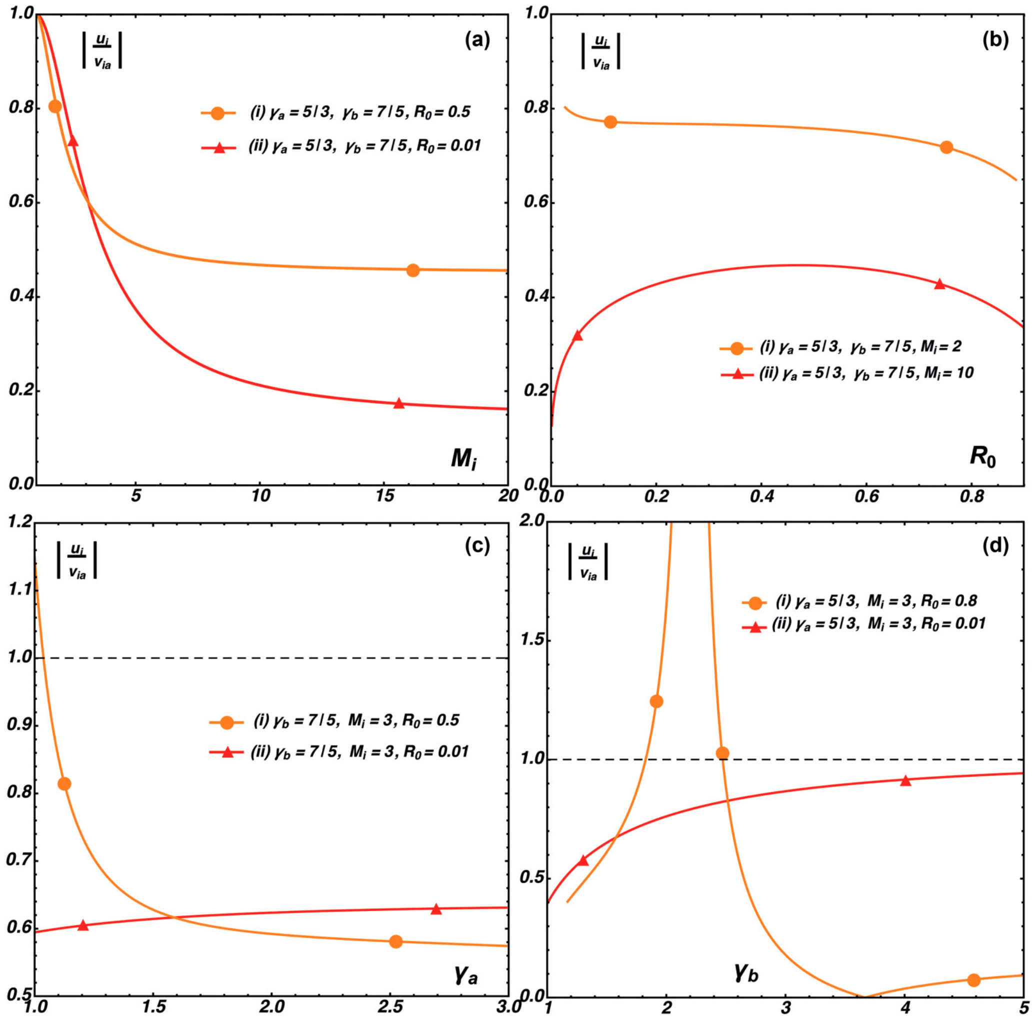


FIG. 11. Ratio $|u_i/v_{ia}|$ as a function of the different preshock parameters: (a) as a function of $M_i$, (b) as a function of $R_0$, (c) as a function of $\gamma_a$, and (d) as a function of $\gamma_b$.

$\gamma_b \cong 2.218$. We also see that there is normal velocity freeze-out also in curve (i) at $\gamma_b \cong 3.670$, where it is $u_i = 0$. We notice that for the curve that corresponds to $R_0 = 0.8$, we can not continue the to the left, for $\gamma_b < \gamma_b^{tt} = 1.171$, because a shock will be reflected. Curve (ii) has its boundary at $\gamma_b^{tt} < 1$, which is the reason why the curve starts from $\gamma_b = 1$. Both $\gamma_a^{tt}$ and $\gamma_b^{tt}$ can be obtained from Eq. (18) by imposing the condition $z_t = z_i$, which defines the total transmission situation.

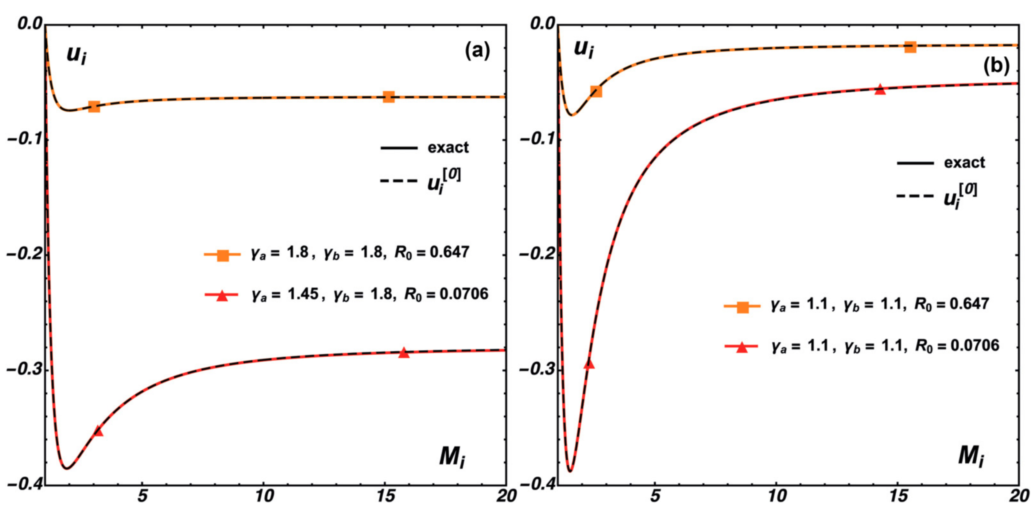


FIG. 12. (a) Comparison between Eqs. (158) and (160) for different pairs of gases. (b) Same as in (a) but with more compressible fluids.

### B. Approximate formula valid at any compression level

Given that the weak shock approximation formula may not give a sufficiently accurate result at high compression, it is worth to examine the possibility of using an analytic expression that takes into account the generation of vorticity inside the compressed fluid $a$. This is possible by considering the lowest order approximation to the parameter $F_a$, given by $F_a^{[0]}$ in Eq. (117). We formally get

$$u_i^{[0]} = \frac{\tilde{v}_{yb}^0 - R\tilde{v}_{ya}^0}{R+1} + \frac{RF_a^{[0]}}{R+1}. \tag{160}$$

In Figs. 12(a) and 12(b), we compare Eq. (160) with the exact value, for the preshock parameters shown in the legends. We see that the approximate Eq. (160) gives an excellent result in the whole range and does not show the shortcomings of the weak shock estimate.

## IV. APPROXIMATE ANALYTICAL FORMULAS OF THE ASYMPTOTIC VELOCITY IN DIFFERENT PHYSICAL LIMITS

### A. Taylor expansion in the weak shock limit ($M_i - 1 \ll 1$)

For very weak shocks, the weak shock formula discussed previously is a good estimate of the asymptotic velocity. However, as the shock Mach number increases, the vorticity generated by the rippled transmitted front becomes important and Eq. (159) ceases to be strictly valid. Similarly as has been done in [15], we can make a Taylor expansion in powers of $M_i - 1$ in the weak shock limit and compare it with the exact value. To this scope, we expand $u_i^{ws}$ and $RF_a/(F_a+1)$ and use the same strategy as in [15]. According to Eq. (113), the value of $F_a$ is proportional to the Laplace transform of $\tilde{P}_t$ evaluated at $s_a = -\sinh\chi_t$. We know that we can always write [15]

$$\tilde{P}_t(s_a) = \sum_{n=0}^{\infty} \frac{\tilde{p}_{t0}^{2n+1}}{s_a^{2n+2}}, \tag{161}$$

where $\tilde{p}_{t0}^{2n+1}$ is the $(2n+1)$th derivative of the pressure perturbation at the transmitted shock front at $t = 0+$. A series expansion like the above one will only be valid within its circle of convergence. The Taylor expansions of the first few derivatives can be retrieved in the Supplemental Material [37]. After collecting equal powers of $M_i - 1$ in Eq. (158) we arrive to an expansion of the form

$$\frac{\delta v_i^\infty}{k\psi_0 U} \cong \frac{R_0 - 1}{R_0 + 1} + \sum_{n=1}^{n_{\max}} a_n (M_i - 1)^n + O[(M_i - 1)^{n_{\max}+1}], \tag{162}$$

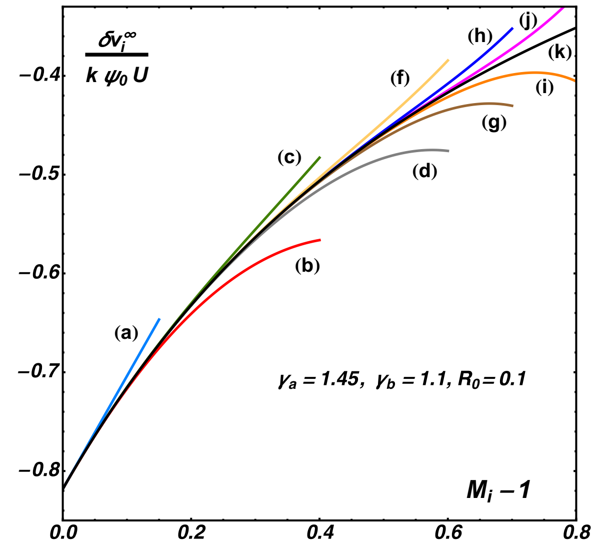


FIG. 13. Comparison between the exact normal velocity and different Taylor polynomials in powers of $M_i - 1$ for the gases and shock parameters indicated in the legend. Different curves correspond to different Taylor polynomials. For details, see the text.

where $n_{\max}$ is a given superior limit for the sum indicated above. In Fig. 11, we have calculated the Taylor polynomials up to $n_{\max} = 9$.

It is remarkable to see that the lowest order term is exactly the preshock Atwood number, confirming the validity of the impulsive prescription for very low values of the incident shock Mach number. An expansion like the above includes the contribution of the weak shock term $u_i^{ws}$ and the bulk parameter $RF_a/(R+1)$. For weak shocks, as it is $F_a \propto (M_i - 1)^3$ (see Fig. 2), bulk vorticity effects are included in Eq. (162) since the Taylor coefficient $a_2$ onwards. In Fig. 13, we compare the exact solution with the different Taylor polynomials of Eq. (162) up to $(M_i - 1)^9$ for a specific choice of the preshock parameters. We see that adding additional terms is not useful because the convergence radius of the corresponding series is quite small ($M_i - 1 \lesssim 0.5$). Unfortunately, the additional terms beyond the third order have very lengthy analytical expressions making their use impractical. We only show here the coefficients $a_1$ and $a_2$ as $a_2$ is the first Taylor coefficient to have information on the bulk vorticity profile near the contact surface. The other Taylor coefficients, from $a_3$ up to $a_9$, can be found in the *Mathematica* files inside Supplemental Material [37]. The first coefficients are

$$a_1 = \frac{4}{\gamma_a(\gamma_b+1)(1+R_0)^2(\gamma_b - \gamma_a R_0)} \left\{ \gamma_a\gamma_b + \gamma_a(\gamma_a - \gamma_b)R_0 + \gamma_a(5\gamma_a - 6\gamma_b)R_0^2 - \left[\gamma_a\gamma_b + \left(\gamma_a^2 + 3\gamma_a\gamma_b - 4\gamma_b^2\right)R_0 + \gamma_a(\gamma_a - 2\gamma_b)R_0^2\right]\sqrt{\frac{\gamma_a R_0}{\gamma_b}} \right\}, \tag{163}$$

$$a_2 = -\frac{4}{3\gamma_a(\gamma_b+1)^2(1+R_0)^3(\gamma_b - \gamma_a R_0)^3} \left[ Z_1(\gamma_a,\gamma_b,R_0) + Z_2(\gamma_a,\gamma_b,R_0)\sqrt{\frac{\gamma_a R_0}{\gamma_b}} \right], \tag{164}$$

where

$$\begin{aligned}
Z_1(\gamma_a,\gamma_b,R_0) &= 4\gamma_a\gamma_b^3(\gamma_b+1) - \gamma_a\gamma_b^2\big[\gamma_a(3\gamma_b+9)+\gamma_b^2-5\gamma_b\big]R_0 \\
&\quad - \big[\gamma_a^3(7\gamma_b+31)+\gamma_a^2\gamma_b(-3\gamma_b-81)+\gamma_a\gamma_b^2(-5\gamma_b+16)+33\gamma_b^3\big]2\gamma_b R_0^2 \\
&\quad + \big[\gamma_a^4(13\gamma_b+19)+\gamma_a^3\gamma_b(-61\gamma_b-283)+\gamma_a^2\gamma_b^2(51\gamma_b+549)+\gamma_a\gamma_b^3(21\gamma_b-297)+36\gamma_b^4\big]R_0^3 \\
&\quad + \big[\gamma_a^4(28\gamma_b+10)+\gamma_a^3\gamma_b(-52\gamma_b-115)+\gamma_a^2\gamma_b^2(21\gamma_b+138)+\gamma_a\gamma_b^3(3\gamma_b-36)+3\gamma_b^4\big]2R_0^4 \\
&\quad + \big[\gamma_a^2(43\gamma_b-95)+\gamma_a\gamma_b(-63\gamma_b+183)-108\gamma_b^2\big]\gamma_a^2R_0^5 - (\gamma_a+1)6\gamma_a^2\gamma_b^2R_0^6, \\
Z_2(\gamma_a,\gamma_b,R_0) &= -5\gamma_a\gamma_b^3(\gamma_b+1) + \big[\gamma_a^2(10\gamma_b+40)+\gamma_a\gamma_b(-13\gamma_b-109)+\gamma_b^2(6\gamma_b+72)\big]\gamma_b^2R_0 \\
&\quad + \big[\gamma_a^3(3\gamma_b+27)+\gamma_a^2\gamma_b(62\gamma_b+110)+\gamma_a\gamma_b^2(-77\gamma_b-365)+\gamma_b^3(6\gamma_b+222)\big]\gamma_b R_0^2 \\
&\quad + \big[\gamma_a^4(-8\gamma_b-14)+\gamma_a^3\gamma_b(-33\gamma_b+99)+\gamma_a^2\gamma_b^2(100\gamma_b-152)+\gamma_a\gamma_b^3(-81\gamma_b+99)-54\gamma_b^4\big]R_0^3 \\
&\quad + \big[\gamma_a^4(-16\gamma_b-4)+\gamma_a^3\gamma_b(-21\gamma_b+243)+\gamma_a^2\gamma_b^2(60\gamma_b-396)+\gamma_a\gamma_b^3(-12\gamma_b+180)-12\gamma_b^4\big]R_0^4 \\
&\quad - \big[\gamma_a^3(8\gamma_b-10)+\gamma_a^2\gamma_b(-15\gamma_b+21)+\gamma_a\gamma_b^2(-12\gamma_b-18)-12\gamma_b^3\big]\gamma_a R_0^5,
\end{aligned} \tag{165}$$

### B. Strong shock limit $M_i \gg 1$

For very strong incident shocks, the following expansion is possible, similarly as for the shock reflected situation [15]:

$$u_i \cong b_\infty + \frac{b_2}{M_i^2} + \frac{b_4}{M_i^4} + O\big(M_i^{-6}\big). \tag{166}$$

The analytical general expressions of the above coefficients can be retrieved in the corresponding *Mathematica* file attached in the Supplemental Material [37]. As happened with the shock reflected case [15], the analytical expressions are rather long to be written. To obtain $b_n$ we have used $F_a^{[0]}$, which makes a good job even for low values of $M_i$, as can be seen in Fig. 14, where the preshock parameters are indicated in the legend.

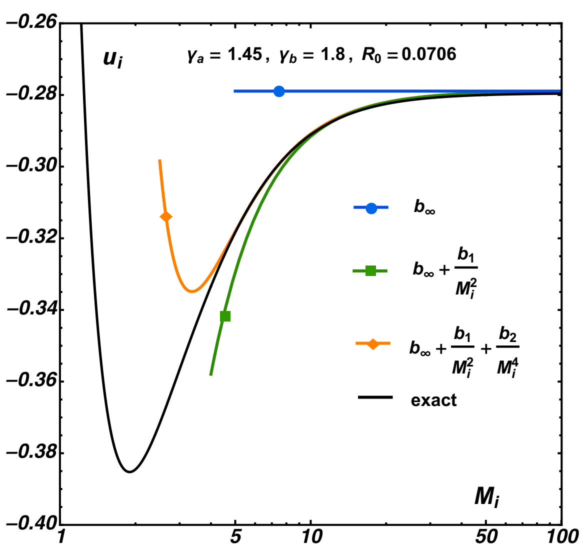


FIG. 14. Comparison between $u_i$ and different Taylor polynomials in $1/M_i^2$ for the preshock conditions indicated in the legend.

### C. Taylor expansion in powers of $(R_0^{tt} - R_0)$, valid for $R_0^{\min} \ll R_0 \leqslant R_0^{tt}$

Near the boundary of total transmission, the asymptotic velocity can be expanded in powers of $R_0^{tt} - R_0$. As done in the previous paragraph, the expansion is done on the analytical formula for $u_i^0$ and we obtain a formula of the type

$$\begin{aligned}
u_i &\cong c_0 + c_1\big(R_0^{tt}-R_0\big) + c_2\big(R_0^{tt}-R_0\big)^2 + c_3\big(R_0^{tt}-R_0\big)^3 \\
&\quad + c_4\big(R_0^{tt}-R_0\big)^4 + O\big[\big(R_0^{tt}-R_0\big)^5\big].
\end{aligned} \tag{167}$$

We can see in Fig. 15 that the fourth order polynomial agrees quite well with the exact formula over a wide interval of the parameter $R_0$. We notice that for this choice of preshock quantities, the asymptotic velocity is positive for $R_0 > 1$, indicating the possibility of freeze-out near $R_0 \cong 1.1433$. The coefficients $c_0, c_2, \ldots$ can be found in the corresponding *Mathematica* file attached in the Supplemental Material [37].

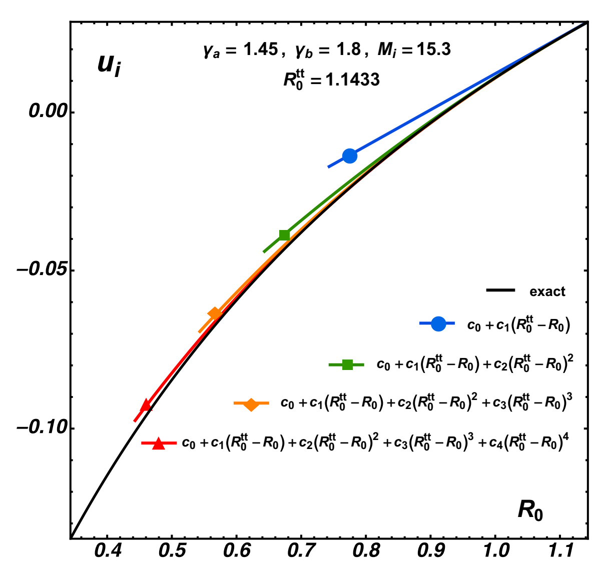


FIG. 15. Comparison between $u_i$ and different Taylor polynomials in $R_0^{tt} - R_0$ for the preshock conditions indicated in the legend.

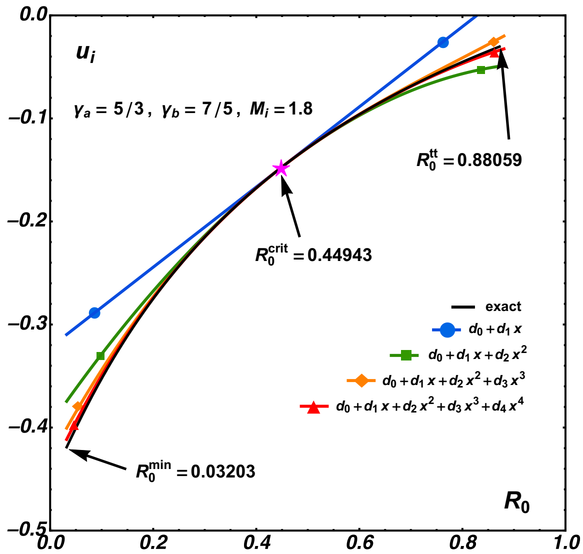


FIG. 16. Comparison of the Taylor polynomials centered at $R_0 = R_0^{\rm crit}$ with the exact value of $u_i$. For $R_0 > R_0^{\rm crit}$, the expansion parameter is $x = R_0/R_0^{\rm crit} - 1$. For $R_0 < R_0^{\rm crit}$, the expansion parameter is $x = 1 - R_0/R_0^{\rm crit}$. For details of the expansion, see the text.

It is noted that the expansion discussed in Eq. (167) is not limited to the weak shock limit, as there is no restriction on the incident shock Mach number, analogously as has been shown for the similar expansion in [15].

### D. Taylor expansion in powers of $(R_0 - R_0^{\rm crit})$

At the value $R_0 = R_0^{\rm crit}$, given by Eq. (25), the rarefaction tail remains steady in the laboratory frame of reference. Mikaelian studied a similar configuration for the case of a shock reflected, in which the reflected shock was at rest. A similar situation is possible here, and having at our disposal the model equations, it is worth to expand $u_i$ in a neighborhood of $R_0^{\rm crit}$:

$$u_i \cong d_0 + d_1\left(R_0^{tt} - R_0\right) + d_2\left(R_0^{tt} - R_0\right)^2 + d_3\left(R_0^{tt} - R_0\right)^3 + d_4\left(R_0^{tt} - R_0\right)^4 + O\left[\left(R_0^{tt} - R_0\right)^5\right]. \tag{168}$$

The comparison is shown in Fig. 16 for the preshock parameters indicated in the legend. This expansion shows the largest circle of convergence when compared to the other Taylor expansions obtained in this work.

### E. Normal velocity in the limit $R_0 \to 0$

#### 1. $R_0 \to 0$, $z_i \equiv \infty$

When we approach the limit of very low density gases to the left of the contact surface, we arrive to the limits shown in Eqs. (20) and (22) and we must be careful inside which interval we want to perform the Taylor expansion. For exactly $R_0 = 0$, the only possible incident shock strength is $z_i = \infty$ or, equivalently, $M_i = \infty$. For small but finite values of $R_0$ we must distinguish whether we make $z_i \gg 1$ or work with a large enough but finite value of the shock strength. This fact enables us to establish the boundary $R_0 = R_0(z_i)$, which is a function of the incident shock Mach number. For not necessarily negligibly small values of the preshock density ratio, the rarefaction tail starts to move to the left, following the transmitted shock. As $R_0$ decreases still further, the velocity of the rarefaction tail is nearer to the velocity of the material boundary. In those conditions, it is clear that the pressure, density, and sound speed at the contact surface become also infinitely small. In the strict limit of $R_0 = 0$, both surfaces coincide and we are not working any longer with an RM environment in two fluids, as there is only the expanding fluid against vacuum. In this case, it is known that the normal ripple velocity is exactly zero [6]. In the limit $R_0$ very near zero, the bulk vorticity term rapidly tends to zero, but the weak shock term $u_{ws}$ tends to $\delta v_{yb}^0 \neq 0$, even in the expansion against vacuum situation, as discussed in [28]. We must admit that our model does not give a continuous limit for $u_i$ in the limit $R_0 = 0$. This discontinuous behavior is related to the fact that this limit is singular. On one hand, the shock strength must be taken equal to $z_i \equiv \infty$, and on the other side, only one fluid is present. In fact, even for negligibly small and nonzero values of $R_0$, two fluids are present and the one-dimensional (1D) background velocities of the contact surface and of the rarefaction tail are different. Therefore, a region of uniform density and pressure will always be created between the contact surface and the rarefaction tail, where pressure perturbations exist and a velocity field is generated. Inside this strip of fluid, lateral mass flow exists up to the contact surface itself, giving rise to the velocity contribution $\delta v_{yb}^0$. Our two fluids model does not handle the limiting case $R_0 = 0$. Such a case must be studied with a traveling alone rarefaction wave in the strict limit $M_1 = 0$, using the results of Sec. III A, as discussed in [28]. Under such conditions, the normal velocity at the rarefaction tail can be seen to be exactly zero at all times since $t = 0+$.

#### 2. Taylor expansion in powers of $(R_0 - R_0^{\rm min})$, valid for $R_0^{\rm min} \leqslant R_0 \ll R_0^{tt}$

The preshock density ratio defined in Eq. (24) defines two regimes of the expansion. For $R_0 > R_0^{\rm min}$, we keep the incident shock strength at a finite value. In the same way as before, we can make a Taylor expansion of the normal perturbation velocity in powers of $(R_0 - R_0^{\rm min})$ of the form

$$u_i \cong e_0 + e_1\left(R_0 - R_0^{\rm min}\right) + e_2\left(R_0 - R_0^{\rm min}\right)^2 + e_3\left(R_0 - R_0^{\rm min}\right)^3 + e_4\left(R_0 - R_0^{\rm min}\right)^4 + O\left[\left(R_0 - R_0^{\rm min}\right)^5\right]. \tag{169}$$

We compare the above formula with the exact solution in Fig. 17. It is seen, as happens with the Taylor expansions studied in the other physical limits, that the convergence radius of the whole series is also finite, amounting for this case to $R_0 - R_0^{\rm min} \lesssim 0.0005$, where $R_0^{\rm min} = 0.001\,168$. The analytical results for the coefficients $e_n$ are rather lengthy to be written and are shown inside the *Mathematica* files attached in the Supplemental Material [37].

## V. COMPARISON WITH SIMULATIONS AND EXPERIMENTS

In this section we compare experiments and simulations with our linear theory. In particular, we follow the linear time

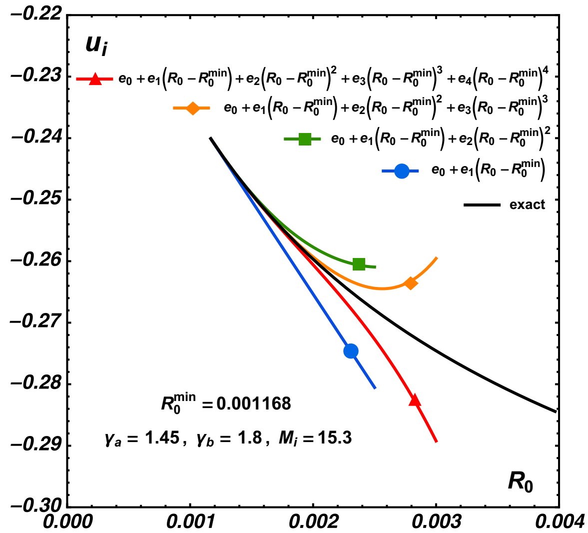


FIG. 17. Comparison of the Taylor polynomials centered at $R_0 = R_0^{\mathrm{min}}$ with the exact value of $u_i$ for the parameters indicated in the legend.

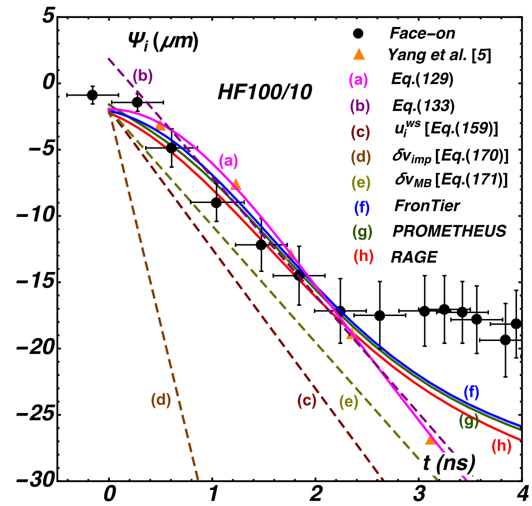


FIG. 18. Comparison between the temporal evolution of the interface ripple and its velocity for HF100/10 case of [13] and our theoretical model. Curves are indicated inside the figure and explained in the text.

evolution of the contact surface ripple and how it depends on the preshock parameters (initial ripple amplitude and perturbation wavelength and fluids parameters). Besides, it is worth to compare the growth rate of the experiments and simulations, with the different analytic approximations, where adequate, as obtained in the previous sections.

### A. Experiments of Refs. [12,13]

In the experiments described in [12,13], strong shocks have generated to drive the RMI for the rarefaction reflected situation. The target is formed with a beryllium (Be) ablator and a tamper formed by a low density foam or plastic. Two-dimensional (2D) corrugation is imposed at the contact surface an its evolution is diagnosed with face-on and side-on radiography. The 1D background flow had been studied with LASNEX simulations and the details are shown in [12]. Two incident shock strengths had been used: $M_i = 15.3$ (which is called high drive) and $M_i = 10.8$ (called low drive). The isentropic exponents used are $\gamma_b = 1.8$ for the beryllium ablator, $\gamma_a = 1.45$ for the foam tamper, and $\gamma_a = 1.8$ for the plastic tamper. An initial density jump $R_0 = 0.0706$ is considered for the Be-foam target and $R_0 = 0.647$ for Be-plastic. A wide range of initial amplitude and wavelength ratios have been studied in [12] ($0.04 \leqslant \psi_0/\lambda \leqslant 0.28$). In order to distinguish the different experiments, we respect the identification scheme used in [12]: the first letter means the driving type (L for low pressure and H for high pressure), the second letter identifies the tamper material (F foam and P for plastic), the first written number is the perturbation wavelength and the second number is the preshock ripple amplitude (both in microns). For example, LF100/4 represents low drive, foam tamper, a wavelength equal to 100 $\mu$m and an initial interface corrugation amplitude equal to 4 $\mu$m. However, in the simulations reported in [13], more cases with other driving pressures have been also studied. For those cases, we simply indicate the incident shock Mach number in front of the tamper material letter.

#### 1. Numerical simulations

Simulations based on different codes are compared with experimental data in the two works cited before. In [12], they simulated face-on and side-on radiographs with CALE, a hydrodynamic Langragian-Eulerian code. In [13], they evaluate three different codes: FRONTIER is a front tracking code, PROMETHEUSwhich solves Euler's equations on a uniform rectangular grid, and RAGE (Radiation Adaptive Grid Eulerian) which is a multidimensional Eulerian radiation-hydrodynamics code. All of them had been validated against a variety of both analytic test problems and experiments. For details and extended bibliography, see [12,13].

#### 2. Detailed comparison for a single case: HF100/10

In this section we make an analysis of the experiment HF100/10, for which the experimental data and simulation results have been taken from [13]. We show the temporal evolution of the contact surface ripple in Fig. 18. The incident shock comes from the beryllium ablator and a shock is transmitted inside the foam tamper. The preshock parameters are $M_i = 15.3$, $\gamma_a = 1.8$, $\gamma_b = 1.45$, and $R_0 = 0.0706$. The preshock initial surface corrugation is 10 $\mu$m and the perturbation wavelength is 100 $\mu$m. In Fig. 18, we show the temporal evolution only up to $t = 4$ ns. Besides, we do only show the face-on data (black circles) because the side-on measurements cannot resolve small amplitudes (see [12]), which are relevant for the comparison within the temporal window in which linear growth is important. The origin of time coincides with the instant when the incident shock has completely disappeared, as discussed in [13], which is uncertain by $\cong 0.25$ ns. Using Eq. (129) is a good test for our linear theory results because it depends explicitly on the value of $\delta v_i^{\infty}$, which is given by Eq. (115). Choosing a wrong value would result in disagreement between curve (a) and the experiments, which is not the case here. Besides, as is evident from Fig. 18, for these experimental conditions we can not discern between $u_i^{[5]}$ and $u_i^{[0]}$, and the curves predicted using both values are

TABLE I. Growth rate comparison of the cases discussed [12,13]. The experimental and simulation data for HF cases are taken from Fig. 7 of [13] and for LF and plastic tamper (P) cases from Fig. 26 of [12]. The last three columns are linear asymptotic velocity predictions: the first of them are calculated using five iterations in the functional equation [Eq. (79)], the second is the approximate formula without iteration [Eq. (160)], and the third are Taylor's series estimations. The key is (ws) weak shock limit [Eq. (162)], (ss) strong shock limit [Eq. (166)], and (hdj) high initial density jump [Eq. (167)]. The first two columns are the values of initial post-shock amplitude Eq. (128) and asymptotic ordinate Eq. (134) for the contact surface ripple. Lengths are given in $\mu$m and velocities in $\mu\mathrm{m\,ns}^{-1}$.

| Case | $\psi_0/\lambda$ | $\psi_0^*$ | $\psi_\infty$ | $\delta v_i^\infty$ (Expt.) | $\delta v_i^\infty$ (Simul.) | $\delta v_i^{\infty[5]}$ | $\delta v_i^{\infty[0]}$ | $\delta v_i^\infty$ (Limits) |
|---|---|---|---|---|---|---|---|---|
| HF 100/4 | 0.04 | −0.775 | 0.731 | −3.135 | −3.568 | −3.562 | −3.557 | −3.557 (ss) |
| HF 150/10 | 0.067 | −1.938 | 1.828 | −7.411 | −6.033 | −5.936 | −5.929 | −5.928 (ss) |
| HF 100/10 | 0.1 | −1.938 | 1.828 | −9.174 | −8.356 | −8.904 | −8.893 | −8.892 (ss) |
| HF 100/14 | 0.14 | −2.713 | 2.559 | −10.721 | −10.742 | −12.466 | −12.450 | −12.449 (ss) |
| HF 50/7 | 0.14 | −1.357 | 1.279 | −13.012 | −10.742 | −12.466 | −12.450 | −12.449 (ss) |
| HF 60/10 | 0.167 | −1.938 | 1.828 | −9.009 | −11.670 | −14.841 | −14.822 | −14.821 (ss) |
| HF 30/7 | 0.233 | −1.357 | 1.279 | −10.153 | −13.308 | −20.777 | −20.750 | −20.749 (ss) |
| HF 38/10 | 0.263 | −1.936 | 1.828 | −11.906 | −13.793 | −23.433 | −23.403 | −23.401 (ss) |
| HF 50/14 | 0.28 | −2.713 | 2.559 | −14.630 | −14.546 | −24.932 | −24.900 | −24.899 (ss) |
| LF 100/4 | 0.04 | −0.746 | 0.754 | −2 | −2.5 | −2.557 | −2.554 | −2.554 (ss) |
| LF 150/10 | 0.067 | −1.865 | 1.884 | −3.5 | −4.5 | −4.261 | −4.257 | −4.257 (ss) |
| LF 100/10 | 0.1 | −1.865 | 1.884 | −5 | −5.5 | −6.391 | −6.386 | −6.386 (ss) |
| LF 100/14 | 0.14 | −2.611 | 2.638 | −5 | −7 | −8.948 | −8.940 | −8.941 (ss) |
| LF 50/7 | 0.14 | −1.306 | 1.319 | −6 | −6 | −8.948 | −8.940 | −8.941 (ss) |
| LF 30/7 | 0.233 | −1.306 | 1.319 | −8 | −7 | −14.913 | −14.900 | −14.901 (ss) |
| LF 50/14 | 0.28 | −2.611 | 2.638 | −10.5 | −9 | −17.896 | −17.880 | −17.881 (ss) |
| 1.33F 100/4 | 0.04 | 1.995 | 3.190 | | | −0.347 | −0.347 | −0.382 (ws) |
| 5.6F 100/4 | 0.04 | −0.597 | 0.929 | | | −1.429 | −1.428 | −1.429 (ss) |
| HF 100/25 | 0.25 | −4.845 | 4.569 | | | −22.261 | −22.232 | −22.231 (ss) |
| HF 100/50 | 0.5 | –9,691 | 9.138 | | | −44.522 | −44.465 | −44.462 (ss) |
| HP 100/14 | 0.14 | 2.979 | 4.459 | −2 | −3.5 | −2.750 | −2.749 | −2.749 (ss) |
| | | | | | | | | −2.743 (hdj) |
| LP 100/14 | 0.14 | 3.026 | 4.506 | −0.8 | −2.42 | −1.954 | −1.953 | −1.953 (ss) |
| | | | | | | | | −1.951 (hdj) |

therefore indistinguishable. In Table I, we give $\delta v_i^\infty$ using $u_i^{[5]}$ and $u_i^{[0]}$, as well as a comparison with different physical limits, where appropriate. The post-shock amplitude [Eq. (128)] is $\psi_0^* = -1.94$ $\mu$m indicating that during the shock refraction, the interface changes its phase. This is due to the difference between the shocked contact surface velocity and the incident shock speed ($U = 59.4$ $\mu$m/ns $> D_i = 49.8$ $\mu$m/ns), known as direct phase inversion [5]. The dotted line (b) is the

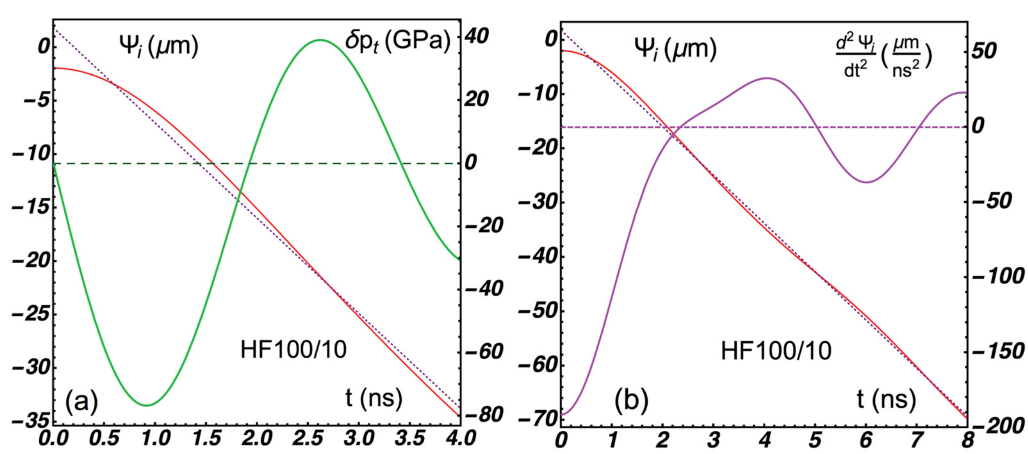


FIG. 19. (a) Time evolution of the contact surface ripple and the transmitted shock pressure perturbations for the experiment HF100/10. (b) Time evolution of the contact surface ripple and the contact surface acceleration for the experiment HF100/10.

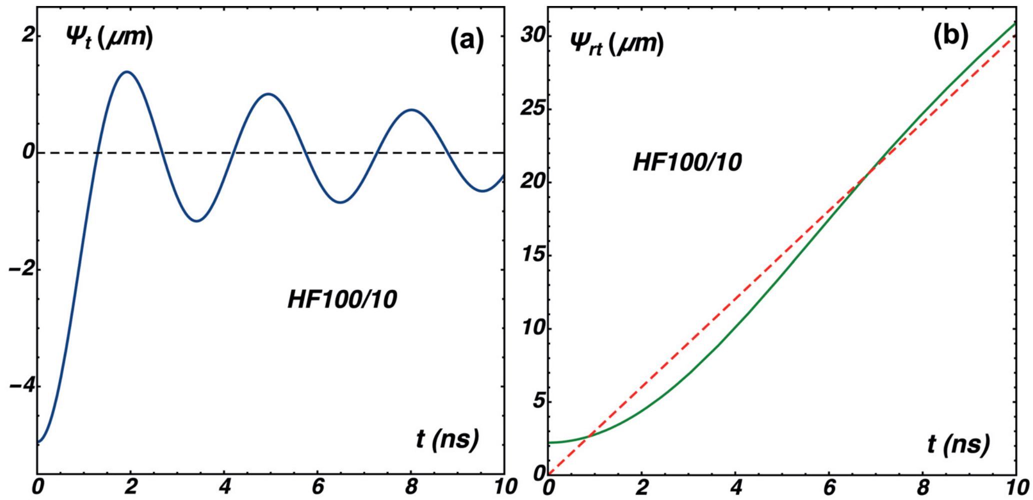


FIG. 20. (a) Time evolution of the transmitted shock ripple for the experiment HF100/10. (b) Time evolution of the rarefaction tail ripple for the experiment HF100/10.

asymptotic evolution predicted by Eq. (133). It intersects the vertical axis at a value equal to $\psi_\infty = 1.83\ \mu$m, which can be calculated with Eq. (134). We notice that $\psi_\infty$ is quite different from the post-shock corrugation $\psi_0^*$. The orange triangles have been numerically calculated using the linear simulations of Ref. [5]. We also show the prediction of some formulations of the impulsive model: dotted line (c) is calculated using the Richtmyer's prescription [1], dotted line (d) is calculated with the value $u_{ws}$ given by Eq. (159), and dotted line (e) is obtained with the impulsive Meyer-Blewett formula [4]. The 2D simulations are given by the solid curves: (f) FRONTIER, (g) PROMETHEUS, and (h) RAGE. The impulsive formula used to draw curve (c) is given by the original Richtmyer's prescription [1]

$$\delta v_{imp} = k\psi_0 U \frac{R_0 - 1}{R_0 + 1}, \tag{170}$$

and the Meyer-Blewett formula used to draw curve (e) is given by [4]

$$\delta v_{\mathrm{MB}} = \frac{k}{2}(\psi_0 + \psi_0^*)U\frac{R-1}{R+1}. \tag{171}$$

Several features concerning Fig. 18 merit discussion. First, as observed before, the approximate formula proposed in this work, with no iteration [Eq. (160)], shows very good agreement with the exact solution (115) [11]. Both expressions exactly agree with the calculations of [5], as shown in [11]. The adequacy of the compressible linear theory developed here to describe the experimental data and the simulations, before nonlinearities appear, is very good for this case. In fact, there is a reasonable description of the initial transient phase and the later linear asymptotic growth for $0 < t \leqslant 2.5$ ns. However, some weak shock approximate formulas give inaccurate results and scalings. Since impulsive prescriptions ignore the perturbation dynamics of the shock fronts for $t > 0^+$, they cannot take into account the compression effects and the bulk vorticity generation. Consequently, in the situations where the shock is not weak, they provide imprecise values for the growth rate [5,6,11]. However, the empirical Meyer and Blewett formula [4], proposed to fit their numerical data, gives a reasonable velocity estimation for this case. For these high values of the incident shock Mach number, compressibility effects are manifested not only in the growth rate value, but also in the asymptotic ordinate $\psi_\infty$ and the tangential velocities $\delta v_{ya}^\infty$ and $\delta v_{yb}^\infty$, which are different. In fact, as discussed in [4], they had to admit the existence of an asymptotic ordinate, quite different from $\psi_0^*$, of which they were unable to give a scaling law, derived either analytically or numerically. In Fig. 18, we see that the linear asymptotic formula [Eq. (129)] is valid inside the interval $0.8 \leqslant t \leqslant 2.5$ ns. The temporal window of linear saturation would be a function of the values of $\psi_0$ and $\lambda$, probably through the ratio $\psi_0/\lambda$. In Fig. 19(a), we show the temporal evolution of $\psi_i$ and $\delta p_t$. We see that the interface ripple enters its asymptotic stage much earlier than the transmitted shock pressure perturbations. By the time $t \cong 2$ ns, the interface ripple is growing with approximately constant velocity and the shock has just generated its first peak of vorticity inside fluid $a$. In Fig. 19(b), a similar comparison is done with the interface acceleration. Finally, in Fig. 20, we show the temporal evolution of the rippled transmitted

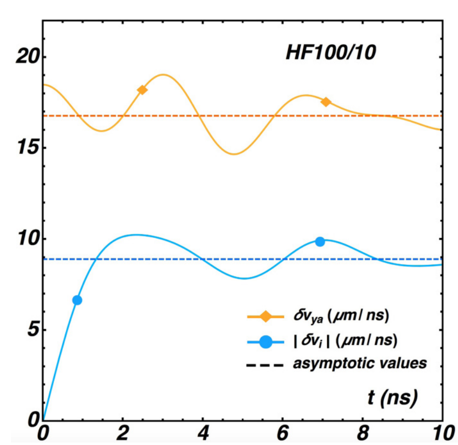


FIG. 21. Time evolution of the normal and tangential velocities (lighter fluid) at the contact surface for the experiment HF100/10.

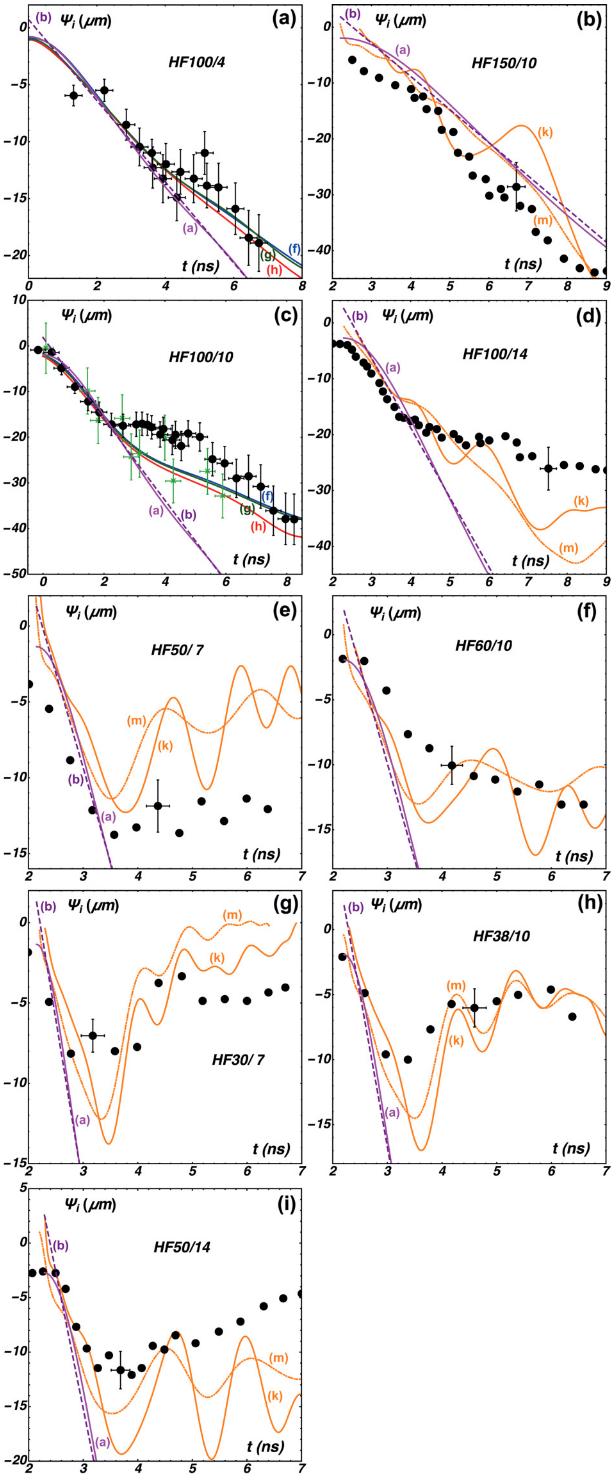


FIG. 22. Temporal evolution of the contact surface ripple for HF cases of [12]. Experimental data: black points are measured from face-on radiographs. Simulations: (f) FRONTIER, (g) PROMETHEUS, (h) RAGE, (k) face-on CALE, and (m) side-on CALE. Linear theory: (a) temporal evolution using $u_i^{[0]}$ [Eqs. (129) with (160)] and (b) asymptotic evolution predicted by Eq. (133).

shock and rarefaction tail corrugation. The rarefaction tail corrugation has been calculated with Eq. (58) of Ref. [20]. The shock corrugation amplitude is obtained using the calculations shown in the Appendix. There is a distinguishing characteristic

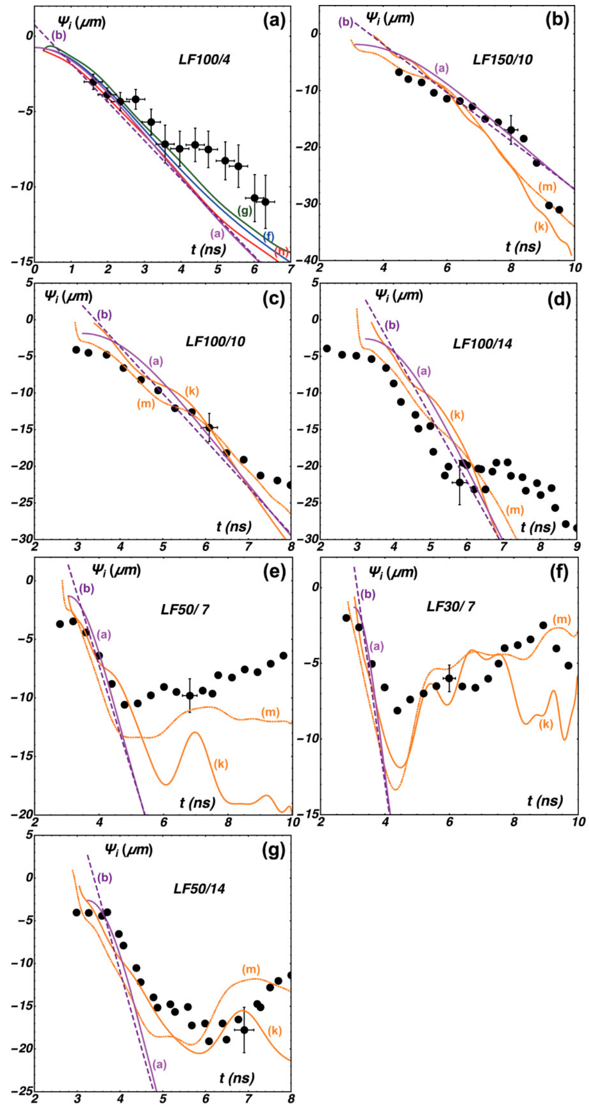


FIG. 23. Temporal evolution of the contact surface ripple for LF cases of [12]. Experimental data: black points are measured from face-on radiographs. Simulations: (f) FRONTIER, (g) PROMETHEUS, (h) RAGE, (k) face-on CALE, and (m) side-on CALE. Linear theory: (a) temporal evolution using $u_i^{[0]}$ [Eqs. (129) with (160)] and (b) asymptotic evolution predicted by Eq. (133).

when comparing the shock and interface ripple growths. The time taken by contact surface and rarefaction trailing edge corrugation amplitudes to reach their asymptotic is different from the characteristic time to reach the asymptotic for the transmitted shock ripple. This fact had also been qualitatively observed in [4], who had written the following: "The (helium) shock, in particular, was seen to undergo oscillations that are independent of the interface behavior." The characteristic time to reach the asymptotic for $\psi_{rt}$ is on the order of $\gtrsim$4 ns and $\psi_i$ is typically on the order of 1 ns. However, at the shock ripple, as discussed in [24], the asymptotic stage is usually reached after the third-fourth zero crossing, which for this case, amounts to a characteristic time between 4–5 ns. By the time the contact surface ripple reached its asymptotic, the transmitted shock has almost entirely generated the first peak of the vorticity

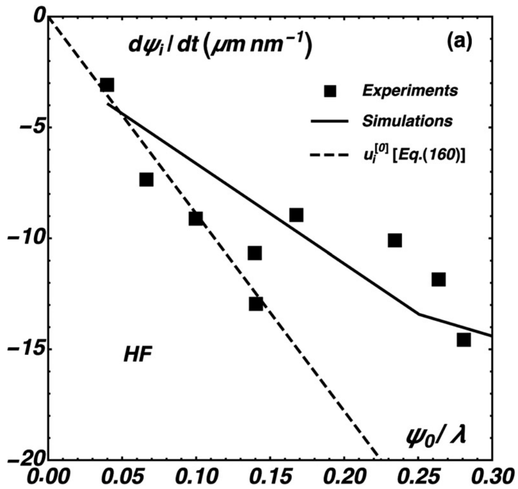


FIG. 24. Asymptotic normal velocity as a function of $\psi_0/\lambda$ for the previous experiments: (a) HF, (b) LF.

distribution in the bulk as shown in Fig. 19(a). This seems to be a general trend behind corrugated shock fronts [15].

As commented along the work, an important consequence of the high compression with corrugated shocks in RM environments is the generation of bulk vorticity which is manifested in different values for the normal and tangential velocities at the contact surface. In fact, in Fig. 21, we show the temporal evolution of both quantities within the temporal window of the experiment. The transverse final velocity $v_{ia}$ is quite different from $u_i$, a fact that *a priori* precludes the use of a potential flow model inside the compressed fluid. Up to date, there is no rigorous theory with which to study the weakly nonlinear phase that consistently joins the fully compressible linear growth phase and the following weakly nonlinear transition taking into account the vorticity spread in the compressed fluids.

### 3. *Rest of experiments and simulations of [12,13]*

In [12], the authors provided experimental data covering an extensive range of perturbation amplitudes and wavelengths ($0.04 \leqslant \psi_0/\lambda \leqslant 0.28$), for two different shock strengths. In Fig. 18, we compare those results with our [Eqs. (129) and (160)] for high drive, and the same is done in Fig. 19 for the low drive cases. Additionally, they presented a pair of configurations where the initial density ratio is changed with a plastic tamper (Fig. 20). In [13], the authors presented an exhaustive study of three experiments HF100/10, HF100/4, and LF100/4, adding to each experimental data the error bars together with 2D simulations. In Fig. 21, we compare with another four cases, only studied with simulations in [13]. As already commented before, in the curves drawn in [13], time is referenced to the instant when the incident shock has crossed the contact surface. The origin of time has an uncertainty around 0.25 ns. However, in the figures shown in [12], time is referenced to the moment when the experiments start. Therefore, knowing that the beryllium ablator has a depth of 100 $\mu$m, we estimate the instant when the shock has completely crossed the interface ripple as $t_{0+} = (100 + \psi_0)/D_i$. We obtain the range $2.09 \leqslant t_{0+} \leqslant 2.29$ ns for HF and $2.96 \leqslant t_{0+} \leqslant 3.24$ ns for LF cases. Let us concentrate in Fig. 18. As commented in [12], when the rarefaction wave

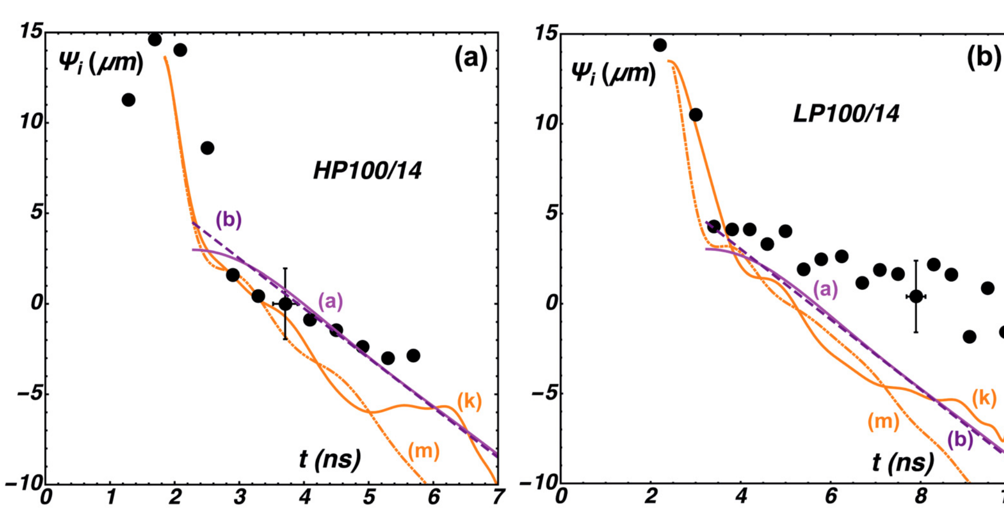


FIG. 25. Temporal evolution of HP (a) and LP (b) cases. The labeling used for the different curves follows the same indications as in Fig. 22.

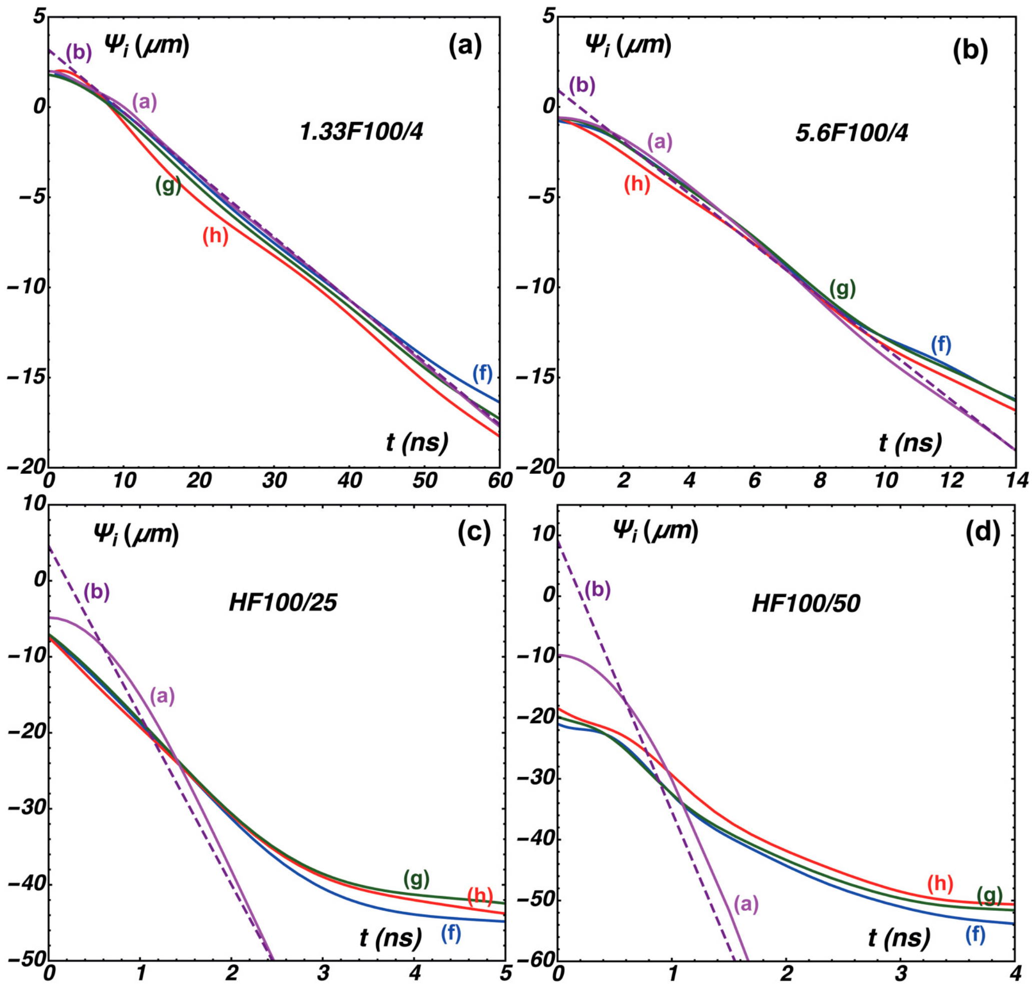


FIG. 26. Temporal evolution of the contact surface ripple for simulated cases of [13]. Simulations: (f) FRONTIER, (g) PROMETHEUS, and (h) RAGE. Linear theory: (a) temporal evolution using $u_i^{[0]}$ [Eqs. (129) with (160)] and (b) asymptotic evolution predicted by Eq. (133).

travels back to the ablation surface, a weak shock is generated inside the expanded fluid that hits the interface at $t \sim 4$ ns after the incident shock disappears. This means that for $t \gtrsim 4$ a second shock is transmitted inside the lighter fluid. It is clear that our theory is only valid before reshock occurs. In Fig. 19, the low drive cases are plotted as a function of time. Similar conclusions can be inferred as with the high drive case. The cases with a higher value of $\psi_0/\lambda$ show different initial slopes as compared to the experiments and simulations due to nonlinearity. In Table I we show, for each case, the ratio $\psi_0/\lambda$, the post-shock interface ripple amplitude $\psi_0^*$, the asymptotic ordinate $\psi_\infty$, the asymptotic normal velocity given in [12,13], the asymptotic velocity as given by the simulations shown in [12,13], the exact theoretical asymptotic velocity given by Eq. (158) [Eq. (160)], and the last column is the inferred value from the corresponding approximation (strong shock, weak shock, high density jump).

Different initial conditions (some of them with large values of the pre-shock ripple) are studied in Figs. 22 and 23. The dots are taken from the experimental results, the orange curves are different numerical simulation results and we have superposed to them our time evolution curves (complete and asymptotic). In Fig. 24, the dependence of the ripple normal velocity with the ratio $\psi_0/\lambda$ is shown. Dots are experimental results, the continuous curves are taken from simulations and the dotted lines are calculated with Eq. (160). In Fig. 25, the experimental ripple time evolution is compared with our results for experiments done with plastic targets and two shock strengths. In Fig. 26, a similar analysis is done for the cases studied in Ref. [13] only with simulations. In Fig. 27 we show several plots showing the dependence of the ratio between the normal velocity $u_i$ and the tangential velocity $v_{ia}$ as a function of the four pre-shock parameters: $M_i$, $R_o$, $\gamma_a$, and $\gamma_b$, as discussed in Fig. 11. We have used here the pre-shock conditions of the experiments of Ref. [13]. The markers refer to the experiments. We see that normal and tangential velocities are quite different, as the markers stay well below the horizontal line $u_i/v_{ia} = 1$.

It is interesting to compare the dependence of $u_i$, $v_{ia}$, and $v_{ib}$ as a function of the Mach number for the preshock parameters corresponding to the foam and plastic targets. This is shown in Fig. 28. The tangential velocity $v_{ib}$ agrees exactly with $u_i$, as expected. The more interesting behavior is shown by $v_{ia}$

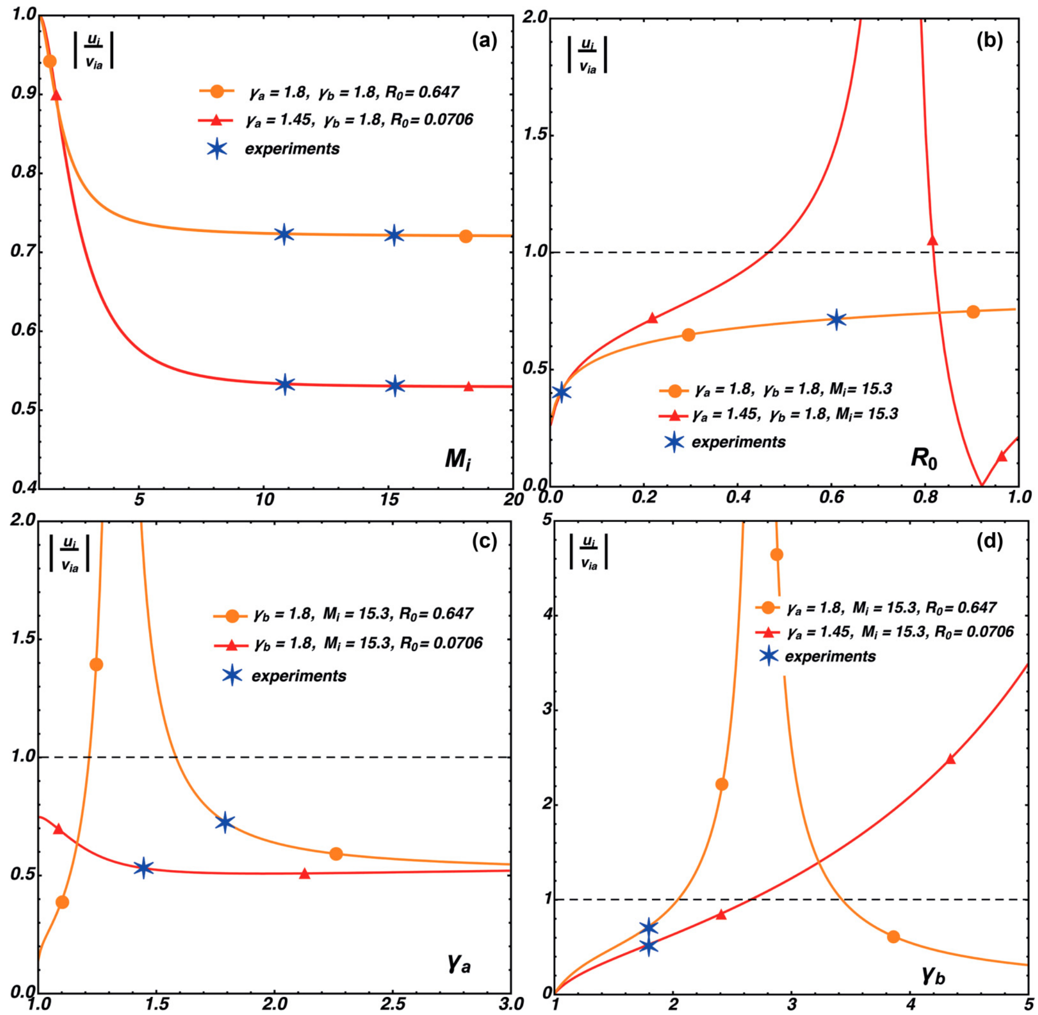

FIG. 27. Ratio of the normal velocity to the tangential velocity (in the lighter fluid) as a function of the four preshock parameters. In each plot, the experiments previously discussed are marked.

where we see that $v_{ia}$ and $v_{ib}$ start to deviate significantly at $M_i \gtrsim 1.4$, due to the vorticity in fluid $a$.

### B. Experiments of Ref. [22]

The authors of [22] have conducted a series of experiments in a shock tube at low Mach numbers in which the rarefaction

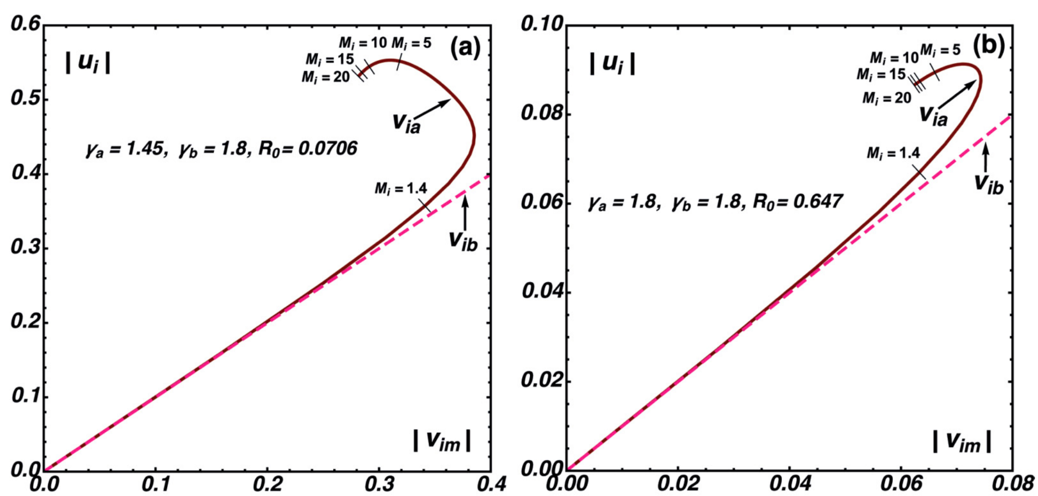

FIG. 28. Parametric curves showing the tangential and normal velocities in the HF (a) and LF (b) cases. The Mach number increases along each curve.

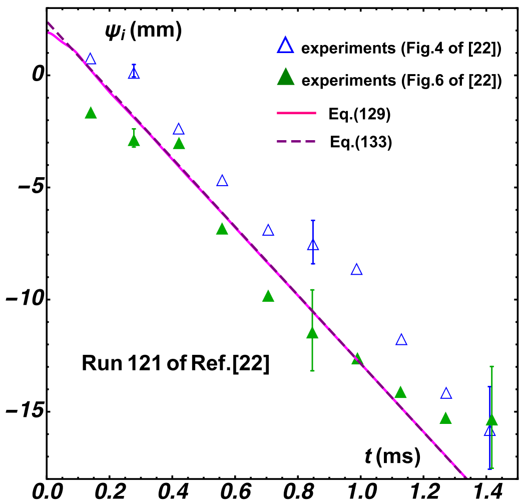


FIG. 29. Contact surface ripple amplitude as a function of time for the experiment 121 of [22]. Triangles refer to the experimental measurements. The continuous red curve is the result of Eq. (129) where $u_i^{[0]}$, given by Eq. (160), has been used. The dashed line is the asymptotic formula given by Eq. (133).

reflected configuration was studied. They have used a novel technique to accurately characterize the initial conditions at the shocked material surface. Perturbations are sinusoidal and laser sheet diagnostics were used to measure the interface displacement. Unfortunately, it is quite difficult to extract useful information for comparison from their experimental data. We have been able to compare with their results plotted in Figs. 4 and 5, for the case they called Run 121, in which a shock coming from air impinges a contact surface separating it from helium. The Mach number used for this case is $M_i = 1.15$. We plot the contact surface ripple as a function of time $\psi_i(t)$ using our Eqs. (129) and (133) in Fig. 29. The blue markers represent the measured temporal evolution of the fundamental mode (as seen from their Fig. 4) and the green markers represent the ripple amplitude as inferred from the positions of the bubble and spike. Our theoretical prediction goes in the middle of the experimental points. It is interesting to make a short analysis of the dynamics of the surface ripple, shock, and rarefaction tail, and tangential velocities in the interval of time during which linear theory is a reasonable assumption, in the same way we did in Figs. 18 to 27 in the previous subsection. In Fig. 30(a), we superpose the surface ripple complete and asymptotic evolution [Eqs. (129) and (133)] with the shock pressure perturbations calculated with Eq. (36) at $\chi_a = \chi_t$. We see that the surface ripple enters its asymptotic stage when the transmitted shock has almost passed its first peak, that is, at the time the transmitted shock has almost generated the first maximum of the vorticity distribution in the bulk. At that time, the interface acceleration is oscillating near zero [Fig. 30(b)]. A similar trend was observed in the experiments of [12,13] for a much stronger incident shock. In Fig. 31(a), we show the transmitted shock ripple amplitude given by the solution (40). We have superposed the approximate solution obtained by simply retaining up to $\pi_5$ and $\omega_5$ in the expression for $\tilde{p}_t$. In fact, for weak shocks, the coefficients $\pi_{2n+1}^m$ and $\omega_{2n+1}^m$ become negligible after $n \sim 2$. In Fig. 31(b), the rarefaction tail ripple growth is compared to the interface ripple. Behavior is similar as in the strong shock experiments.

In Fig. 31, we show the time evolution of the ripple at the rarefaction trailing edge. We compare the exact and asymptotic evolution. We see that during the interval of time in which linear theory is an acceptable approximation, the surface ripple enters its asymptotic stage much before than the rarefaction tail ripple, as in the experiments at large Mach.

In Fig. 32, we show the temporal evolution of the tangential velocity on fluid $a$ at the contact surface $v_a(x=0,t)$ and $v_b(x=0,t) = u(x=0.t)$. We see that both velocities start from quite different values and tend to an almost common asymptotic which is also very near the asymptotic value of the normal velocity. There is a very small difference between them due to the small amount of vorticity spread in the bulk of fluid $a$. We can notice the difference of this weak incident shock situation with Fig. 21 for the experiments of [12,13].

## VI. SUMMARY

We have presented an analytical study of the Richtmyer-Meshkov instability when a rarefaction is reflected. This work

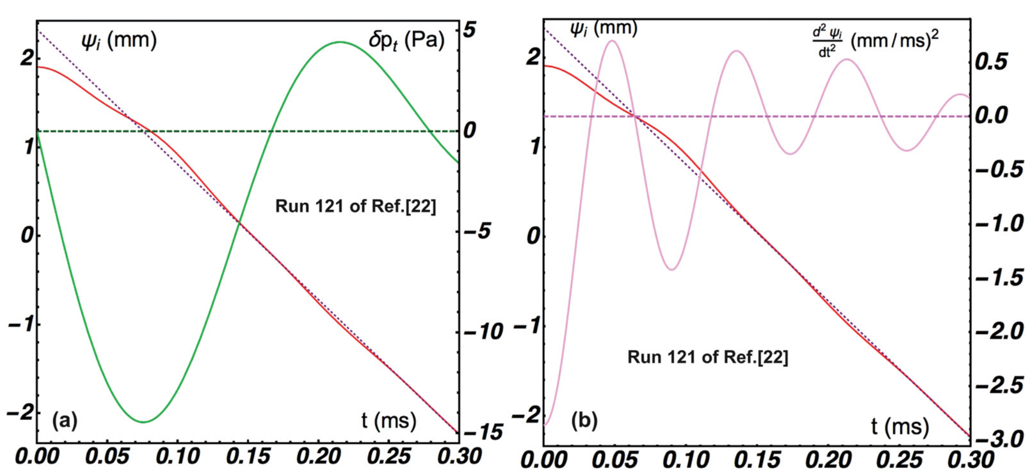


FIG. 30. (a) Contact surface ripple (exact and asymptotic) superposed to the transmitted shock pressure perturbations temporal evolution for the experiment 121 of [22]. (b) Contact surface ripple (exact and asymptotic) superposed to the contact surface ripple acceleration.

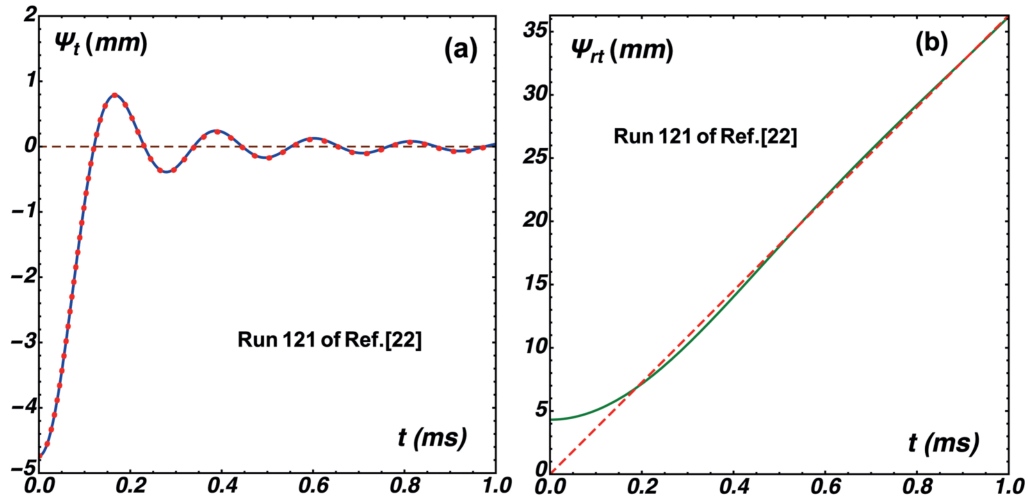


FIG. 31. (a) Transmitted shock ripple amplitude as a function of time. The continuous curve represents the exact solution of Eq. (40) and the dots represent the asymptotic solution. (b) Rarefaction tail ripple as a function of time: continuous curve is the exact solution and the dashed line is the asymptotic solution taken from [20].

is a natural continuation of previous works on the subject. The background profiles of pressure, density, and velocity have been obtained and the scaling laws in different regimes have been studied (weak and strong rarefactions, refraction near the boundary of total transmission). The equations of motion have been linearized and their solution has been briefly reviewed in order to be used later in the subsequent sections. The asymptotic velocity profiles inside each fluid have been solved taking into account the generation of vorticity inside the compressed fluid. The exact rotational solution is compared with the irrotational approximation and an important difference is observed in the values of the tangential velocity profiles. Besides, the rotational velocities change sign due to the spatial variations of the vorticity generated by the transmitted shock. The kinetic energy content of the perturbed fluids is analyzed by integrating the analytical profiles and we see that the asymptotic kinetic energy is concentrated in a narrow layer near the contact surface, essentially inside the first peak of the vorticity distribution in the bulk. This effect is stronger as the shock strength increases. A careful study of the dependence of the kinetic energy on the preshock parameters is obviously left for a future work. These scaling laws might result important to understand how energy is distributed in the bulk, becoming a useful tool in the design of theoretical models that aim to describe, for example, reshock. Besides, future nonlinear model may benefit from that knowledge. The exact and asymptotic time evolution of the contact surface ripple has been exhaustively studied with the help of the Bessel functions series and the model presented here. We have found that in order to describe the asymptotic behavior of $\psi_i(t)$, we must incorporate an asymptotic ordinate $\psi_\infty$. This behavior was already observed by Meyer and Blewett in their simulations, but they could not give any scaling law to describe it. The goodness of an irrotational approximation to characterize the behavior of the normal contact velocity has been studied in different ranges of the preshock parameter space. The influence of the incident shock strength as well as the values of $R_0$, $\gamma_a$, and $\gamma_b$ have been carefully analyzed. In general, an irrotational approximation is justified for $M_i \lesssim 1.5$. As with the behavior with respect to $R_0$, there is no simple rule to be given. Even for very weak shocks, there could be ranges of $R_0$ in which an irrotational approximation would be very bad because we could be approaching a freeze-out situation. At higher strengths, the comparison would be also strongly dependent on the values of the isentropic exponents. We have found that for strong shocks, the relative error might be well above 10%, except in exceptional cases in which $F_a = 0$. As for the relative error between the exact solution and the irrotational approximation as a function of $\gamma_a$ and $\gamma_b$, conclusions are more or less similar. This complicated behavior is certainly related to the complex mathematical structure of the solutions of this apparently simple linear problem, which is manifest because of the nonzero value of $F_a$ in most of the parameter space. A good indicator of irrotationality would be the equality between the normal and tangential velocities in the compressed fluid. To this scope, the ratio between both quantities has also

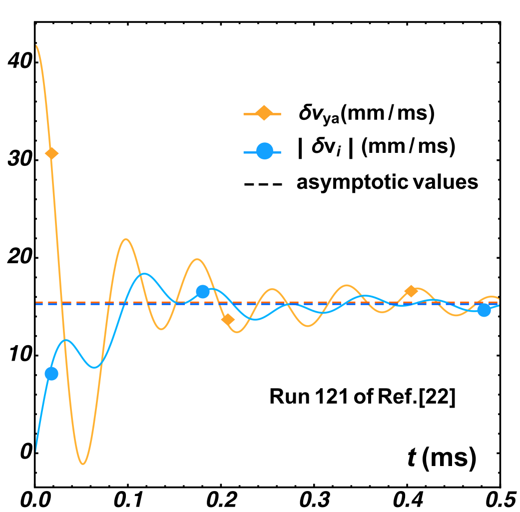


FIG. 32. Comparison of the time evolution of the normal and tangential velocity inside fluid $a$.

been studied as a function of the four preshock parameters and conclusions are consistent with the behavior observed before. As a good rule of thumb, in order to decide whether an irrotational approximation could be a good choice or not, is to roughly compare the bulk parameter $F_a \neq 0$ with any of the initial tangential velocities. If these quantities are similar, this might indicate us that significant vorticity is generated behind the transmitted shock. An approximate and quite simple formula for the normal velocity has been proposed that work very well in situations where $F_a$ is not negligible, and irrotational estimations fail. Having at hand an exact description of the velocity field, it is worth to present exact Taylor expansions of the normal velocity as a function of some small parameter in different physical limits. This has been done expanding $u_i$ in the weak shock limit, strong shock limit, near the total transmission boundary, near the critical preshock density ratio where the rarefaction is steady in the laboratory frame, near the limit of negligible ambient density for very strong rarefactions. All these expansions suffer from the same illness: they have limited convergence circles. The expansion coefficients can be easily calculated with the files attached inside the Supplemental Material [37]. The calculations shown here have been contrasted with experiments and simulations done in two different environments: a very strong incident shock and a weak incident shock situation. The contact surface ripple evolution followed with our model equations agree quite well with experiments and numerical calculations within the time interval in which a linear theory is acceptable. We have found that, in both limits, the contact surface ripple enters its asymptotic stage much earlier than does the transmitted shock to enter its asymptotic regime. This fact had been also observed by Meyer and Blewett in their 1974 work. We have also found that the rarefaction tail ripple also enters its asymptotic stage at a much later time than the interface. Besides, the contact surface enters its linear asymptotic when the transmitted has almost generated its first vorticity peak. We hope that the results shown here might be useful in the design and analysis of future more complex experiments and more elaborate models of nonlinear evolution, and to help with the development of reshock theoretical models.

## ACKNOWLEDGMENTS

The authors would like to thank A. R. Piriz and A. Bret (UCLM) for encouraging discussions, C. Huete (UC3M) for helpful comments. F.C.C. acknowledges support from UCLM for a predoctoral fellowship. This work has received support from MINECO under Grant No. ENE2013-45661-C2-1-P and PEII Grant No. 2014-008-P by JCCM (Spain).

## APPENDIX A: CALCULATION OF $\psi_\infty$

The value of the origin ordinate $\psi_\infty$ depends on the accuracy with which we evaluate the derivatives of the pressure functions $F_{a1,2}$ at $q_a = 0$. In fact, we must calculate

$$\psi_\infty = \psi_0^* - \frac{D_i}{c_{af}}[F'_{a1}(0) - F'_{a2}(0)]\psi_0. \tag{A1}$$

We rewrite here Eq. (47) for convenience:

$$F_{a2}(q_a) = \epsilon_{a1}(q_a) + \epsilon_{a2}(q_a)F_{a1}(q_a - 2\chi_t), \tag{A2}$$

where

$$\epsilon_{a1}(q_a) = \frac{v_{ya}^0}{\sinh(q_a - \chi_t)\eta^+(q_a - \chi_t)}, \tag{A3a}$$

$$\epsilon_{a2}(q_a) = -\frac{\eta^-(q_a - \chi_t)}{\eta^+(q_a - \chi_t)}. \tag{A3b}$$

On the other hand, $F_{a1}(q_a)$ satisfies the functional equation (79), which we also rewrite here for convenience:

$$F_{a1}(q_a) = \phi_{a1}(q_a) + \phi_{a2}(q_a)F_{a1}(q_a - 2\chi_t). \tag{A4}$$

We make an expansion of $F_{a1}(q_a - 2\chi_t)$ near $q_a = 0$ and retain linear terms in $q_a$. After substituting in both Eqs. (A2) and (A4), we easily arrive to the desired result:

$$\begin{aligned} &F'_{a1}(0) - F'_{a2}(0) \\ &\quad = \phi'_{a1}(0) - \epsilon'_{a1}(0) + [\phi'_{a2}(0) - \epsilon'_{a2}(0)]F_{a1}(-2\chi_t) \\ &\qquad + \phi'_{a2}(0)F'_{a1}(-2\chi_t). \end{aligned} \tag{A5}$$

We see, as happened in the shock reflected case [15], that the accuracy with which we can calculate $\psi_\infty$ is governed by the accuracy with which we obtain $F_{a1}(-2\chi_t)$ and $F'_{a1}(-2\chi_t)$. These last two quantities can be calculated with the desired accuracy, by increasing the number of iteration steps inside Eq. (83).

## APPENDIX B: DETAILED CALCULATIONS FOR PARTICULAR CASE HF100/10 OF [12,13]

In this Appendix, we show, step by step, the algebraic calculations to obtain the results presented in the main text for the case HF100/10 of [12,13] where a shock comes from beryllium and transmits inside a foam. The preshock parameters for this particular case are [13]: incident shock strength $M_i = 15.3$, initial density ratio across the contact surface $R_0 = 0.0706$ which gives a preshock Atwood number $A_T \cong -0.8681$. The shocked (foam) and rarefacted (beryllium) fluids are correspondingly characterized by $\gamma_a = 1.45$ and $\gamma_b = 1.8$. The preshock ripple amplitude is $\psi_0 = 10\ \mu$m and the corrugation wavelength is $\lambda = 100\ \mu$m. As $R_0^{tt} \cong 1.1432 > 0.0706$, it is clear from Eq. (2) that we are in a rarefaction reflected case.

### 1. Zero order quantities

From Eq. (1), the incident shock strength is $z_i = (p_1 - p_0)/p_0 \cong 300$ and the downstream incident Mach number, is, according to Eq. (7), $\beta_i \cong 0.474\,14$. The incident shock speed is $D_i = -49.79\ \mu$m/ns [13]. The initial sound speeds are $c_{a0} \cong 10.992\ \mu$m/ns for foam, and $c_{b0} \cong 3.254\ \mu$m/ns for beryllium. Therefore, the ratio of preshock sound speeds is $N_0 = c_{a0}/c_{b0} \cong 3.377\,89$. To calculate the transmitted shock strength ($z_t$) and the expansion strength $M_1 = c_{bf}/c_{b1}$, as proposed in [19], we need to solve the nonlinear equations system (18). We obtain $z_t = (p_2 - p_0)/p_0 \cong 53.094\,09$ and $M_1 \cong 0.683\,05$. The upstream and downstream transmitted Mach numbers are, respectively, according to Eqs. (11) and (12): $M_t \cong 6.771\,66$, and $\beta_t \cong 0.413\,27$. We display below the different ratios of post-shock quantities. We show at first the ratios behind the incident front, according to Eqs. (5)

and (6):

$$\frac{\rho_{b1}}{\rho_{b0}} \cong 3.463\,02, \quad \frac{c_{b1}}{c_{b0}} \cong 9.318\,16, \quad \frac{U_1}{c_{b0}} \cong 10.881\,89. \tag{B1}$$

For this experiment, we thus have $c_{b1} \cong 30.324$ $\mu$m/ns and $U_1 \cong 35.412$ $\mu$m/ns. The fluid particles with speed $U_1$ move from right to left (see Fig. 1). The self-similar coordinates of the rarefaction head and tail in the system fixed to the contact surface are, respectively, according to Eq. (9): $\zeta_{rh} \cong 1.792\,38$ and $\zeta_{rt} = M_1 \cong 0.683\,05$. The density and pressure jumps across the rarefaction fan are given by Eq. (10). We remind that $A = M_1$ at the rarefaction tail. Then,

$$\frac{\rho_{bf}}{\rho_{b1}} \cong 0.385\,59, \quad \frac{p_{b1}}{p_{b0}} \cong 0.179\,90. \tag{B2}$$

The transmitted shock dimensionless coordinate is $\chi_t = -\arctan\beta_t \cong -0.413\,27$. We also calculate the ratios across the transmitted shock, using the expressions inside Eqs. (13) and (14):

$$\frac{\rho_{af}}{\rho_{a0}} \cong 4.963\,38, \quad \frac{c_{af}}{c_{a0}} \cong 3.301\,31, \quad \frac{U}{c_{a0}} \cong 5.407\,33. \tag{B3}$$

The ratio of final densities and final sound velocities, at the contact surface, are

$$R = \frac{\rho_{af}}{\rho_{bf}} \cong 0.262\,42, \quad N = \frac{c_{af}}{c_{bf}} \cong 1.752\,06. \tag{B4}$$

We have $c_{af} = 36.290$ $\mu$m/ns, $c_{bf} = 20.713$ $\mu$m/ns. In the laboratory frame, we have $U \cong 59.440$ $\mu$m/ns, $c_{bf} \cong 20.713$ $\mu$m/ns, and $D_t = 74.437$ $\mu$m/ns. Besides, $R_0^{\text{crit}} \cong 1.7552 > 0.0706$, which means that the rarefaction tail moves opposite to the contact surface in the laboratory frame.

### 2. First order quantities in the shocked fluid

The initial amplitude of the rippled transmitted front is, as it was defined after Eq. (34), $\psi_{t0} \cong -0.495\,03$ $\psi_0$. Besides, the initial tangential velocity behind the transmitted shock is [Eq. (151)] $\delta v_{ya}^0 \cong 0.590\,97\, k\psi_0 D_i = 18.488$ $\mu$m/ ns. The dimensionless slope of the Hugoniot curve at the final state behind the transmitted front is [see Eq. (46)] $1/\kappa_t \cong 7.831\,64$. In order to solve for the pressure field inside fluid $a$, we need the parameters $\alpha_{a10}$, $\alpha_{a11}$, and $\alpha_{a20}$ [Eq. (44)]:

$$\alpha_{a10} \cong 1.236\,25, \quad \alpha_{a11} \cong 1.209\,87, \quad \alpha_{a20} \cong 0.268\,20. \tag{B5}$$

### 3. Initial conditions at the corrugated rarefaction tail

The initial amplitudes of the corrugated rarefaction head and tail are, respectively, according to Eq. (51): $\psi_{rh} \cong 0.897\,80$ $\psi_0$ and $\psi_{rt} \cong 0.222\,18$ $\psi_0$. The initial tangential velocity profile inside the rarefaction fan is shown in Eq. (52), and can be rewritten in the form

$$\frac{\delta v_y(\zeta, t = 0+)}{c_{b1} k\psi_0} = a + b\,\zeta + c\,\zeta^2, \tag{B6}$$

where [see Eq. (153)]

$$a \cong -0.450\,64, \quad b \cong -0.138\,44, \quad c \cong 0.217\,51. \tag{B7}$$

It is clear that the initial tangential velocity at the rarefaction head is zero. However, the initial tangential velocity at the tail is given by Eq. (152), where we have substituted the self-similar variable of the rarefaction trailing edge $\zeta = \zeta_{rt}$. We get $\delta v_{yb}^0 \cong -0.270\,24\, k\psi_0 D_i = -8.454$ $\mu$m/ns. The negative sign indicates that $\delta v_{yb}^0$ points along the negative direction of the $\hat{y}$ axis.

### 4. Calculation of $F_{b1}(-N \sinh 2\chi_t)$

In this section we calculate the pressure amplitude $F_{b1}$, evaluated at the rarefaction tail, which is needed to later on calculate the asymptotic velocities at the contact surface. At first, we calculate the integral numerically using Eqs. (53)–(60). At $t = 0+$, the characteristic coordinates of the rarefaction tail are $\xi_{rt} = 1.771\,421$ and $\eta = 0$. On the other hand, Eq. (72) gives us an exact finite analytical expression of Eq. (71). Below, we show the values obtained, with the numerical integration or the analytical expression. We use *Mathematica* software. The quantity $t_c$ is used to indicate the calculation time used in each evaluation:

$$\begin{aligned} \text{Eq. (53)}: F_{b1}[q_b &= \arcsin(N \sin -2\chi_t)] \\ &\cong 0.048\,110\,033; \quad t_c = 0.30 \text{ s}, \\ \text{Eq. (72)}: F_{b1}[q_b &= \arcsin(N \sin -2\chi_t)] \\ &\cong 0.048\,110\,033; \quad t_c = 0.03 \text{ s}. \end{aligned} \tag{B8}$$

We see that the calculation time for $F_{b1}$ is one order of magnitude lower with the analytical formula.

### 5. Calculation of the asymptotic velocities at the contact surface

We remind here the sonic parameter $F_a$ [Eq. (116)]:

$$F_a = \left[1 + \frac{M_t^2}{M_t^2 - 1}\frac{4(D_t - U)}{U}\right]^{-1}\left[\tilde{v}_{ya}^0 - 2F_{a1}(-2\chi_t)\right]. \tag{B9}$$

From which we see that the pressure amplitude $F_{a1}$ must be evaluated at $q_a = -2\chi_t$. To get $F_{a1}$, we need to solve the functional equation (79) [11]. The starting function is Eq. (82). The auxiliary quantities necessary to build the recurrence are $\phi_{a1}(q_a)$, $\phi_{a2}(q_a)$, $\Delta(q_a)$, and $\eta_t^{\pm}(q_a)$ [Eqs. (80) and (81)]. The function $F_{b1}(q_b)$ is inside the expression of $\phi_{a1}(q_a)$. The variable $q_b$ has to be put as a function of the variable $q_a$ through the conversion relation at the interface $c_{af}\sin q_a = c_{bf}\sin q_b$. We have

$$\phi_{a1}(q_a = -2\chi_t) \cong 0.0409, \quad \phi_{a2}(q_a = -2\chi_t) \cong -0.0789, \tag{B10}$$

and the functional equation becomes

$$\begin{aligned} F_{a1}^{[n+1]}(q_a = -2\chi_t) &= 0.0409 - 0.0789 \\ &\quad \times F_{a1}^{[n]}(q_a = -2\chi_t), \quad n \geqslant 0. \end{aligned} \tag{B11}$$

Therefore, the starting and the first five iterated values of $F_{a1}(-2\chi_t)$ are

$$\begin{aligned} &F_{a1}^{[0]}(-2\chi_t) \cong 0.037\,929\,826\, k\psi_0 D_i \quad \text{[Eq. (82)]}, \\ &F_{a1}^{[1]}(-2\chi_t) \cong 0.039\,750\,764\, k\psi_0 D_i, \\ &F_{a1}^{[2]}(-2\chi_t) \cong 0.039\,719\,406\, k\psi_0 D_i, \end{aligned}$$

$$F_{a1}^{[3]}(-2\chi_t) \cong 0.039\,719\,922\, k\psi_0 D_i,$$
$$F_{a1}^{[4]}(-2\chi_t) \cong 0.039\,719\,913\, k\psi_0 D_i,$$
$$F_{a1}^{[5]}(-2\chi_t) \cong 0.039\,719\,913\, k\psi_0 D_i. \tag{B12}$$

The sonic parameter $F_a$ is obtained from Eq. (B9), and we substitute the different iterations of $F_{a1}$, we have

$$F_a^{[0]} \cong 0.253\,531\,913\, k\psi_0 D_i \;\; \text{[Eq. (117)]},$$
$$F_a^{[1]} \cong 0.251\,739\,422\, k\psi_0 D_i,$$
$$F_a^{[2]} \cong 0.251\,770\,290\, k\psi_0 D_i,$$
$$F_a^{[3]} \cong 0.251\,769\,783\, k\psi_0 D_i,$$
$$F_a^{[4]} \cong 0.251\,769\,790\, k\psi_0 D_i,$$
$$F_a^{[5]} \cong 0.251\,769\,790\, k\psi_0 D_i. \tag{B13}$$

Finally, we go to Eq. (115) to calculate the asymptotic velocities. If we substitute $F_a^{[0]}$ in the asymptotic normal velocity formula, we will get the approximate formula without iteration $u_i^{[0]}$ [Eq. (160)]. If we put successive iterations we obtain different accuracies, this process can be continued until we get the desired number of exact decimal digits. Usually, five iterations are enough to get six exact significant digits, even in very compressible cases. So, the asymptotic velocities are (remember that $\delta v_{yb}^{\infty} = \delta v_i^{\infty}$)

$$\left(\delta v_i^{\infty}\right)^{[0]} \cong -0.284\,208\,640\, k\psi_0 D_i$$
$$\cong -8.891\ \mu\text{m/ns} \;\; \text{[Eq. (160)]},$$
$$\left(\delta v_i^{\infty}\right)^{[1]} \cong -0.284\,581\,247\, k\psi_0 D_i,$$
$$\left(\delta v_i^{\infty}\right)^{[2]} \cong -0.284\,574\,830\, k\psi_0 D_i,$$
$$\left(\delta v_i^{\infty}\right)^{[3]} \cong -0.284\,574\,936\, k\psi_0 D_i,$$
$$\left(\delta v_i^{\infty}\right)^{[4]} \cong -0.284\,574\,934\, k\psi_0 D_i,$$
$$\left(\delta v_i^{\infty}\right)^{[5]} \cong -0.284\,574\,934\, k\psi_0 D_i \;\cong -8.903\ \mu\text{m/ns}, \tag{B14}$$

$$\left(\delta v_{ya}^{\infty}\right)^{[0]} \cong 0.537\,740\,554\, k\psi_0 D_i \cong 16.823\ \mu\text{m/ns},$$
$$\left(\delta v_{ya}^{\infty}\right)^{[1]} \cong 0.536\,320\,669\, k\psi_0 D_i,$$
$$\left(\delta v_{ya}^{\infty}\right)^{[2]} \cong 0.536\,345\,120\, k\psi_0 D_i,$$
$$\left(\delta v_{ya}^{\infty}\right)^{[3]} \cong 0.536\,344\,718\, k\psi_0 D_i,$$
$$\left(\delta v_{ya}^{\infty}\right)^{[4]} \cong 0.536\,344\,725\, k\psi_0 D_i,$$
$$\left(\delta v_{ya}^{\infty}\right)^{[5]} \cong 0.536\,344\,725\, k\psi_0 D_i \cong 16.779\ \mu\text{m/ns}. \tag{B15}$$

Notice the great difference between the normal and tangential velocities at the material surface. This difference is due to the non-negligible vorticity field inside fluid $a$. The weak shock approximation presented in Eq. (159) for the normal velocity, where we neglected the bulk vorticity parameter $F_a$, gives

$$\left(\delta v_i^{\infty}\right)^{ws} \cong -0.3369\, k\psi_0 D_i$$
$$= -10.542\ \mu\text{m/ns}. \tag{B16}$$

It is easy to realize from Eq. (115) that $(\delta v_i^{\infty})^{ws} = (\delta v_{yb}^{\infty})^{ws} = -(\delta v_{ya}^{\infty})^{ws}$. This weak shock approximation overestimates the asymptotic normal velocity by 18% and underestimates the asymptotic tangential velocity in fluid $a$ by 37%. But, the more important effect due to the difference between the tangential and normal velocities is in the kinetic energy stored inside fluid $a$, as will be calculated below.

#### 6. Calculation of the coefficients of the perturbed pressure solution $\pi_{2n+1}^a$ and $\omega_{2n+1}^a$, and the initial derivatives $p_{t0}^{(2n+1)}$

In order to obtain the pressure field and the rest of the perturbed quantities, it is necessary to calculate the coefficients $\pi_{2n+1}^a$ and $\omega_{2n+1}^a$ inside the perturbed pressure solution [Eq. (36)] in the form of a Bessel function series. The procedure to obtain them is explained in Sec. II. The first step is to expand each side of the functional equation for $F_{a1}$ [Eq. (79)] in powers of $1/s_a$ (where $s_a = \sinh q_a$). We have

$$F_{a1}(q_a) = \sum_{n=0}^{\infty} \frac{f_{2n+1}^{a1}}{s_a^{2n+1}} = \frac{0.043\,59}{s_a} - \frac{0.005\,53}{s_a^3} + \frac{0.002\,98}{s_a^5} - \frac{0.002\,90}{s_a^7} + \frac{0.002\,93}{s_a^9} + O\left(\frac{1}{s_a^{11}}\right). \tag{B17}$$

The coefficients $f_{a1}^1$ and $f_{a1}^3$ are explicitly written in Eqs. (86) and (87). We use the linearized boundary conditions at the shock front to relate $F_{a2}$ and $F_{a1}$, and we reach to Eq. (47). We are able to write $F_{a2}$ as a function of the previous coefficients $f_{a1}^{2n+1}$. The relation between $F_{a1,2}$ with the Laplace transform of the pressure perturbation $\tilde{P}_a$ and its auxiliary function $\tilde{H}_a$ is detailed in the main text, reaching to Eq. (38). If we particularize the relationships inside Eq. (38) at the contact surface ($\chi_a = 0$), we will arrive at Eq. (84). We have chosen this particular coordinate at the interface in order to get a single linear system for each coefficient, instead a coupled system to calculate $\pi_{2n+1}^a$ and $\omega_{2n+1}^a$. In Eq. (84), we see that there is a side which depends on $F_{a1}$ and another on a single pressure coefficient. Thus, we expand each side in powers of $1/s_a$ and equalize terms with the same power, we have a linear relation between $f_{a1}^{2n+1}$ and $\pi_{2n+1}^a$:

$$P_{ai}(s_a) = \frac{-0.0773 + 0.9561 f_{a1}^1}{s_a^2} + \frac{0.0584 - 0.5098 f_{a1}^1 + 0.9924 f_{a1}^3}{s_a^4} + \frac{-0.0488 + 0.3992 f_{a1}^1 - 0.4986 f_{a1}^3 + 0.9987 f_{a1}^5}{s_a^6}$$
$$+ \frac{0.0428 - 0.3415 f_{a1}^1 + 0.3781 f_{a1}^3 - 0.4992 f_{a1}^5 + 0.9998 f_{a1}^7}{s_a^8} + O\left(\frac{1}{s_a^{10}}\right), \tag{B18a}$$

$$P_{ai}(s_a) = \frac{\pi_1^a}{2s_a^2} + \frac{\pi_3^a - 3\pi_1^a}{8s_a^4} + \frac{\pi_5^a - 5\pi_3^a + 10\pi_3^a}{32s_a^6} + \frac{\pi_5^a - 7\pi_5^a + 21\pi_3^a - 35\pi_3^a}{128s_a^8} + O\left(\frac{1}{s_a^{10}}\right). \tag{B18b}$$

Equating equal powers of $1/s_a$ between the last two equations, we have the first $\pi_{2n+1}$ coefficients. We repeat the procedure with $H_{ai}(s_a)$:

$$\begin{aligned} H_{ai}(s_a) = {} & \frac{0.0773 + 1.0437 f_{a1}^1}{s_a} + \frac{-0.0198 + 0.0317 f_{a1}^1 + 1.0076 f_{a1}^3}{s_a^3} + \frac{0.0010 - 0.0247 f_{a1}^1 + 0.0023 f_{a1}^3 + 1.0013 f_{a1}^5}{s_a^5} \\ & + \frac{-0.0063 + 0.0184 f_{a1}^1 - 0.0048 f_{a1}^3 - 0.0001 f_{a1}^5 + 1.0002 f_{a1}^7}{s_a^7} + O\left(\frac{1}{s_a^9}\right), \end{aligned} \tag{B19a}$$

$$H_{ai}(s_a) = \frac{\omega_1^a}{2s_a} + \frac{\omega_3^a - \omega_1^a}{8s_a^3} + \frac{\omega_5^a - 3\omega_3^a + 4\omega_3^a}{32s_a^5} + \frac{\omega_5^a - 5\omega_5^a + 9\omega_3^a - 5\omega_3^a}{128s_a^7} + O\left(\frac{1}{s_a^9}\right). \tag{B19b}$$

We have finally

$$\begin{aligned} &\pi_1^a \cong -0.0712, \quad \omega_1^a \cong 0.2456, \\ &\pi_3^a \cong 0.0321, \quad \omega_3^a \cong 0.0537, \\ &\pi_5^a \cong 0.0497, \quad \omega_5^a \cong 0.0498, \\ &\pi_7^a \cong -0.0737, \quad \omega_7^a \cong -0.0726. \end{aligned} \tag{B20}$$

At this point, we are able to calculate the initial derivatives of the pressure at the transmitted shock. We use the equation system that result to equalize Eqs. (96) and (98), and we obtain

$$\begin{aligned} &p_{t0}^{(1)} \cong -0.094\,812\,947, \quad p_{t0}^{(3)} \cong 0.067\,499\,167, \\ &p_{t0}^{(5)} \cong -0.054\,579\,150, \quad p_{t0}^{(7)} \cong 0.046\,698\,056. \end{aligned} \tag{B21}$$

### 7. Contact surface ripple growth as a function of time (Fig. 18)

In this section we show the time evolution of the ripple interface. Our linear theory provides us with Eq. (129) and asymptotic formula (133). The post-shock ripple amplitude at $t = 0+$, according to Eq. (128), is $\psi_0^* \cong -0.193\,815\,267\psi_0$, which indicates that it is a direct phase inversion case. Using $u_i^{[0]}$ as the value for the dimensionless asymptotic normal velocity, we get

$$\begin{aligned} \psi_i(t)[\mu\text{m}] = {} & -1.938 + 13.720\,180\,1\Bigg\{-0.284\,208\,640\Bigg(\tau_a\left\{\tau_a J_0(\tau_a) + \frac{\pi\tau_a}{2}[J_1(\tau_a)\boldsymbol{H}_0(\tau_a) - J_0(\tau_a)\boldsymbol{H}_1(\tau_a)] - J_1(\tau_a)\right\} \\ & - 1 + J_0(\tau_a)\Bigg) + \sum_{n=0}^{\infty} 2\omega_{2n+1}^a \sum_{l=1}^{n}\left[1 - \frac{2}{\tau_a}\sum_{k=1}^{l}(2k-1)J_{2k-1}(\tau_a)\right]\Bigg\}, \end{aligned} \tag{B22}$$

where for this particular case $\tau_a = 2.280\,143\,51\ \text{ns}^{-1}\,t$. Equation (B22) is used to plot the exact linear time evolution curve (a) in Fig. 18. In order to calculate the asymptotic linear regime, it is needed to obtain the asymptotic ordinate $\psi_\infty$ given by Eq. (134), where we need to calculate the derivatives of $F'_{a1}$ and $F'_{a2}$ at the origin $q_a = 0$. Then, the asymptotic ordinate [Eq. (134)] is

$$(\psi_\infty)^{[n]} = -1.938 - 13.720\,180\,1\left[\left(F_{a1}^{[n]}\right)'(0) - \left(F_{a2}^{[n]}\right)'(0)\right]. \tag{B23}$$

To calculate $(F_{a1}^{[n]})'(0) - (F_{a2}^{[n]})'(0)$ we follow the strategy developed in Eq. (A5). We show the first five iterations:

$$\begin{aligned} &(\psi_\infty)^{[0]} \cong 0.370\,315\,726\ \psi_0, \\ &(\psi_\infty)^{[1]} \cong 0.138\,085\,814\ \psi_0, \\ &(\psi_\infty)^{[2]} \cong 0.184\,543\,403\ \psi_0, \\ &(\psi_\infty)^{[3]} \cong 0.182\,725\,015\ \psi_0, \\ &(\psi_\infty)^{[4]} \cong 0.182\,761\,012\ \psi_0, \\ &(\psi_\infty)^{[5]} \cong 0.182\,760\,406\ \psi_0 = 1.828\ \mu\text{m}. \end{aligned} \tag{B24}$$

Finally, the ripple asymptotic time evolution for this particular case is written as

$$\psi_i(t \gg t_1) \cong 1.828\ \mu\text{m} - 8.893\ \frac{\mu\text{m}}{\text{ns}}\ t, \tag{B25}$$

which is the formula used to plot curve (b) in Fig. 18.

#### 8. Velocity perturbations at the contact surface as a function of time (Fig. 21)

In this section we calculate the time evolution of the normal and tangential velocities at the interface. In this case, we use Taylor series instead of Bessel functions series. Since both methods give similar results, Taylor series provide a little more accurate description. If it is desired to calculate the time evolution through Bessel function series, we use Eq. (119) for normal velocity and its equivalent to the tangential velocity at the $a$ side:

$$\delta v_{ai}(\tau_a) = \tilde{v}^0_{ya} + \left(v_{ia} - \tilde{v}^0_{ya}\right)[1 - J_0(\tau_a)] - 2\sum_{n=0}^{\infty}\omega^a_{2n+1}\sum_{k=1}^{n} J_{2k}(\tau_a). \tag{B26}$$

For the Taylor series coefficients, we need the auxiliary coefficients $f^{2n+1}_{a1}$ that for this particular case were calculated in Eq. (B17). For $f^{2n+1}_{a2}$, we get

$$F_{a2}(q_a) = \sum_{n=0}^{\infty}\frac{f^{2n+1}_{a2}}{s_a^{2n+1}} = -\frac{0.079\,19}{s_a} + \frac{0.018\,45}{s_a^3} - \frac{0.008\,89}{s_a^5} + \frac{0.005\,42}{s_a^7} - \frac{0.003\,73}{s_a^9} + O\left(\frac{1}{s_a^{11}}\right). \tag{B27}$$

We get the series for $\tilde{H}_{ai}(s_a)$, with the initial derivatives $h^{(2n+1)}_{i0}$:

$$\tilde{H}_{ai}(s_a) = \sum_{n=0}^{\infty}\frac{h^{(2n+1)}_{i0}}{s_a^{2n+2}} = \frac{0.122\,78}{s_a^2} - \frac{0.071\,93}{s_a^4} + \frac{0.059\,32}{s_a^6} - \frac{0.058\,27}{s_a^8} + \frac{0.059\,93}{s_a^{10}} + O\left(\frac{1}{s_a^{12}}\right). \tag{B28}$$

We write next the series for $\tilde{P}_{ai}(s_a)$ withe the initial derivatives $p^{(2n+1)}_{i0}$:

$$\tilde{P}_{ai}(s_a) = \sum_{n=0}^{\infty}\frac{p^{(2n+1)}_{i0}}{s_a^{2n+2}} = -\frac{0.035\,60}{s_a^2} + \frac{0.030\,71}{s_a^4} - \frac{0.025\,72}{s_a^6} + \frac{0.021\,44}{s_a^8} - \frac{0.018\,05}{s_a^{10}} + O\left(\frac{1}{s_a^{12}}\right). \tag{B29}$$

Combining the above results, we get the following Taylor series in time for the normal and tangential velocities:

$$u_{ai}(\tau_a) = -0.122\,783\,515\,\tau_a + 0.003\,996\,278\,\tau_a^3 - 0.000\,098\,873\,\tau_a^5 + 0.000\,000\,165\,\tau_a^7 - 0.000\,000\,018\,\tau_a^9 + O\left(\tau_a^{11}\right), \tag{B30a}$$

$$v_{ai}(\tau_a) = 0.590\,970\,559 - 0.017\,797\,562\,\tau_a^2 + 0.001\,279\,777\,\tau_a^4 - 0.000\,035\,717\,\tau_a^6 + 0.000\,000\,532\,\tau_a^8 - 0.000\,000\,005\,\tau_a^{10} + O\left(\tau_a^{12}\right). \tag{B30b}$$

We note that all the series used to calculate the different quantities and to plot the figures shown in this work have been done with at least 50 coefficients in the Bessel and Taylor series. Besides, to avoid the accumulation of round-off errors, the calculations have been done with at least 200 digits behind the decimal comma. For obvious reason of space, we only show here a more limited number of coefficients and the numerical results are displayed with less than 10 digits.

#### 9. Pressure perturbation and ripple evolution at the transmitted shock; rarefaction tail corrugation as a function of time (Figs. 19 and 20)

To obtain the pressure perturbation time evolution at the transmitted shock, we can use Eq. (97) in which we use the Bessel function series solution or Eq. (95) if we want to represent it with the Taylor series. The auxiliary parameters we need for both methods have been already calculated in previous subsections. It is useful to remember that $r_t = \tau_a/\cosh\chi_t \cong 2.076\,321\ \mathrm{ns}^{-1}\ t$. To plot Figs. 19 and 20(a), we have used the Taylor series solution. The ripple time evolution of the rarefaction tail [Fig. 20(b)] is calculated by Eq. (102), and its asymptotic regime by Eq. (105). For this particular case, $u^{\infty}_{rt} \cong 0.231\,363$ and $\tau_{\mathrm{raref}} \cong 1.301\,406\ \mathrm{ns}^{-1}\ t$.

#### 10. Asymptotic velocity profiles and vorticity field (Fig. 3)

The general solution for the asymptotic velocity profiles inside both fluids is written in Eq. (137):

$$u_a(\tilde{x}) = u_i\, e^{\tilde{x}} + u_{ap}(\tilde{x}), \quad x \leqslant 0$$
$$u_b(\tilde{x}) = u_i\, e^{-\tilde{x}}, \quad x \geqslant 0. \tag{B31}$$

We must obtain the particular solution of fluid $a$. It can be written in the form of a Taylor series, and its coefficients are calculated using Eqs. (141) and (139). We get

$$u_{ap}(\tilde{x}) = \sum_{n=0}^{\infty}\frac{\theta_n^{2n+1}}{(2n+1)!}\tilde{x}^{2n+1} = -0.251\,77\,\tilde{x} + 0.121\,36\,\tilde{x}^3 - 0.022\,16\,\tilde{x}^5 + 0.002\,11\,\tilde{x}^7 - 0.000\,12\,\tilde{x}^9 + O(\tilde{x}^{11}). \tag{B32}$$

In the previous formula, we have only shown the first five coefficients, for lack of space. In Fig. 4, we have truncated the series at a much higher power (up to $x^{99}$). Because of the asymptotic incompressibility of the perturbation field, we can easily calculate the tangential velocities as $v = -du/d\tilde{x}$. The bulk vorticity field in fluid $a$ is given by Eq. (109), which in the form of a Taylor series is

$$g_a(\tilde{x}) = \Omega_a \sum_{n=0}^{\infty}\frac{p^{(2n+1)}_{t0}\sinh^{2n+1}\chi_t}{(2n+1)!}\tilde{x}^{2n+1}, \tag{B33}$$

where $\sinh\chi_t \cong -0.453\,836$ and $\Omega_a \cong 4.690\,599$ according Eq. (110). The initial derivatives $p_{t0}^{(2n+1)}$ have been obtained before.

#### 11. Kinetic energy

We calculate now the kinetic energy perturbation stored in a vorticity strip inside the fluid $a$. The formula is given by Eq. (144), where we need to evaluate an integral which is a function of the normal coordinate $x$. The exact value [Eq. (145)] involves the normal and tangential velocity profiles obtained in the previous subsection, which strongly depend on the amount of vorticity stored inside the fluid. For the sake of comparison, an irrotational estimate [Eq. (146)] could also be done (valid, however, only for very weak shocks). Both estimates (rotational and irrotational) are shown in Fig. 4. We give below the values obtained with both estimates, inside different strips of fluid:

$$\delta e_{\text{kin}}^{a}\left(-0.2\lambda,\frac{\lambda}{2}\right) \cong 16.747 \text{ J/m},$$
$$\delta e_{\text{kin}}^{a}\left(-1.4\lambda,\frac{\lambda}{2}\right) \cong 20.301 \text{ J/m},$$
$$\left(\delta e_{\text{kin}}^{a}\right)^{irr}\left(-0.2\lambda,\frac{\lambda}{2}\right) \cong 8.631 \text{ J/m},$$
$$\left(\delta e_{\text{kin}}^{a}\right)^{irr}\left(-1.4\lambda,\frac{\lambda}{2}\right) \cong 9.391 \text{ J/m}. \tag{B34}$$

The irrotational calculation underestimates the real kinetic energy by slightly more than 50%.

The ratio between the perturbed kinetic energy and the zero order kinetic energy is given in Eq. (148). We get

$$\frac{\delta e_{\text{kin}}^{a}}{e_{\text{kin}}^{2}}(-0.2\lambda) \cong 1.59\%,$$
$$\frac{\delta e_{\text{kin}}^{a}}{e_{\text{kin}}^{2}}(-1.4\lambda) \cong 0.28\%,$$
$$\left(\frac{\delta e_{\text{kin}}^{a}}{e_{\text{kin}}^{2}}\right)^{irr}(-0.2\lambda) \cong 0.82\%,$$
$$\left(\frac{\delta e_{\text{kin}}^{a}}{e_{\text{kin}}^{2}}\right)^{irr}(-1.4\lambda) \cong 0.12\%. \tag{B35}$$

#### 12. Physical limits approximate analytical formulas

To conclude this particular case, we calculate the asymptotic normal and tangential velocities at the interface using the *Mathematica* files attached in the Supplemental Material [37]. In this particular case, the only reasonable physical limit we may take is the strong shock limit. We use the corresponding file and obtain the expansions

$$u_i)_{M_i\gg 1} \cong -0.278\,923 - \frac{1.264\,283}{M_1^2} + \frac{7.140\,142}{M_i^4} + O\left(\frac{1}{M_i^6}\right),$$
$$F_a)_{M_i\gg 1} \cong 0.250\,735 + \frac{0.950\,479}{M_1^2} - \frac{70.081\,469}{M_i^4} + O\left(\frac{1}{M_i^6}\right). \tag{B36}$$

If we evaluate the above expressions at $M_i = 15.3$, we get

$$\delta v_i^{\infty}\big)_{M_i\gg 1} \cong -0.284\,193\, k\psi_0 D_i \cong -8.891\ \mu\text{m/ns},$$
$$\delta v_{ya}^{\infty}\big)_{M_i\gg 1} = \mathcal{F}_a)_{M_i\gg 1} - \delta u_i^{\infty}\big)_{M_i\gg 1} \cong 0.537\,710\, k\psi_0 D_i \cong 16.8217\ \mu\text{m/ns}. \tag{B37}$$

The strong shock approximation underestimates the normal velocity in 0.13% and overestimates the tangential velocity in 0.25%.


[1] R. D. Richtmyer, Commun. Pure Appl. Math. **13**, 297 (1960).
[2] E. E. Meshkov, Fluid Dyn. **4**, 101 (1969).
[3] G. Fraley, Phys. Fluids **29**, 376 (1986).
[4] K. A. Meyer and P. J. Blewett, Phys. Fluids **15**, 753 (1972).
[5] Y. Yang, Q. Zhang, and D. H. Sharp, Phys. Fluids **6**, 1856 (1994).
[6] A. L. Velikovich, Phys. Fluids **8**, 1666 (1996).
[7] J. G. Wouchuk and K. Nishihara, Phys. Plasmas **3**, 3761 (1996).
[8] J. G. Wouchuk and K. Nishihara, Phys. Plasmas **4**, 1028 (1997).
[9] A. L. Velikovich, J. P. Dahlburg, A. J. Schmitt, J. H. Gardner, L. P. Phillips, F. L. Cochran, Y. K. Chong, G. Dimonte, and N. Metzler, Phys. Plasmas **7**, 1662 (2000).
[10] J. G. Wouchuk, Phys. Rev. E **63**, 056303 (2001).
[11] J. G. Wouchuk, Phys. Plasmas **8**, 2890 (2001).
[12] G. Dimonte, C. E. Frerking, M. Schneider, and B. Remington, Phys. Plasmas **3**, 614 (1996).
[13] R. L. Holmes, G. Dimonte, Bruce Fryxell, M. L. Gittings, J. W. Grove, M. Schneider, D. H. Sharp, A. L. Velikovich, R. P. Weaver, and Q. Zhang, J. Fluid Mech. **389**, 55 (1999).
[14] J. G. Wouchuk and T. Sano, Phys. Rev. E **91**, 023005 (2015).
[15] F. Cobos Campos and J. G. Wouchuk, Phys. Rev. E **93**, 053111 (2016).
[16] K. O. Mikaelian, Phys. Rev. Fluids **1**, 033601 (2016).
[17] Y. Kivity and M. Hanin, Isr. J. Technol. **8**, 139 (1970).
[18] Y. Kivity and M. Hanin, Phys. Fluids **24**, 1010 (1981).
[19] A. L. Velikovich and L. Phillips, Phys. Fluids **8**, 1107 (1996).

[20] J. G. Wouchuk and R. Carretero, Phys. Plasmas **10**, 4237 (2003).
[21] F. Cobos Campos and J. G. Wouchuk, Phys. Rev. E **90**, 053007 (2014).
[22] C. Mariani, M. Vandemboomgaerde, G. Jourdan, D. Souffland, and L. Houas, Phys. Rev. Lett. **100**, 254503 (2008).
[23] J. G. Wouchuk and J. Lopez Cavada, Phys. Rev. E **70**, 046303 (2004).
[24] J. G. Wouchuk and F. Cobos-Campos, Plasma Phys. Control. Fusion **59**, 014033 (2017).
[25] J. G. Wouchuk, C. Huete Ruiz de Lira, and A. L. Velikovich, Phys. Rev. E **79**, 066315 (2009).
[26] C. Huete Ruiz de Lira, A. L. Velikovich, and J. G. Wouchuk, Phys. Rev. E **83**, 056320 (2011).
[27] A. L. Velikovich, A. Schmitt, J. H. Gardner, and N. Metzler, Phys. Plasmas **8**, 592 (2001).
[28] A. L. Velikovich, S. T. Zalesak, N. Metzler, and J. G. Wouchuk, Phys. Rev. E **72**, 046306 (2005).
[29] K. O. Mikaelian, Phys. Fluids A **3**, 2625 (1991).
[30] Z. Dell, R. F. Stellingwerf, and S. I. Abarzhi, Phys. Plasmas **22**, 092711 (2015).
[31] C. Huete, J. G. Wouchuk, and A. L. Velikovich, Phys. Rev. E **85**, 026312 (2012).
[32] A. L. Velikovich and G. Dimonte, Phys. Rev. Lett. **76**, 3112 (1996).
[33] G. B Whitham, *Linear and Nonlinear Waves* (Wiley, New York, 1974), p. 174.
[34] M. G. Briscoe and A. A. Kovitz, J. Fluid Mech. **31**, 529 (1968).
[35] *NIST Handbook of Mathematical Functions*, edited by Frank W. J. Olver, Daniel W. Lozier, Robald F. Boisvert, and Charles W. Clark (U.S. Department of Commerce and Cambridge University Press, New York, 2010).
[36] M. Abramowitz and I. A. Stegun, *Handbook of Mathematical Functions with Formulas, Graphs and Mathematical Tables* (Dover, New York, 1970).
[37] See Supplemental Material at http://link.aps.org/supplemental/10.1103/PhysRevE.96.013102 for *Mathematica* files that can be used to follow some of the calculations.